Institute of Engineering Surveying and Space Geodesy
School of Civil Engineering

Digital Surface Modelling in Developing Countries Using Spaceborne SAR Techniques

by

Earl Peter Fitz-Gerald EDWARDS
BSc (Hon) (UWI), MPhil. (Cambridge)

Thesis submitted to the University of Nottingham for
the degree of Doctor of Philosophy

September 2005

To My Mother Rita Shirley Bratwaite-Edwards

&

In Memory of My Father Lewis Sylvanus Edwards (1920 – 1992)

Abstract

Topographic databases at the national level, in the form of Digital Surface Models (DSMs), are required for a large number of applications which have been spurred on by the increased use of Geographic Information Systems (GIS). Ground-Based (surveying, GPS, etc.) and traditional airborne approaches to generating topographic information are proving to be time consuming and costly for applications in developing countries. Where these countries are located in the tropical zone, they are affected by the additional problem of cloud cover which could cause delays for almost 75% of the year in obtaining optical imagery. The Caribbean happens to be one such affected territory that is in need of national digital topographic information for its GIS database developments, 3D visualization of landscapes and for use in the digital ortho-rectification of satellite imagery.

The use of Synthetic Aperture Radar (SAR), with its cloud penetrating and day/night imaging capabilities, is emerging as a possible remote sensing tool for use in cloud affected territories. There has been success with airborne single-pass dual antennae systems (e.g. STAR 3i) and the Shuttle Radar Topographic Mapping (SRTM) mission. However, the use of these systems in the Caribbean are restrictive and datasets will not be generally available. The launching of imaging radar satellites such as ERS-1, ERS-2, Radarsat-1 and more recently Envisat have provided additional opportunities for augmenting the technologies available for generating medium accuracy, low cost, topographic information for developing countries by using the techniques of Radargrammetry (StereoSAR) and Interferometric SAR (InSAR).

The primary aim of this research was to develop, from scratch, a prototype StereoSAR system based on automatic stereo matching and space intersection algorithms to generate medium accuracy, low cost DSMs, using various influencing parameters without any recourse to ground control points. The result was to be a software package to undertake this process for implementation on a personal computer. The DSMs generated from Radarsat-1 and Envisat SAR imagery were

compared with a reference surface from airborne InSAR and conclusions with respect to the quality of the StereoSAR DSMs are presented. Work required to further improve the StereoSAR system is also suggested.

Acknowledgements

This thesis is the result of three years of directed research conducted at the Institute of Engineering Surveying and Space Geodesy (IESSG), The University of Nottingham in the United Kingdom. The research was funded through a three year studentship provided by The University of Nottingham which was arranged through the IESSG.

I am indebted to my research supervisors Dr. Andrew Sowter and Dr. Martin Smith from the IESSG for the advice, support and encouragement received throughout the research. I am also grateful to the internal assessor, Dr. Richard Bingley, for his useful suggestions and recommendations. Thanks to Dr. Chris Hill and Dr. Caroline Noakes for their assistance with the Everett interpolation. Gratitude is also expressed to Mr. Theo Veneboer, Mr. Sean Ince, Dr. Samantha Waugh, PhD colleagues and other members of staff at the IESSG for their assistance in one way or another throughout the life of this project.

I wish to thank the University of Technology, Jamaica for granting study leave to take up the PhD offer at The University of Nottingham. Thanks also to the University of Nottingham and the IESSG for funding my PhD studies. Appreciation to Radarsat International and InfoTerra for providing the radar images used in this project at a substantially reduced cost. Thanks also to European Space Agency (ESA) for providing the Envisat SAR imagery free of cost under *Envisat project AO779* where Dr. Andrew Sowter is the Principal Investigator.

I express gratitude to the Jamaica Forestry Department for providing the ancillary datasets (maps, digital contours etc) of the study area, and Spatial Innovision Limited, a GIS company located in Jamaica, for supplying the reference InSAR DSM and geo-referenced IKONOS images used in this study.

Thanks to my friends Karen, Michael, Shantel, Karlene and Sheea for making those early years in England more tolerable and enjoyable. I am eternally grateful to my mother, brothers and sisters for their encouragement and support. To my fiancée Hazelle, thanks for your love, patience, prayers and understanding and for your assistance in proof-reading this thesis. Finally, and most importantly, thanks to ***GOD*** for making all this possible, ***HE*** is truly magnificent!

Contents

List of Figures

List of Tables

Chapter 1
Introduction

1.1 Overview

National topographic databases in the form of Digital Surface Models (DSMs) from which information on elevation, slope, aspect and line-of-sight can be extracted are required by many organisations for use in applications such as: environmental monitoring; flood risk assessment; natural resource management; telecommunication planning; topographical mapping; geo-referencing & visualization of earth observation imagery; multimedia products; flight simulations; etc. The recent popularity of Geographic Information Systems (GIS) as a tool for combining and analysing various databases to manage land resources and to model future land uses, threats to the environment and the sustainability of resources, has been a catalyst for the increased demand for up-to-date geographic information in a digital format. The development of digital databases in support of GIS applications is by no means an inexpensive undertaking since approximately 80% of the cost of implementing such systems is associated with data capture and conversion (*Edwards 1998*). Traditionally, paper topographical maps generated using analogue photogrammetric techniques have been the main source for providing surface models for use in a GIS. In fact, it is currently the method used in most developing regions including the Caribbean, for generating topographic databases.

Modern photogrammetric approaches have been developed in recent years for automating the traditional techniques and it is now possible to obtain imagery from airborne sensors, without the use of costly ground control points, which can be used in digital processes for creating DSMs (see *Mikhail et al. 2001; Shukla 2001*). The recent launch of high resolution satellite sensors such as: Ikonos, SPOT5 and Quickbird provide additional opportunities for generating DSMs from space (see *Toutin 2001*). Most developing countries cannot afford to own or contract the services of modern airborne imaging systems due to limited financial capabilities resulting from heavy national debt burdens. External funding from international

lending agencies for such mapping projects can take up to five years between conceptualization and implementation (*Clarke 2004*) further frustrating the development of topographic databases.

Developing countries must therefore rely on spaceborne systems for the provision of topographic information if it is required in a timely fashion and at moderate costs. Because the spaceborne systems mentioned earlier are optical systems – operating in the visible part of the electromagnetic spectrum and requiring illumination from the sun – they are incapable of penetrating cloud cover and can only be used during daytime. This makes their use quite limited in tropical zones where there are many developing countries, such as the Caribbean, which is often affected by cloud cover. The 'imaging window' for most Caribbean islands is between December and March which means that 75% of the year is lost due to cloud cover problems (*Kost 2002*). A search of the LandSat online database for imagery of the Caribbean island of Jamaica did not turn up any cloud free images, even during this so called 'imaging window' which suggests that on cloud-free days the sensor may not be imaging that location on the earth; examples are shown in Figure 1.1 and further examples can be seen at *http://bsrsi.msu.edu/cgi-bin/access7g.pl*. It is important to note that for the extraction of topographic information, a stereoscopic pair of cloud-free images is required.

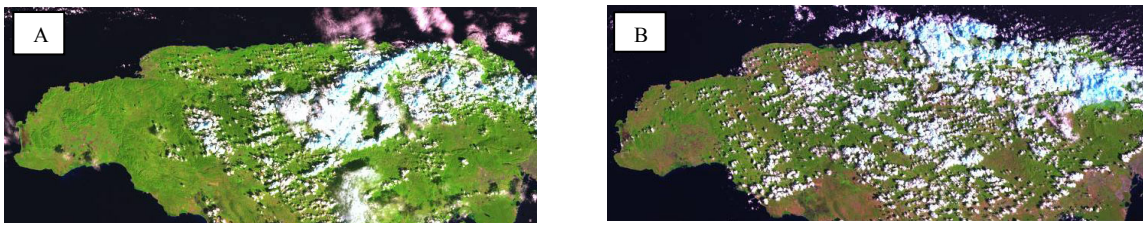

Figure 1.1: *Images of Jamaica from LandSat: (A) February 2002; (B) March 2002 (www.landsat.org)*

The launch of the Radarsat satellite, and more recently the Envisat satellite, with their microwave imaging characteristics, along with their cloud penetrating and day/night imaging capabilities make them a compelling alternative to optical spaceborne sensor for generating topographical information. These sensors are capable of generating cloud-free stereoscopic radar imagery for almost any location on the earth's surface with repeatability of just a few days depending on imaging

mode. Radargrammetry, referred to today as Stereoscopic SAR (StereoSAR) and Interferometry (InSAR) are the two main techniques for the extraction of valuable topographic information from radar data (see section 2.3). The use of spaceborne Radar technology for augmenting existing DSM methodologies in developing countries shows great promise and should therefore be investigated as a possible solution, in the Caribbean region, for products at the medium or small scale (i.e. 1:25,000 – 1:100,000). Future Radar systems (see section 2.9) to be launched as early as the summer of 2005 promises higher spatial resolution (3m) thus providing further opportunities for topographic products at 1:10,000 or larger map scales.

1.2 Motivation for the Research

Developing countries (referred to in the past as *The Third World)* are countries with a low average income compared to the world average. They are often indebted nations that are currently trying to industrialize or develop alternative methods of supporting their populations and most times have to rely on foreign capital or development aid. These countries usually have a relatively low level of technological sophistication and economic productivity. Despite economical and technological challenges, these countries still strive to protect their environment and better allocate natural resources to achieve self-sustainability. The lack of credible, current spatial information leads to 'best guess' decision making and incohesive development plans. There is a need to investigate low-cost solutions for delivering some of this spatial information, for example, the provision of topographic information, particularly in cloud affected tropical regions.

In developing countries, airborne SAR systems are not always accessible to general users. Topographic data from the recently released Shuttle Radar Topographic Mission (SRTM) is widely available for most parts of the globe, but at a spatial resolution of 90m and they are restricted to research purposes and may not be used in any commercial applications. The SRTM datasets are known to contain data voids in areas of steep terrain and gaps left arising from non-parallel orbital tracks. The reliance for the supply of SAR data for applications in developing countries will certainly have to be from satellite platforms.

Several spaceborne Radar systems have been in use for sometime now (see section 2.9) and include the European Remote Sensing Satellites (ERS-1, ERS-2), the Canadian Radar Satellite (Radarsat) and more recently the European ENVIronmental SATellite (Envisat). The orbital data quality of ERS-1 and ERS-2 at the meter level made it possible to conduct experiments using the InSAR technique for the extraction of topographic information using these satellites (see for example *Hensley et al. 1993*; *Zebker et al. 1994*; *Vachon et al. 1995*; and *Rufino et al. 1998*). However, it is difficult to achieve good results from repeat pass satellite based InSAR due to atmospheric factors and decorrelation over forest canopies and other densely vegetated areas, and the time lapse between the acquisition of each image in the pair. This therefore makes satellite InSAR unsuitable for topographic extraction over most cloud affected developing countries that contain steep terrain and dense forest, as will be discussed later in this thesis (see section 3.3.5).

Compared to the spaceborne InSAR technique, the StereoSAR procedure is not constrained by these factors, making it a better alternative for extracting elevation information over most developing countries situated in tropical regions. However, there are two aspects to this method which need to be solved in order to achieve useful topographic information. Firstly, the identification of a large quantity of densely spaced points, usually called a *point cloud*, covering the overlap portion of the stereoscopic pair of images and the subsequent determination of the differences between the position of each point and its conjugate to generate a *disparity* or *parallax* file. This is normally achieved through a process called *stereo-matching* (see chapter 4). Secondly, the conversion of the data in the disparity files to create a three dimensional (3D) point cloud using an appropriate SAR sensor model to link the image space coordinates of the conjugate points to the object space coordinates in a desired map projection system and vertical datum. The procedure for achieving this is called *space intersection* (see chapter 5). The success, however, relies on the availability of good stereoscopic pairs of SAR imagery.

Although the ERS satellites have good orbital data, the viewing direction is fixed at an incidence angle of ~ 23^{o}, except for a brief period in 1992 during a Roll-Tilt Mode (RTM) satellite manoeuvre to achieve an incidence angle of 37^{o}. Some results using data from these two incidence angles have been presented by *Twu and Dowman 1996*

and *Twu 1996*. However, this satellite cannot normally achieve multiple incidence angles and therefore would be unsuitable for routine StereoSAR applications despite its accurate orbit. Radarsat, for the first time, provided the opportunity for recording Radar images with multiple incidence angles and spatial resolutions that are suitable for StereoSAR applications. Under the Application Development and Research Opportunity (ADRO) programme, sponsored by the Canadian Space Agency (CSA), data was made available to researchers to perform evaluations on the datasets to assess its stereoscopic capabilities; the results were presented at the Radarsat ADRO Symposium held in Montreal Canada in 1998.

The main limitation of this satellite is its poor precision of orbit when compared to ERS-1 and ERS-2. Some authors have used several ground control points (GCPs) in the formulation of their StereoSAR algorithms (for example *Toutin 1995* and *Toutin 1999*) to refine the Radarsat orbit, while others have used a few GCPs to remove the systematic trends in elevations where a more rigorous StereoSAR strategy was implemented (for example *Chen 2000*, *Chen and Dowman 2001*). The identification of GCPs in Radar imagery is an extremely difficult task due to the quality of the image and may not result in large, well distributed quantities of GCPs particularly over landscapes comprising of forests and mountains in developing countries such as the Caribbean. This may be because there are simply not enough clearly identifiable features in the imagery that can be detected on the topographical map being used to generate the control points; the topographical maps maybe outdated or the features may not be large enough to be detected at the Radar resolution. Therefore, any StereoSAR algorithms will ideally have to be developed without the reliance on GCPs.

Another issue when using the StereoSAR technique for the generation of topographic information is the reduction of speckle noise (see section 2.8). Speckle noise is common in SAR imagery and can create difficulties in the interpretation and extraction of information, especially at the stereo-matching stage. The common approach is to reduce this effect with the use of *speckle filters*. However, there appears to be conflicting views being reported in the literature regarding the use of speckle filters on SAR imagery. *Dowman et al. 1997* do not believe that pre-processing the image with a speckle filter will improve the accuracy of the

topographic information if a multi-scale (coarse-to-fine) approach is used to extract the elevations. *Toutin 1999* noted that the use of a speckle filter can slightly reduce the image contrast and smoothes out the relief, especially the low tones. *Belgued et al. 1999* noted that filtering has the inconvenience of deleting some important information in the SAR image, especially structures and contours. These opinions appear to be shared by *Sowter 1998*. On the contrary, there are many researchers who argue that speckle affects the stereo matching process and must be removed using an appropriate adaptive filter before matching proceeds (see for example, *Sylvander et al. 1998*; *Raggam and Gutjahr 1998*; and *Gelautz et al. 2003*). Based on these differing views, it was felt necessary to investigate the influence that speckle filtering would have on the StereoSAR DSM being developed in this research.

Until now, there have not been any satellites capable of providing accurate orbits while at the same time recording images using multiple incidence angles. The new Envisat satellite launched recently provides the best of both worlds. It has a superior orbit with cm level accuracy and has the capability of providing images at multiple incidence angles and spatial resolutions. It is essentially a synergy between the good features of ERS and Radarsat and can thus routinely provide stereoscopic images for almost any part of the globe.

As yet, there have been no studies reported in the literature investigating the development of StereoSAR systems for the extraction of topographic information from stereoscopic pairs of Envisat Radar imagery with or without using GCPs and the evaluation of the products derived from such systems. A review of the literature did not identify any studies investigating the use of spaceborne StereoSAR techniques over cloud affected developing countries of the Caribbean, so knowledge of how StereoSAR performs over these areas is unknown at this time. In contributing to knowledge, this thesis sought to provide answers to some of the following research questions:

- How does the performance of Envisat and Radarsat compare for space intersection without using GCPs?
- Does the use of multiple rays (i.e. intersection from more than two orbital positions) from the more accurate Envisat orbit improve the elevations determined from the space intersection process?
- How does the StereoSAR DSM from Radarsat and Envisat compare over a test site in a tropical region?
- Is it possible to automatically produce a geocoded SAR image while simultaneously generating the StereoSAR DSM?
- Is there any benefit from speckle filtering images before stereo-matching?

1.3 Research Aims and Objectives

Developing countries have financial difficulties which result in limited resources available for the generation of topographic information and these countries must rely on the near global data coverage available from spaceborne platforms. Many of these developing countries are located in tropical zones where there are often cloud cover problems making SAR a compelling alternative to optical techniques for the generation of topographic information over these areas. However, not all SAR techniques can be used due to limitations caused by steep terrain, forest canopies and the influence of speckle noise on the imagery.

The main aim of this research was to investigate the use of spaceborne stereoscopic Radar from Radarsat-1 and the new Envisat Advanced SAR (ASAR) for the generation of topographic information, essentially DSMs, over a developing country in a tropical region by designing, implementing and testing a prototype StereoSAR system which does not require the need for ground control points (GCPs) in constructing the geometric model, and featuring an adaptive stereo matching algorithm. The following research objectives were proposed:

- Investigation and development of an adaptive strategy for stereo matching spaceborne SAR imagery.
- Development of a GCP-free Space Intersection strategy and a comparison of its performance on Radarsat and Envisat SAR data.
- Development of a low-cost StereoSAR software system and a critical assessment of the DSM product generated utilizing Radarsat and Envisat stereoscopic imagery.
- Evaluation of the effects of speckle filtering on the quality of the StereoSAR DSM product.

1.4 Research Methodology

In pursuit of the aims and objectives mentioned earlier, the research project followed four (4) stages:

- **Stage 1 - Background**: This involved an investigation, through literature review and an analysis of existing stereo matching and space intersection techniques for spaceborne SAR imagery. It also provided the knowledge and skills required for the different areas that the research addressed.
- **Stage 2 - Algorithm and Software Development**: All the image processing, stereo matching, space intersection and DSM generation algorithms required for the StereoSAR software system were developed at this stage.
- **Stage 3 - System Integration and Testing**: Here, all the algorithms developed were integrated into the StereoSAR application and tested for its robustness over a tropical territory with limited resources. The Caribbean island of Jamaica was identified as the test site. The possibility of simultaneously geocoding the SAR image while generating a StereoSAR DSM was investigated at this stage.
- **Stage 4 - Analysis and Conclusions**: The DSMs produced and the methodology for obtaining them were critically analysed and conclusions drawn from the test results. Discussions were conducted on the suitability of the StereoSAR system developed during this research for generating DSMs in developing countries such as the Caribbean.

1.5 Organization of the Thesis

This thesis consists of eight chapters which are organized such that the reader is first presented with background theory for an understanding of the subject matter; then an outline of the algorithms and systems developed; next a demonstration of the system over a developing country; analysis, discussions and then conclusions. A brief summary of the contents of each of the remaining seven chapters is outlined in the following paragraphs.

Chapter 2 provides an overview of the fundamental principles of Radar and Synthetic Aperture Radar (SAR) systems. The concept of speckle and methods of reducing its effects are introduced. The characteristics of spaceborne SAR systems are presented before ending with a look at the spaceborne SAR systems to be launched in the near future.

Chapter 3 explores the terminologies and characteristics of elevation models. It provides a brief review of the current methods available for surface modelling, giving an overview of the StereoSAR technique and presents the StereoSAR system developed as part of this research project. The chapter ends with a discussion on the quality assessment of surface models.

Chapter 4 focuses on the digital matching of stereoscopic pairs of SAR imagery by first providing a critical review of the techniques being used for SAR stereo-matching and the current research being conducted in this field. The challenges of matching SAR imagery are outlined and an adaptive matching algorithm developed in this study is presented.

Chapter 5 presents the next critical step in the StereoSAR process, that of Space Intersection. It describes the mathematical models necessary for its development and outlines the space intersection algorithm developed as part of this research. This chapter also presents tests and results conducted on the space intersection algorithm to assess its performance. This chapter also investigated the possibility of using multiple rays for the intersection process and presents the findings of this investigation.

Chapter 6 describes the Nottingham StereoSAR system developed in this research and presents views of the graphical user interfaces used for each module and an explanation of the function of each, the type of input information required and the expected output.

In **Chapter 7**, the main concern is to demonstrate the capabilities of the Nottingham StereoSAR system over the Caribbean island of Jamaica. The chapter starts with a description of the study area and the various datasets used in the research. It explains the choice of stereoscopic image pairs covering the study area for both the Radarsat and Envisat sensors. The validation of the reference surface used for comparisons is described and statistical analysis presented. The adaptive stereo-matching strategy and the GCP-free space intersection algorithm developed in this research were used on the SAR stereoscopic images to generate DSMs over the study area. These were compared with the reference surface and statistical results derived. Critical analysis of these results was conducted and the findings presented.

Finally, **Chapter 8** presents the primary conclusions of the research and recommends possible areas for further research activities.

Chapter 2

Fundamentals of Synthetic Aperture Radar

2.1 Introduction

RADAR is the acronym for *RAdio Detection And Ranging*. Although the word radio exists in the acronym, out of its historical origins, none of the imaging radars today use radio waves. Radar is essentially a distance measuring device operating in the microwave portion of the electromagnetic spectrum using wavelengths from 1mm to 1m. The main feature characterizing microwave signals is that they are capable of penetrating the atmosphere under virtually all conditions (*Lillesand et al. 2004*). The first experiments with Radar waves were conducted as early as 1886 when Heinrich Hertz demonstrated that reflections could be received from metallic and non-metallic objects (*Ulaby et al. 1981)*. By World War II, radars were deployed on airborne platforms for detecting other aircrafts and ships at sea. It was not until the 1950s that the first *Side-Looking Airborne Radars* or SLARs were developed. It was with an advanced SLAR system that the first large scale project for mapping terrain was conducted by the US Army in 1967 over Panama. The region had not been photographed or mapped in its entirety prior to this project, due to persistent cloud cover (*Lillesand et al. 2004*). In 1969 commercial airborne radars became available and they were used extensively for mapping in various parts of the world, primarily for geological applications.

Experiences gained from these airborne Radar systems were used to extend the capabilities of imaging Radars to include spaceborne platforms with the launch of Seasat in 1978 which utilized a technique known as Synthetic Aperture Radar (SAR) for improving image resolution. This continued with the Shuttle Imaging Radar (SIR) and Soviet Cosmos experiments in the 1980s. By the start of the 1990s, Almaz-1, ERS-1 and JERS-1 were launched by the former Soviet Union, the European Space Agency (ESA) and Japan respectively, all within a 12 month period. In 1995, Canada entered the frame with the launch of Radarsat-1, continuing a trend into the new millennium with the short term Shuttle Radar Topographic Mission

(SRTM) and recently ESA's launching of the Envisat satellite. More advanced spaceborne imaging Radar systems are promised for the near future, thus providing a variety of choices for spaceborne Radar data with near global coverage on demand. Further information on the history of Radars can be found in such texts as *Ulaby et al. 1981*; *ASPRS 1998*; and *Lillesand et al. 2004*.

This chapter reviews the fundamentals necessary for an understanding of imaging radars and will be limited to those systems mounted on spaceborne platforms, which is the focus of this study.

2.2 Radar Imaging Principle

The main components of an imaging Radar system are illustrated in Figure 2.1. The imaging principle of a Radar system is best explained by using a *Real Aperture Radar* (RAR) – a system using a fixed antenna length that is attached to the side of the platform.

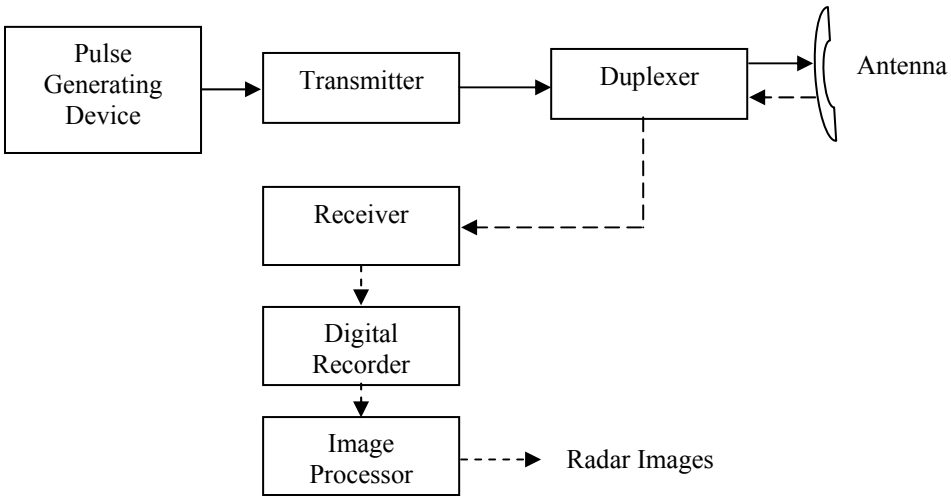

Figure 2.1: *Block Diagram of Imaging Radar System (after Sabins 1997)*

A narrow beam of repetitive microwave pulses at a specific frequency is transmitted through the *antenna*, perpendicular to the direction of flight, towards the earth's surface from the Radar platform. Microwaves are at that part of the electromagnetic spectrum that has wavelengths considerably longer than visible light. The most

common wavelengths used are shown in Table 2.1. Normally each microwave pulse has a duration of between 10 and 50 micro-seconds. On interaction with objects on the surface, the pulses are dispersed in all directions, some of it (the *backscatter*) being reflected towards the antenna and detected by the *receiver*.

Table 2.1: *Designation for Radar Bands, Wavelengths and Frequencies(based on Campbell 2002)*

Band	***Wavelength (cm)***	***Frequency (GHz)***	***Popular Wavelengths (cm)***
X	2.40 – 3.75	12.5 – 8.0	3.0
C	3.75 – 7.50	8.0 – 4.0	6.0
L	15.0 – 30.0	2.0 – 1.0	23.5 or 25.0
P	30.0 - 100	1.0 – 0.3	68.0

A *duplexer* is used to prevent interference between transmitted and received pulses by blocking the receiver circuit during transmission and blocking the transmit circuit during reception. The antenna focuses the microwave pulse in the desired form for transmission and for collecting the backscatter from the earth's surface. The receiver is used to amplify the weak backscatter while preserving the variations in intensity of the reflected pulse. A *digital recorder* is used to store the amplitude, phase and receive time of the backscatter. The amplitude of the backscatter determines the pixel brightness value while the time delays and the speed of light are used to determine the ranges to the terrain objects. Radar processing techniques are then used to generate amplitude/intensity images from the raw data.

Since imaging radars are active systems generating their own illumination using a single wavelength, the resulting image is not in colour as with images from passive optical systems, which are illuminated by various colours (wavelengths) from the visible part of the Electro-Magnetic (EM) spectrum.

2.3 Radar Geometry

The antenna array is located to the side of the platform so that the microwave pulses are transmitted perpendicular to the flight path. The side-looking configuration of the system is to allow better discrimination of the return signal, a feature that has provided advantages for military applications. Each pulse creates a single image line and since the *Pulse Repetition Frequency* (PRF) is ~ 2000 pulses per second, the platform only moves a very small distance to acquire each image line thus building up a two dimensional radar image. The area imaged by the Radar is therefore a *swath* of the earth's surface parallel to and at some distance from the *nadir track* of the platform. Figure 2.2 shows the basic geometry of an imaging Radar system. Unlike other remotely sensed images, the location of pixels in the Radar images is given with reference to the *azimuth time (t)* - the time that particular image line was recorded (scanned), indicated by the along-track direction; and the *range (R)* - distance to the object in the across track direction. It is therefore common to refer to the two dimensional position of an object in a radar image in terms of (*R, t)* coordinates.

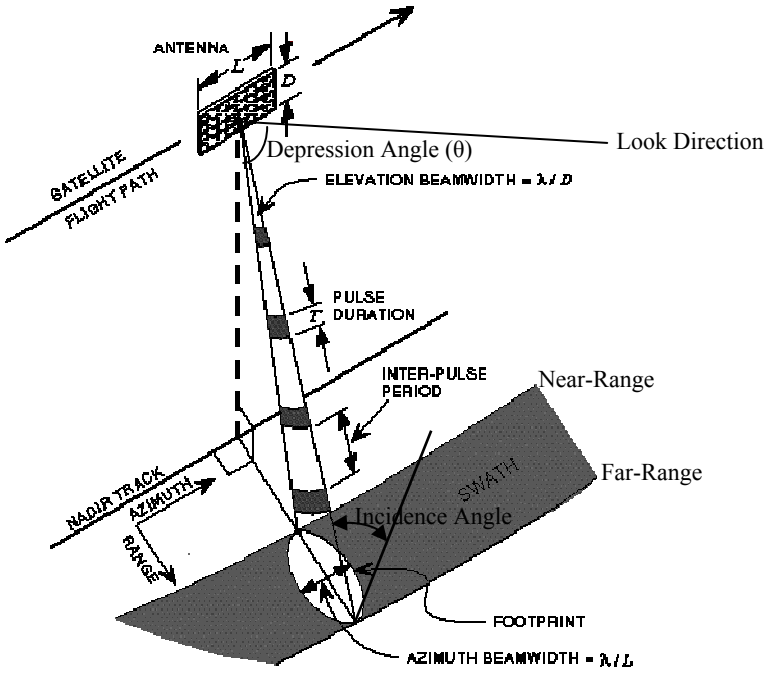

Figure 2.2: *Geometry of an Imaging Real Aperture Radar (RAR) System (ESA 1998)*

The upper and lower edges of the Radar beam define the edges of the image. The *near-range* is the edge closest to the nadir track of the platform usually with the largest depression angle and the *far-range* is the edge furthest from the nadir track of the platform and with the smallest depression angle. Since microwave pulses travel along a straight path from the platform to the earth's surface the computed distance is referred to as a *slant-range*.

2.4 Spatial Resolution of Radar

The spatial resolution of a Radar system is the minimum separation between two objects of equal reflectivity that enables them to appear individually in a processed Radar image (*ESA 2002*). It is related to the size of the smallest area on the earth's surface that is illuminated by the Radar pulse. If the area is large, then the backscatter from different features may be averaged together to form a single pixel value on the image, and their distinctiveness is lost. If on the other hand the area is small, individual features are imaged as separate features and their identities are preserved. In RAR systems, Radar resolution is dependent on pulse duration and antenna beam width (*Lewis and Henderson 1998*). Pulse duration influences resolution in the range direction and antenna beam width determines resolution in the azimuth direction. The combination of range and azimuth resolutions determines the spatial resolution of each pixel on a Radar image.

2.4.1 Range Resolution

The range resolution is the ability of the Radar to distinguish between objects in the across-track or *look* direction of the sensor such that they can be imaged as individual features. It is determined by the depression angle (θ) – the angle between the horizontal plane in the look direction and the slant-range – and by the pulse duration (τ) as shown in Figure 2.3. Range resolution is determined by the following relationship (*Lewis and Henderson 1998*), where c is the velocity of the microwave pulse:

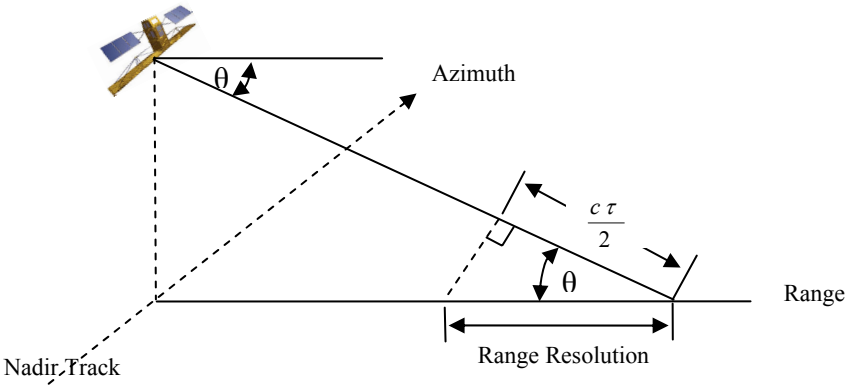

Figure 2.3: *Illustration of Radar Range Resolution*

$$Range\ Resolution = \frac{c\tau}{2\cos\theta} \qquad [2.1]$$

It can be deduced from Equation 2.1 that the shorter the pulse duration τ, the finer the range resolution. Although a short pulse duration may improve the range resolution, it also reduces the total amount of energy in each transmitted pulse. The pulse duration has to be at a level which will ensure that sufficiently strong backscatter is returned from the earth's surface.

2.4.2 Azimuth Resolution

To be resolved, objects must be separated in the azimuth direction by a distance greater than the beamwidth as measured on the earth's surface. The variables influencing azimuth resolution are the physical length of the antenna and the wavelength of the microwave pulse. Azimuth resolution is determined using the following relationship (*Lillesand et al. 2004*) :

$$Azimuth\ Resolution = \beta R = \frac{\lambda R}{L} \qquad [2.2]$$

where λ is the wavelength of the microwave signal; *R* the slant-range; *L* the physical length of the Radar antenna; and λ/*L* defining the azimuth beamwidth (β) as shown in Figure 2.4.

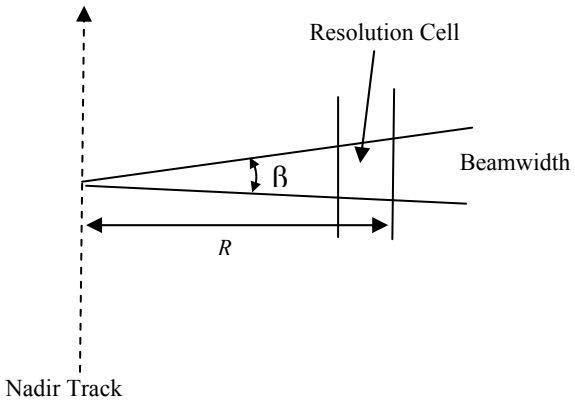

Figure 2.4: *Illustration of Azimuth Resolution Viewed from Above*

Because the range varies from near range to far range, azimuth resolution tends to vary as well, with finer resolution at near range and coarser resolution at far range. From Equation 2.2 it can be construed that azimuth resolution can be improved by either using a short wavelength or a longer antenna. The use of short wavelengths will not be able to attain the desirable effect of penetrating vegetation, clouds and other weather conditions. There are also practical limitations to the maximum antenna length that can be flown on a Radar platform. This restriction on antenna length forms a barrier for the use of RAR systems on spaceborne platforms (*Campbell 2002*).

2.5 Synthetic Aperture Radar Systems

The length of the Radar antenna on board airborne or spaceborne platforms is restrictive. For airborne radars it is usually about 2m while for satellites it is limited to 10 - 15 m. To overcome this limitation, a very long antenna length is electronically "synthesized" by moving a RAR antenna, as shown in Figure 2.5, through a series of

positions along a flight track and recording the Doppler history of the object (example, object **A**) for the entire time they are observed within the radar beam. This synthetic aperture, **B**, is equal to the distance the platform travelled during the integration time.

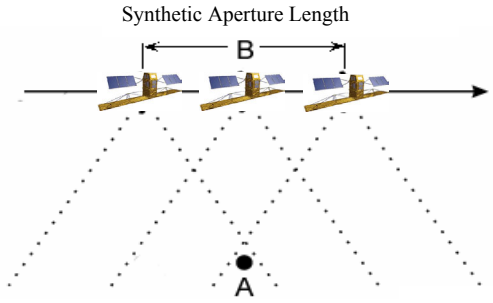

Figure 2.5: *Concept of Synthetic Aperture Radar*

Knowledge of this history is then used to form an image with improved azimuth resolution, which is usually half the length of the fixed antenna for *single look* imagery, i.e. $L / 2$. Where multiple looks are used, as described in section 2.8.1, the azimuth resolution becomes $(NL)/2$ where N is the number of looks (*ESA 2002*; *Lewis and Henderson 1998*). Compared to Equation 2.2, azimuth resolution here is not a function of range R, which implies that the spatial resolution in the azimuth direction is independent of sensor altitude. There is no other remote sensing system with this capability. A system employing this technique is referred to as a *Synthetic Aperture Radar* (SAR) and it is adopted in all modern imaging radars. A full explanation of the SAR systems can be found in radar texts such as *Elachi 1988; Curlander and Mcdonough 1991; Kingsley and Quegan 1992*; *ASPRS 1998*.

2.6 Radar Backscatter

Of primary importance in imaging radars is the signal reflected or *backscattered* from the surface to the antenna. The microwave signal being transmitted is made up of two components: an electric field (E); and a magnetic field (M). The orientation of the electric field determines the *polarization* of the signal which could be either horizontal (H) or vertical (V) as shown in Figure 2.6. Most Radar systems transmit the signal and receive the backscatter in either HH, VV, HV or VH modes; future systems are capable of doing four – quad polarization.

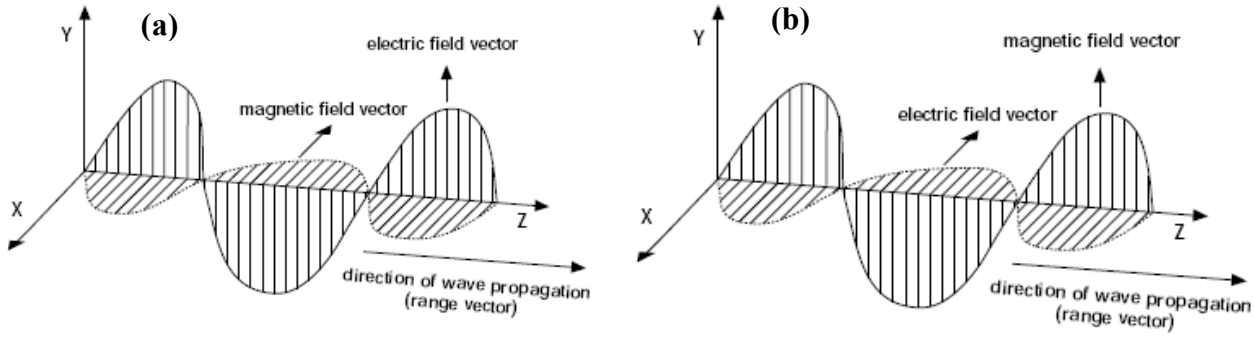

Figure 2.6: *Illustration of a Vertically Polarized (a) and Horizontally Polarized (b) Signal (source: ESA 2002)*

The polarization and amount of backscatter returning to the sensor is dependent on the nature, and specifically the roughness, of the surface that the signal interacts with. Figure 2.7 shows possible backscatter scenarios. Very smooth objects do not return any backscatter and therefore appear black in the imagery, while corner reflectors (such as walls) return strong backscatter and appear white. Other levels of backscatter are given by shades of grey.

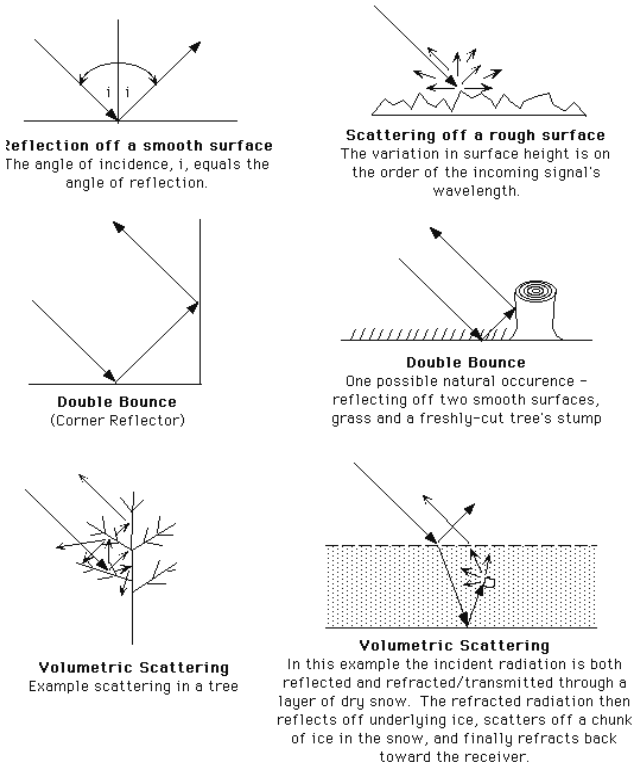

Figure 2.7: *Backscatter of radar signal from various terrain objects (ESA 2002)*

In vegetated areas, the point from which backscattering occurs depends to a great extent on the wavelength assigned to the microwave pulse (see Table 2.1). Figure 2.8 illustrates the effect of different wavelengths. With the X-band there is little penetration of the canopy and one can expect that the image generated will show the tops of the canopy. The C-band generates more penetration into the foliage while the L-band is capable of penetrating deep into the foliage to return the bare earth surface. A combination of data from the X- and L-band will be able to provide information on forest heights.

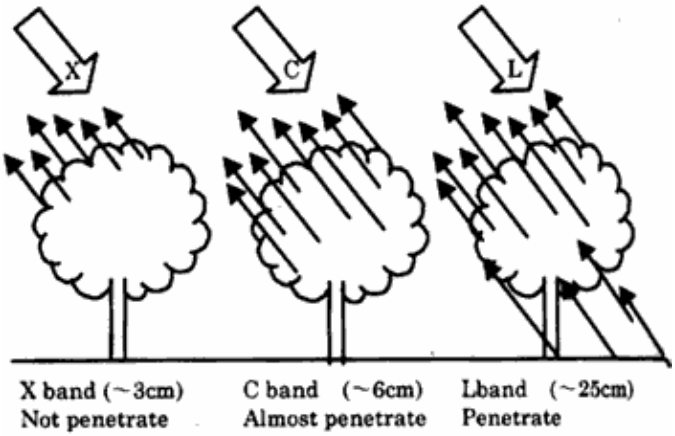

Figure 2.8: *Backscatter of radar signal from various terrain objects (Sowter 2005)*

The parameters influencing the brightness of a terrain object on a radar image are given by the *radar equation (Campbell 2002)*:

$$P_r = \frac{P_t G^2 \lambda^2 \sigma}{(4\pi)^3 R^4} \qquad [2.3]$$

Where:

P_r = Power received

P_t = Power transmitted

G = Antenna Gain

λ = Wavelength

R = Range from antenna to object

σ = Radar Cross-Section (RCS)

All the parameters in Equation 2.3 can be determined in the radar design process except the RCS which is determined by the specific characteristics of the terrain surface. It is this quantity that carries the most information about the terrain and is generally given in a normalized form referred to as *sigma nought* (σ^0) usually specified in decibels (dB):

$$\sigma^0 dB = 10 * \log_{10}(RCS / A) \qquad [2.4]$$

where A is the area of ground imaged by the radar. Typical values of σ^0 for natural surfaces are from + 5 dB (bright) to - 40 dB (dark). A method of stretching the SAR image was developed using the value of σ^o computed based on formulas in *RSI 2000* and then converted to a 0-255 brightness range. This newly developed stretching method, called *sigma nought* stretch, is illustrated in Figure 7.13(d).

2.7 Geometric Effects on SAR Images

Since radar images are made up of ranges to the objects, they are likely to be affected by geometric distortions such as: *foreshortening, layover* and *shadows*. Because the radar is a side-looking sensor, the ranges are usually measured in a slant configuration (hence the term *Slant-Range*). This results in slopes facing the sensor to be compressed (or foreshortened) while slopes facing away from the sensor are stretched as illustrated in Figure 2.9(a). Here *a*, *b* and *c* define a hill symmetrical in cross-section with front slope α. When recorded in a slant-range geometry, the front

slope distance *ab* is recorded in the image plane as *a'b'* showing a compression while the back slope *bc* represented by *b'c'* in the image plane shows some stretching. Layover occurs where the microwave pulse travelling to the top of the terrain object is recorded before the pulse travelling to the bottom of that object as shown in Figure 2.9(b). This usually occurs with a larger slope angle α, such that the front slope *ab* is steeper than the back slope *bc*. This causes *ab* to be recorded as *b'a'* in the image plane. Radar shadows result where, because of topography, the radar beam is unable to illuminate parts of the terrain making those areas appear dark. This is usual in terrain where the back slopes are steeper than the fore slopes as illustrated in Figure 2.9(c).

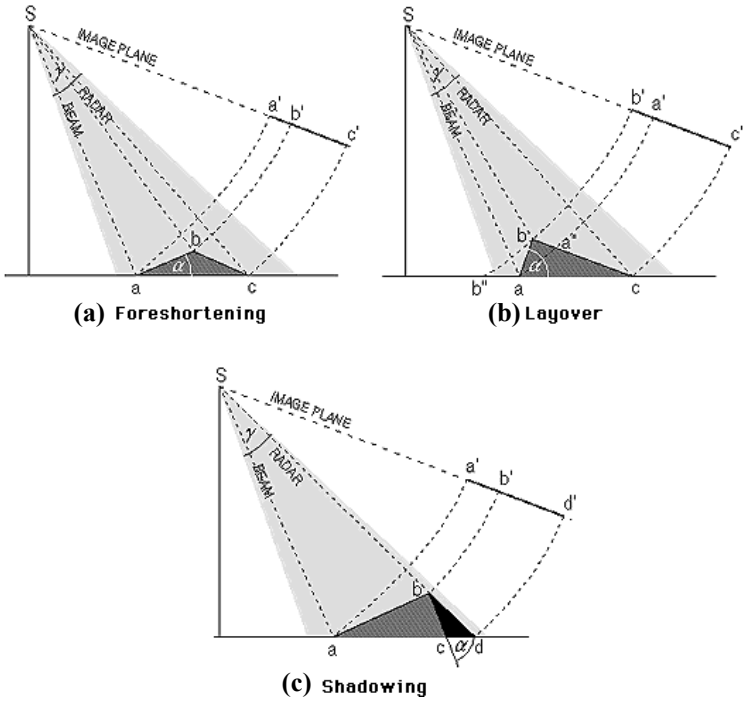

Figure 2.9: *Geometric Effects on Radar Images(ESA 2002)*

2.8 Speckle Noise

Radar is a coherent system, which means that it transmits and receives signals of the same wavelengths. The microscopic scattering of these signals returning from spatially extensive targets cause interference in the resolution cell (pixel) and this interference manifests itself as a sort of "salt and pepper" effect which is usually

referred to as *speckle noise*. It has been verified in several works that the standard deviation of the signal is proportional to its mean over homogeneous areas (*Lee 1981*) which suggests the use of a multiplicative model for representing speckle:

$$I(n) = R(n) \cdot F(n) \qquad [2.5]$$

where $I(n)$ is the measured value for an image pixel n, $R(n)$ is the true scene reflectivity at that point and $F(n)$ is the multiplicative noise process (speckle). The presence of speckle in a SAR image forms an obstacle to the extraction of topographic information and some form of pre-processing of the images to suppress or ensure its removal must be taken into account in the development of any stereo-matching strategy.

Many speckle reduction techniques have been proposed ever since the concept of speckle was presented by *Goodman 1976* and the most common are: multi-look processing (see *RSI 2000*); the use of non-adaptive speckle filters (see *Tso and Mather 2001*); and the commonly used technique of adaptive speckle filtering such as Lee, Kuan, Frost and Gamma-Map. The full removal of speckle noise without losing information in SAR images is still a long way off (*Huang et al. 2000*). As yet, there is no speckle filter that is appropriate for all Radar images. A complete statistical description of speckle noise and reflectivity models used in speckle filtering can be found in *Lopes et al. 1993*.

2.8.1 Multi-Look Processing

The effect of speckle in a Radar image can be suppressed by averaging several images (looks), formed using smaller aperture lengths, to reduce the noise variance; a process usually referred to as *multi-look processing*. It is essentially a signal processing procedure requiring sophisticated hardware and software and is therefore usually performed by the data provider. The number of 'looks' used in the averaging process determines the amount of speckle that will be reduced in the resulting image; the greater the number of looks the more reduction in the effects of speckle, however, this comes at a cost because it also leads to a degradation in the spatial

resolution of the Radar image. The relationship between real aperture length L, spatial resolution r, and the number of looks N, is given by the following equation (*Ulaby et al. 1981*):

$$N \approx \frac{r}{0.5L} \qquad [2.6]$$

For example, if real aperture length is 10m and the worst spatial resolution that would be acceptable is 25m, then the number of 'looks' required would be 5.

2.8.2 Non-Adaptive Speckle Filters

Non-adaptive speckle filters are those that use the same set of rules for the entire image regardless of differences in image texture, contrast, etc. The most common filters make use of the statistical mean or median computed from a fixed size moving window. Since these filters use basic statistical models, they have the advantages of being easy to implement, do not require a lot of computer time and produce results quickly. The main disadvantage, however, is that they do not take into account the principles relating to the formation of the SAR imagery and therefore do not produce the best results. They may work well with additive Gaussian noise but are unsuitable for the multiplicative nature of SAR speckle noise.

With a statistical mean based filter, the image is convolved with a predetermined kernel by moving the fixed size window, say n x n, across the image pixel by pixel and substituting the digital number (DN) of the pixel in the centre of the window with the mean of all n^2 pixels in that window. Kernel sizes can range for 3x3, 5x5, 7x7, 9x9 or larger, but the larger the size the more smoothing is done to the image. An example of a 5x5 mean filter is shown in Equation 2.7.

$$\frac{1}{25}\begin{bmatrix} 1 & 1 & 1 & 1 & 1 \\ 1 & 1 & 1 & 1 & 1 \\ 1 & 1 & 1 & 1 & 1 \\ 1 & 1 & 1 & 1 & 1 \\ 1 & 1 & 1 & 1 & 1 \end{bmatrix} \qquad [2.7]$$

The median filter operates similar to the mean filter, but instead of substituting the centre pixel with an average, it replaces the centre pixel with the median value of the n^2 pixels in the window. The advantage of this filter over the mean is that the pixel value is always replaced with a DN value from the dataset and not one that is computed. This filter is also more effective over the mean filter because it tends to preserve step edges and the output is not affected by spurious DN values in the window, thus making it effective in eliminating spike noises. For further information on non-adaptive filters the reader is directed to some of the most common remote sensing and image processing text, for example, *Mather 2001*.

2.8.3 Adaptive Speckle Filters

In contrast to non-adaptive filters, adaptive filters tend to preserve the subtle image information. These adaptive filters should be able to smooth speckle in homogeneous areas while preserving texture and high frequency information in heterogeneous areas. It may not always be possible for filters to achieve these two requirements and at times there will have to be a trade-off between requirements (*Shi and Fung 1994*). Numerous adaptive filters have been proposed in the last few years that have achieved, to some degree, the suppression of speckle in SAR imagery. Most adaptive filters are formulated based on three main assumptions (*Lee 1980*): (a) SAR speckle is modelled as a multiplicative noise (see Equation 2.5); (b) the noise and signal are statistically independent; and (c) the sample mean and variance of a pixel is equal to its local mean and local variance computed within a window centred on the pixel of interest. The most common adaptive speckle filters are described in the following paragraphs.

- **The Lee Filter**

  This filter developed by Lee (see *Lee 1980*; *Lee 1981* and *Lee 1986*) first approximates the multiplicative noise model in Equation 2.5 as a linear model and then applies the minimum mean square error (*MMSE*) criterion to the linear model. The resulting DN value, R, for the filtered pixel that is generated based on statistics derived from a fixed size moving window over the image is given by Equation 2.8.

$$R = Ic \times W + \mathrm{Im} \times (1 - W) \qquad [2.8]$$

where:

$W = 1 - \frac{Cu^2}{Ci^2}$, used as a weighting function

$Cu = \sqrt{\frac{1}{L}}$, an estimate of the speckle variation coefficient

$Ci = \frac{\sigma}{\mathrm{Im}}$, the image variation coefficient

Ic = center pixel of the filter window

Im = mean value of DNs within the filter window

σ = standard deviation of DNs within the filter window

L= number of looks

- **The Kuan Filter**

In Kuan's approach (*Kuan et al. 1985*), the multiplicative noise model (Equation 2.5) is first transformed into a signal dependent additive noise model then the *MMSE* criterion applied to this additive model. The resulting speckle filter has a similar form to the Lee filter as in Equation 2.8, but with a different weighting function given by:

$$W = \frac{1 - \frac{Cu^2}{Ci^2}}{1 + Cu^2} \qquad [2.9]$$

Since the Kuan filter makes no approximation to the original noise model it can be considered to be superior to the Lee filter (*Shi and Fung 1994*).

- **The Frost Filter**

The Frost filter (*Frost et al. 1982*), also based on the multiplicative noise assumption, uses an exponentially damped convolution kernel which adapts itself to features based on local statistics. This filter differs from the Lee and Kuan filters in that the reflectivity of the scene is estimated by convolving the image with the impulse of the SAR system. The Frost filter is outlined in Equation 2.10 which shows the resulting DN value, *R*, for the filtered image pixel using an *n x n* window.

$$R = \frac{P_1 \times W_1 + P_2 \times W_2 + ... + P_n \times W_n}{W_1 + W_2 + ... + W_n} \qquad [2.10]$$

Where:

P_i = DN for each pixel in the *n* x *n* window (i = 1…..n)

$W_i = \exp(-K \times Ci^2 \times |t|)$, the weighting function

K = is the exponential damping factor

$Ci = \frac{\sigma}{\mathrm{Im}}$, the image variation coefficient

σ = standard deviation of DNs within the filter window

Im = mean value of DNs within the filter window

$|t|$ = absolute value of the pixel distance from the centre pixel to its neighbours in the filter window

- **The Gamma Map Filter**

The Maximum A-Posteriori (MAP) approach to speckle reduction was first proposed by *Kuan et al. 1987* where they assumed a Gaussian distribution for probability density function (PDF) of the scene. This was not quite accurate since it implicitly assumed a negative reflectivity (*Shi and Fung 1994*). *Ulaby et al. 1986b*b have indicated that the PDF follows a Gamma distribution for multi-look SAR images. The Kuan MAP has since been modified by *Lopes et al. 1990a* by assuming that the scene has a Gamma distribution.

The well known filters like the Lee, Frost and Kuan, described previously, weight the central pixel value and neighbouring pixel values (Frost) or local mean (Lee and Kuan) as a function of the local coefficient of variance *Ci*. This allows some texture preservation although no texture model is introduced. Noise is not well suppressed along linear features or around point targets because *Ci* can take high values within the fixed window around the central pixel value (*Nezry et al. 1991*).

With the Gamma MAP filter, the *Ci* is adapted such that it is able to detect whether the pixel to be filtered lies within a homogeneous area or a heterogeneous area; heterogeneity is considered to exist if $Ci < Cu$. *Lopes et al. 1990b* suggests an upper threshold for the maximum *Ci* not to exceed $\sqrt{2} \times Cu$, beyond which a gamma distribution would no longer be valid for the scene. The Gamma Map filter is given by Equation 2.11 showing the resulting DN value, *R*, for the filtered image pixel using an *n* x *n* window.

$$R = \begin{cases} Im & for\ Ci <= Cu \\ (B \times \mathrm{Im} + \sqrt{D})/(2 \times A & for\ Cu < Ci < Cmax \\ Ic & for\ Ci <= Cu \end{cases} \qquad [2.11]$$

Where:

$Cu = \sqrt{\frac{1}{L}}$, an estimate of the speckle variation coefficient

$Ci = \frac{\sigma}{\mathrm{Im}}$, the image variation coefficient

$Cmax = \sqrt{2} \times Cu$

Ic = center pixel of the filter window

Im = mean value of DNs within the filter window

σ = standard deviation of DNs within the filter window

L = number of looks

$A = \frac{1 + Cu^2}{Ci^2 - Cu^2}$

$$B = A\text{-}L\text{-}1$$
$$D = I_M^2 \times B^2 + 4 \times A \times L \times I_M \times Ic$$

A study by *Paudayal and Aschbacher 1993* was carried out to investigate the performance of these adaptive filters. The study also included the mean and median filters. The performance of the filters was assessed based on their ability to improve the signal-to-noise ratio (mean/standard deviation) and the preservation of linear features as well as small strong scatters. Their results showed that the best overall performance was achieved using the Gamma MAP filter. A comparison of these adaptive filters was also conducted by *Shi and Fung 1994* and their results showed that the Frost filter performed the best in preserving edges and linear structures. From their study it is clear that the choice of a speckle filter is dependent on the radar application.

2.9 Spaceborne Imaging Radars

The development of Synthetic Aperture Radar (SAR) provided opportunities for advances in compact systems capable of acquiring fine spatial detail at high altitudes, most of which are flown on spaceborne platforms. These spaceborne imaging Radars can be placed into two categories: those that use a fixed antenna pointing, leading to fixed incidence or look angle – single beam mode – for data acquisition and those that use multiple beam modes which provide a range of incidence angles that the user can choose from and are capable of highlighting different characteristics of the terrain.

As mentioned in section 2.1, several spaceborne imaging Radars have been deployed since the launching of Seasat in 1978. Although this mission lasted approximately four months, due to an electrical system failure, invaluable experience and knowledge were gained that led to the development and deployment of other spaceborne imaging Radars such as: Shuttle Imaging Radars (SIR), ERS-1, ERS-2, JERS-1, Radarsat-1 and more recently Envisat. In this study, the sensors selected were Radarsat-1 and Envisat. The main reasons for choosing these sensors were because they are the only Radar satellites in space, at present, capable of routinely

imaging the earth's surface using multiple incidence angles (10^{o}-60^{o}) and varying spatial resolutions (8m – 100m), characteristics which are advantageous for stereo applications. The use of multiple incidence angles also shortens the revisit time of the sensor, depending on the pairing of imaging modes, thus minimizing the dissimilarity between images due to temporal change. Table 2.2 gives a summary of the main characteristics of the single beam mode Radars, while the following sections present an overview of the Radarsat-1 and Envisat Radars. More detailed information on spaceborne imaging Radars can be found in such texts as *ASPRS 1998*; *Mikhail et al. 2001*; *Campbell 2002*; and *Lillesand et al. 2004*.

Table 2.2: *Summary of Characteristics of the Main Single Beam Spaceborne Imaging Radars*

Imaging Radar	Launch	Look Angle (deg)	Resolution (m)	Swath Width (km)	Band	Polarization
Seasat	28-Jun-78	20	25	100	L	HH
SIR-A	12-Nov-81	40	40	50	L	HH
SIR-B	05-Oct-84	15 – 60	17 – 58	40 – 50	L	HH
ERS-1	25-Jul-91	23	25	100	C	VV
JERS-1	11-Feb-92	35	18	75	L	HH
ERS-2	20-Apr-95	23	25	100	C	VV

2.9.1 Radarsat -1

Radarsat is a joint project of the Canadian and United States governments and private corporations (*Campbell 2002*) with Canada being responsible for the design, control, and operations of the entire system and the United States, through NASA, providing launch services. The satellite was launched on the 28th November 1995 with a life expectancy of 5 years and at the time of writing this thesis it was still fully functional. According to *Bach 2003*, the accuracy of the satellite orbit is: 100m along-track, 20m across-track and 20m radial. Figure 2.10 shows the Radarsat satellite.

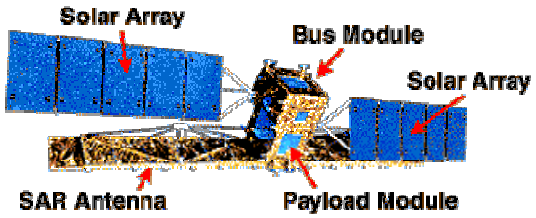

Figure 2.10: *The Radarsat Satellite (Source: www.ccrs.nrcan.gc.ca)*

The Radarsat-1 SAR sensor is right looking, operating at various look angles and swath widths thus giving the sensor the ability to revisit polar regions on a daily basis and mid-latitude regions every 3 days. The revisit time for the same beam mode is usually 24 days. The satellite was launched into a sun synchronous orbit with inclination of ~ 98°, an altitude of ~ 800km, and an orbit period of 100.7 minutes (*Lillesand et al. 2004*). This SAR system operates in the C-band with a wavelength of 5.6cm and is configured to detect HH polarized signals. Figure 2.11 illustrates the beam modes available from Radarsat-1 and Table 2.3 summarizes the swath width, resolutions and look angles that characterize the system.

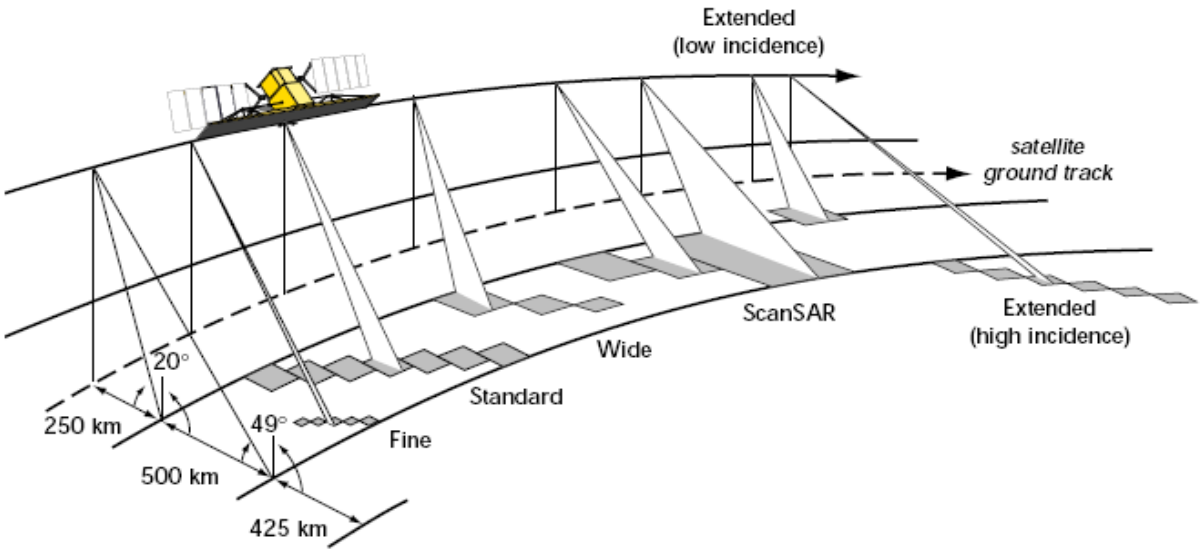

Figure 2.11: RADARSAT Imaging Modes (after RSI 2000)

Table 2.3: *Summary of Radarsat-1 Beam Mode Characteristics (adapted from Lillesand et al. 2004)*

Beam Mode	*# of Beam Positions*	*Swath Width (km)*	*Look Angle (deg)*	*Spatial Resolution (m)*	*# of Looks*
Standard	7	100	20-49	25	4
Wide	3	150	20-39	30	4
Fine	5	45	37-48	8	1
Extended High	6	75	50-60	25	4
Extended Low	1	170	10-23	35	4
ScanSAR Narrow	2	305	20-46	50	2-4
ScanSAR Wide	1	510	20-49	100	4-8

2.9.2 Envisat ASAR

The launching of the ENVIronmental SATellite (Envisat) on 1st March 2002 continued the development cycle of the European Remote Sensing (ERS) satellites ERS-1 and ERS-2. Among the instruments onboard Envisat is an Advanced Synthetic Aperture Radar (ASAR) system with a phased-array antenna capable of retrieving a variety of geophysical measurements on a global scale (*ESA 2002*). Improvements over its predecessors ERS-1 and ERS-2 include: beam steering to acquire images with different incidence angles; dual polarization; and wide swath coverage. This new sensor (see Figure 2.12) is expected to make significant contributions to the geosciences including, but not limited to, soil moisture monitoring; surface deformations; and more importantly topographic mapping.

Figure 2.12: *The Envisat Satellite (source: www.hero.ac.uk)*

Launched into a sun synchronous orbit at an altitude of ~ 785 km and transmitting microwave signals in the C-band at 5.331 GHz, illuminating the earth's surface from the right side of the satellite platform, the Envisat ASAR sensor acquires images using 5 operating modes: Image Mode; Alternating Polarisation Mode; Wide Swath Mode; Global Monitoring Mode; and Wave Mode. For topographic mapping the Image Mode is the one usually used with a HH polarization and a spatial resolution of ~ 30m (*ESA 2002*). Experiments conducted by *Otten and Dow 2004*, on Envisat orbits, showed the precision of the best estimate to be around 10cm (3D) with a 3 cm radial accuracy. Figure 2.13 shows the operating modes of Envisat and their main characteristics are summarised in Table 2.4. Full explanations on these modes of operation can be found in *ESA 1998* and *ESA 2002*.

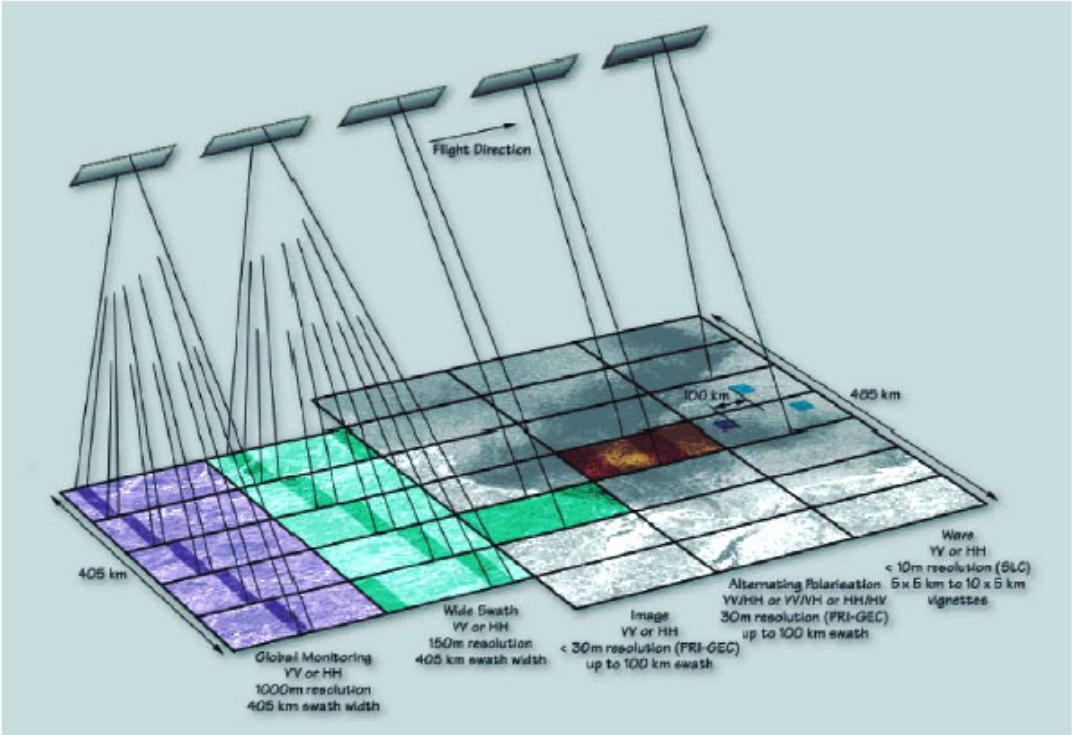

Figure 2.13: *Envisat ASAR Operating Modes (Source: ESA 1998)*

Table 2.4: *Summary of Envisat Operating Mode Characteristics (Based on ESA 1998)*

Mode	***Polarisation***	***Swath Width (km)***	***Look Angle (deg)***	***Spatial Resolution (m)***	***# of Looks***
Image	VV or HH	56 - 105	15 - 45	30	4
Alternating Polarisation	VV and HH HH and HV VV and VH	56 - 105	15 - 45	30	2
Wide Swath	VV or HH	405	17 - 42	150	12
Global Monitoring	VV or HH	405	17 - 42	1000	7 - 9
Wave	VV or HH	5	15 - 45	10	1

2.9.3 Future Stereo-Related SAR Missions

Radarsat-2

The Radarsat-1 satellite will be followed by Radarsat-2, scheduled for launch in 2006. The orbital characteristics remain the same as Radarsat-1, but the new satellite has a design life of 7.5 years. When fully operational it will be the most advanced commercial satellite in space offering spatial resolution of up to 3m, the highest from any spaceborne Radar platform.

The improvements made to this satellite include: GPS receivers on board for more accurate orbit determination, leading to improved geometric accuracy without ground control; the ability to look either to the right or left of the satellite track (see Figure 2.14) further increasing revisit times and generating faster responses to user requests; full polarimetric imaging modes allowing the user to select between HH, VV, HV and VH polarizations thus increasing the information content and its applicability for various applications such as agriculture, target identification, marine monitoring, and mapping/geology; and the inclusion of an ultra-fine mode which would provide improved object detection and recognition further enabling a variety of new applications.

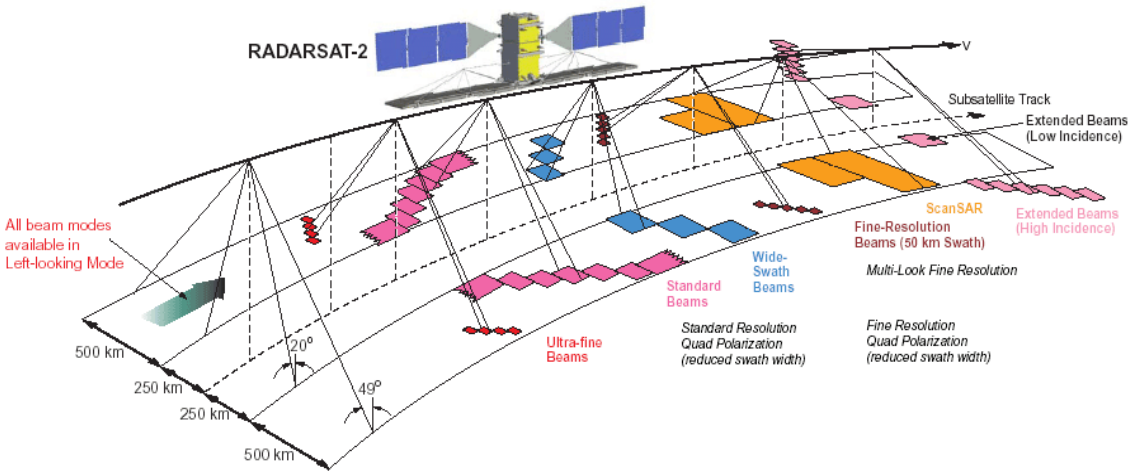

Figure 2.14: *Proposed Radarsat-2 Operating Modes (Source: www.radarsat2.info)*

ALOS PALSAR

The Phased Array type L-band Synthetic Aperture Radar (PALSAR) sensor flown onboard the Advanced Land Observing Satellite (ALOS) is a joint project between Japan Aerospace eXploration Agency (JAXA) and Japan Resources Observation System Organization (JAROS) following on from the Japanese Earth Resources Satellite-1 (JERS-1) mission. The satellite is scheduled for launch in the summer of 2005 and will be placed in a sun-synchronous orbit with an altitude of ~ 700 km, an inclination of 98.2^{o} and repeatability of 42 days. The sensor will operate in the L-band with a wavelength of 23.5 cm utilizing multiple incidence angles ranging from ~ 8 to 60 degrees and HH, HV, VH, VV polarizations. The multiple incidence angles will decrease the revisit times to ~ 2 days at near-polar regions. The spatial resolutions are expected to be ~ 7 – 44m in Fine Mode; 100m in ScanSAR Mode; and 24 – 89m in Polarametric Mode. Figure 2.15 illustrates the beam modes and characteristics of the PALSAR sensor. For more information see http://www.eorc.jaxa.jp/ALOS.

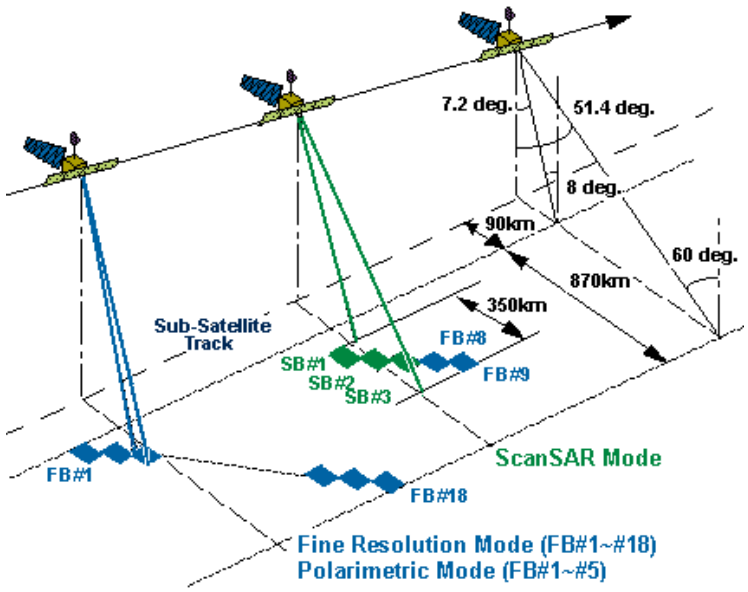

Figure 2.15: *ALOS PALSAR Operating Modes (Source: www.eorc.jaxa.jp)*

2.10 Summary

The fundamentals for an understanding of SAR have been reviewed in this chapter. Radar operates in the microwave portion of the electromagnetic spectrum and generates its own illumination making it capable of penetrating cloud cover and observing day or night. However, the images are usually corrupted by speckle noise and to date there are no speckle filters that can remove this noise completely for all types of datasets; yet the mathematics behind the common speckle filters in use today have been outlined. The geometry and characteristics of spaceborne SAR systems have been presented and a brief overview of the future stereoscopic multi incidence angle SAR systems was accomplished.

Chapter 3

Surface Modelling Using StereoSAR

3.1 Introduction

With the advent of Geographic Information Systems (GIS), the need for topographical information has been on the increase and cost effective methods for providing this information are well sought after. Traditionally, topographic information was represented in the form of contour maps and these were created using ground surveying or photogrammetric techniques. More recently, approaches using Global Positioning Systems (GPS) and Light Detection And Ranging (LiDAR) have been adopted. It has been widely accepted that for generating topographic information of large areas, for example an entire country, the most economical method is the use of airborne or spaceborne sensors.

A growing body of research work has focused on the digital modelling of the earth's surface using airborne or spaceborne sensors. These research activities can be categorised into three approaches: (a) those methods that use range information directly provided by an active sensor e.g. LiDAR (see *Smith et al. 2000*) and Radar altimetry (see *Berry 2000*); (b) those methods that use only single images such as clinometry or shape-from-shading (see *Toutin and Gray 2000*); and (c) techniques using two or more datasets taken from different recording positions and possibly on different days using either optical or microwave sensors. This research is primarily concerned with the third option based on data acquired from spaceborne microwave sensors, specifically Radarsat and Envisat satellites. This area can be further subdivided into: Stereoscopic SAR (StereoSAR) or Interferometric SAR (InSAR) based on the specific common technique used to extract the topographic information.

In this chapter, a critical review of the techniques for generating topographic information will be outlined before presenting details on the StereoSAR technique, which is the subject of this research project, and issues surrounding the use of this technique. A critical review of the methods for assessing the quality of surface models is also given at the end as knowledge of model quality is important.

3.2 What is a Surface Model?

The main purpose of generating topographic information is to be able to produce a digital description of the relief of a particular area thus characterizing the nature of the surface of the area of interest, whether its extents are site specific or reach the national or global level. Many applications today demand digital characterization of the earth's surface in a variety of formats. Terms such as *DEM*, *DSM* and *DTM* have been associated with different categories of models of the surface of the earth.

A Digital Elevation Model (***DEM***) is a generic term used to refer to any model comprising of elevations that characterize the surface of the earth without making any distinction of the features it represents. A Digital Surface Model (***DSM***) therefore, is a special case of a DEM representing the first surface 'seen' by the sensor and will describe not only the bare surface of the earth but also all the natural and man-made objects on it, including vegetation, buildings, etc. A Digital Terrain Model (***DTM***) on the other hand, is also a special case of a DEM, but one which represents only the bare-earth. It is essentially a DSM with all above ground features stripped off to reveal the bare-earth (see Figure 3.1).

In this research, the SAR sensors utilized image the first surface of the earth, and no attempt is made here to strip away any features from the elevation models generated, thus giving rise to a DSM. Therefore, for this study, the focus is on generating DSMs and the terms surface model or elevation model may be used interchangeably throughout this thesis. Several characteristics can be used in describing a surface model, examples are: the structure used to store the data (Grid, TIN, etc); the spatial resolution; and the interpolation method used. These are briefly discussed below.

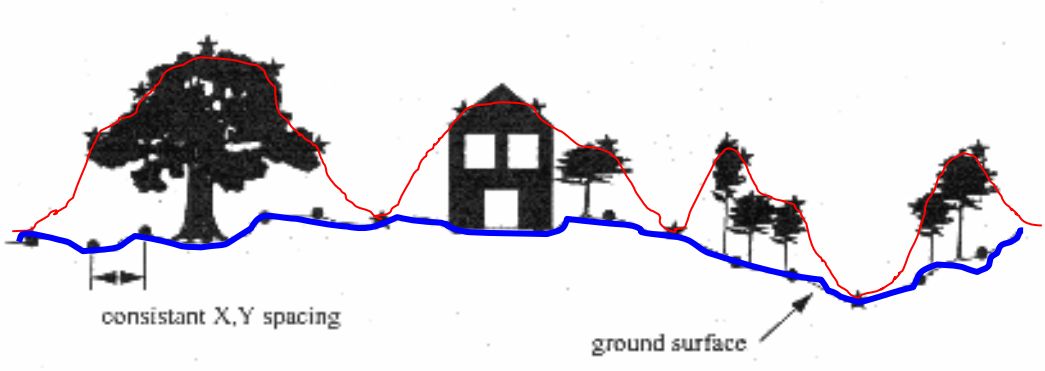

Figure 3.1: *Distinction between DSM (red) and DTM (blue) surfaces*

- ***Data Structures***

  The most common DEM data structure is the raster or grid structure. Graphically, these normally consist of a matrix of square grid cells with the mean cell elevation stored in a two dimensional array. Location of a cell in geographic space is implicit from the row and column location of the cell within the array, provided that the boundary coordinates (geo-referencing) of the array are known. Grid DEMs are widely available and used because of their simplicity, processing ease and computational efficiency (*Martz and Garbrecht 1992*). Limitations include: grid size dependency of certain computed topographic parameters (*Fairfield and Leymarie 1991*) and inability to locally adjust the grid size to the dimensions of topographic land surface features. Other DEM data structures, such as the Triangulated Irregular Network (TIN) and contour-based structures, have overcome some of the disadvantages of grid DEMs; however, they have shortcomings of their own and are not as widely available as grid DEMs. Choice of data structure will depend on data availability, nature of surface being modelled and the techniques that will be used to analyse and manipulate model scale and resolution of the data and problem. Although the grid DEM is the most commonly used data structure it is rarely the structure used to capture data. The data is normally captured in a way that is appropriate to the technology being used and in the end a regular grid is then interpolated. The regular grid interval should be commensurate with the density of the data capture so there is minimal reduction in quality. Of course, the data capture density should be commensurate with the required level of detail.

- ***Resolution***

  The concept of spatial resolution is well developed in the field of remote sensing, where it is defined in terms of the ground dimensions of the element or pixel making up the dataset. For DEMs, resolution refers to the size of the grid cell used to represent the surface being modelled and relates to the size of the smallest feature that can be represented and detected in the elevation model. For a discussion on Radar resolution see section 2.4.

- ***Interpolation***

  When the topographic data is collected it may not represent a continuous surface or represent the area of interest. The method of converting the discrete points collected into a continuous surface is referred to as surface interpolation. Several algorithms exist for this purpose and the most popular are: kriging, nearest neighbour, inverse distance weighted and spline. Many elevation modelling packages offer a choice of interpolation methods. However, the user should be aware that the accuracy of a selected method will depend on the accuracy of initial point measurements, density and distribution of the raw data. The reader is directed to *Burrough and McDonnell 1998* and *Watson 1994* for more information on the different interpolation algorithms.

3.3 Current Surface Modelling Methods

Several approaches exist for the collection of data and the generation of models of the earth's surface with each method having its own merits and limitations. In addition, each area of interest has its own specific set of conditions which will render certain techniques more suitable than others. Sometimes, it may be necessary to use a combination of different methods or even specifically design methods in some extreme cases. The selection of a particular technique will rely on: the accuracy required; the extent of the area of interest; the budget; time frame; the modelling objective; etc. The following sections outline some of the common methods used for elevation data collection and modelling.

3.3.1 Cartographic

Essentially, the cartographic method involves the production of elevation models by digitizing or scanning the contour lines and spot heights on an available topographic map of the area of interest. Once this data has been converted to a digital format it can be interpolated using one the methods mentioned earlier. Since these contour lines and spot heights normally represent bare earth surfaces, the product generated is

a DTM. This approach is usually relatively inexpensive; however, its accuracy depends greatly on the quality of the map and the skill of the operator digitizing the data. Also, the contours are widely spaced in low lying areas which do not give a good representation of the surfaces in these areas and contain less spatial detail when compared to other methods. The greatest disadvantage with this method comes from interpolation in the gridding process which tends to leave terracing artefacts in the digital model (see Figure 3.2). Further information on the Cartographic technique can be found in *Kennie and Petrie 1990*.

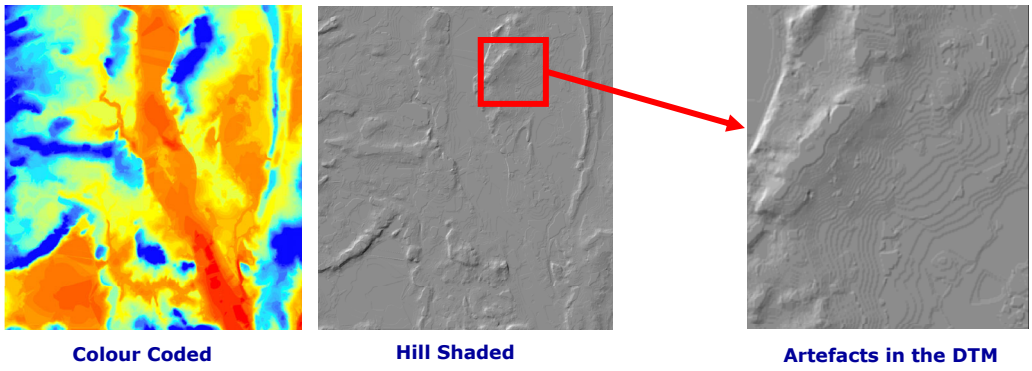

Figure 3.2: *DTM Generated from Contours Showing Artefacts (Source: OS LandForm Profile)*

3.3.2 Ground Surveying

These techniques require that observations for elevation models be made directly in the field. The current approaches for achieving this are: Conventional total station surveying; and Global Positioning Systems (GPS). The objective is to acquire appropriate measurements at every point requiring 3D national grid coordinates (Northing, Easting and Height). These points are usually conveniently placed across the terrain and will have to be re-sampled into a regular grid using one of the interpolation methods mentioned earlier. These techniques are the most accurately available to date giving better than ± 5 cm accuracy, however, they can require lengthy field work making them potentially costly and therefore unsuitable for elevation generation over large areas. They do, however, play an important support role for other techniques by providing control information, validation data and filling in data voids. GPS is probably the most used technique today and Figure 3.3 gives and example of it in use; it however requires an unobstructed view of the sky at all times thus limiting its use in densely vegetated areas.

The principles of GPS and its limitations are well documented in many books and papers, for example: *Hoffman-Wellenhof et al. 1994*; *Kaplan 1996*; *Leick 1995*; *Wells 1989* and *Rizos 1997*. Information on the use of total stations can be found in any standard surveying text, for example *Kavanagh 2003* and *Bannister et al. 1998*.

Figure 3.3: *Ground Surveying Using GPS Techniques*

3.3.3 LiDAR

Since 1994, a new technology for terrain modelling has been made available to the mapping community and is commonly referred to as LiDAR (Light Detection And Ranging). A LiDAR system (see Figure 3.4) is based on the combination of three different data collection tools: a laser scanner mounted on an aircraft or helicopter platform; a GPS receiver/antenna used in kinematic mode to provide the sensor position; an Inertial Measurement Unit (IMU or INS) to provide the orientation; and a data processing and storage unit.

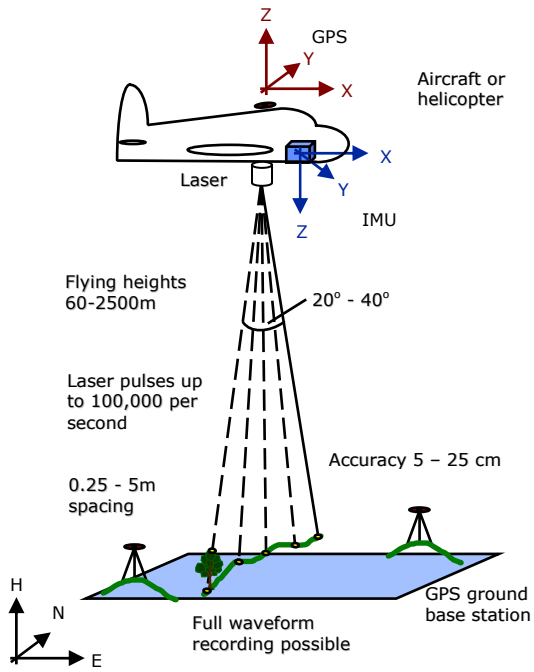

Figure 3.4: *Typical LiDAR System and its Main Components (after Smith 2005)*

In typical standard conditions, taking into account the flight (speed 200–250 km/hour, altitude 500–2,000 m) and sensor characteristics (scan angle ± 10–20 degrees, emission rate 2,000–100,000 pulses per second), terrain elevations are collected within a density of at least one point every 0.25–5 m with an accuracy of ± 15 cm. The technology therefore allows the generation of accurate and high resolution surface models suitable for many applications. However, LIDAR data acquisition is dependent on favorable weather conditions and the data processing requirements are considerable. Therefore, LIDAR is generally limited by cost and capacity for large target areas. Further reviews of LiDAR can be found in *Asal 2003*; *Fowler 2001*; *Flood 2001*; *Baltavias 1999*; and *Wehr and Lohr 1999*.

3.3.4 Digital Photogrammetry

Photogrammetry utilizes a passive sensor which detects the reflected solar radiation from ground surface and records the returns digitally or on analogue film. Classical aerial photographs for topographic mapping purposes are taken with a camera specifically designed for photogrammetry called a metric camera. These are normally of 152.4 mm focal length and large (22.5cm x 22.5cm) format, very closely representing perspective geometry. Perspective geometry is fundamental to many

photogrammetric processes and a stereo-pair of photographs (images in digital photogrammetry) are used to generate 3D coordinates *ASPRS 2004*. The steps for generating a DEM using digital photogrammetric techniques are well documented in modern photogrammetry textbooks, for example *ASPRS 2004*; *Mikhail et al. 2001*; *Wolf and Dewitt 2000* and *Schenk 1999*. They are summarised as follows: acquisition and pre-processing of aerial photos; interior orientation; exterior orientation – involving aerial triangulation or relative and absolute orientations; automatic and semi-automatic DEM generation; and DEM editing. Considerable manual labour is required for the production of high-quality optically based DEMs. Furthermore, the operational time frame for image acquisition is limited due to the natural limitations of the passive sensor.

3.3.5 Synthetic Aperture Radar (SAR)

The fundamentals of SAR have been detailed in chapter 2, where it has been highlighted that by using an active microwave system it is possible to generate images of the earth's surface regardless of illumination or weather conditions, factors which severely limit the capabilities of LiDAR and optical imaging systems especially in cloud affected territories. SAR systems can therefore play a complementary role in the generation of surface models, especially at the national and global levels, in a cost effective manner.

Four methods have been identified in the literature (*Toutin and Gray 2000*) for extracting topographic information from SAR imagery, these are: Clinometric SAR (ClinSAR), Polarimetric SAR (PolSAR), Interferometric SAR (InSAR, sometimes termed IfSAR or ISAR) and Stereoscopic SAR (StereoSAR or Radargrammetry). ClinSAR or shape-from-shading, which may be an economical method since it only requires one image of the terrain, uses the radiometric information, particularly shading, to reconstruct the topography. However, despite developments and some results during the 1990s (see for example *Frankot and Chellappa 1990*; *Guindon 1990*; and *Thomas et al. 1991*) ClinSAR remains a marginal technique, generating limited interest in the scientific community due to its inefficiency in non-homogeneous regions. PolSAR also uses a single SAR image but relies mainly on

the polarimetric configuration of the SAR backscatter. Until now, with the launching of Envisat, there have been limited sensors capable of transmitting and receiving in dual- or quad-polarization modes. Derived estimates of topography using PolSAR have been demonstrated by *Schuler et al. 1996* and *Schuler et al. 1998*. The technique is currently in its experimental phase only capable of generating profiles in the azimuth direction which must use a DSM to seed the starting elevation point for each azimuth profile. For further reviews on ClinSAR and PolSAR the reader is directed to *Toutin and Gray 2000* . The two most common techniques identified in the literature for extracting topographic information from SAR imagery remain StereoSAR and InSAR.

3.3.5.1 Interferometric SAR (InSAR)

The extraction of topographic information using the InSAR technique was first demonstrated by *Graham 1974*, but it was not until the 1980's that the first practical experiments were conducted by *Zebker and Goldstein 1986* from airborne radar systems and the concepts subsequently extended to spaceborne platforms by *Goldstein et al. 1988* for the SEASAT satellite and *Gabriel and Goldstein 1998* for the Space Shuttle Imaging Radar. Further experiments were conducted by *Li and Goldstein 1990* to examine the influence of baseline length on the InSAR results. The launch of ERS-1 and subsequently ERS-2 provided increased opportunities for researchers to conduct InSAR experiments from spaceborne sensors using tandem missions from ERS-1 / ERS-2, which provided data one day apart as opposed to the 35 day delay incurred if using ERS-1 or ERS-2 as independent datasets.

InSAR coherently combines microwave signals collected from two across-track displaced antennas. The two antennas can be mounted on a single platform (single-pass) or be a single antenna passing over the area twice (repeat-pass). The platform can be aircraft (airborne) or satellite (spaceborne). Single-pass airborne InSAR implementation can provide for the creation of surface models of greater quality because of its practical advantages compared with other implementations: no temporal decorrelation; flexible system deployment; higher spatial resolution and

lesser degree of atmospheric influence. However, there is a cost associated with these advantages whether it relates to owning the system or hiring its services.

InSAR relies on the coherence between two images of the same area taken from slightly different positions. Since the use of ERS-1 SAR for interferometry necessarily requires images taken at different times (35 days apart), so called repeat-pass interferometry, the possible changes occurring in the target area as a function of time may reduce the coherence. This change is caused either by direct changes in the surface, or because of moving scatterers. Forested areas may lose the coherence because of strong wind or seasonal changes in the canopy. These factors make the use of repeat-pass InSAR quite limited over most vegetated territories, for example the Caribbean. In this study an attempt was made to generate InSAR DSM over one of the Caribbean Islands using ERS-1 and ERS-2 archived Tandem data observed on the 23rd and 24th December 1998. This dataset was processed using the *Atlantis EV-InSAR v2.1* software. The coherence map and interferogram generated by the software are shown in Figure 3.5.

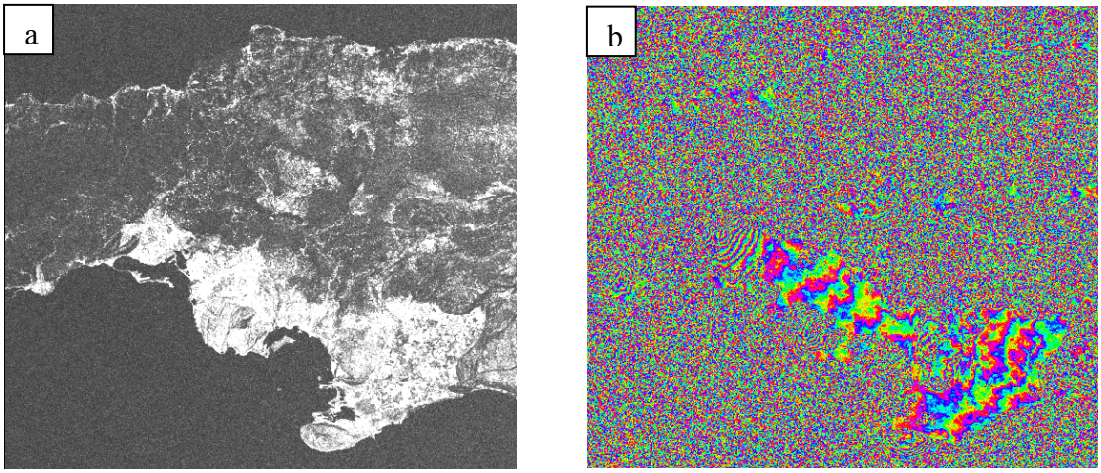

Figure 3.5: *(a) Coherence map and (b) interferogram generated over a portion of Jamaica using the EV-InSAR software. In (a) white represents areas of high coherence and black represents areas with no coherence, mainly heavily vegetated sites and the sea. The fringes in the interferogram are from 0 - 2π.*

The coherence (0 to1) is a measure of the similarity between the two images and for InSAR DSM generation it is important that no change or movement occur between the acquisitions. With spaceborne systems this will pose a problem since the acquisition has to occur in *repeat-pass* configuration as opposed to *single-pass* as with airborne systems thus resulting in extremely low coherence, or zero coherence, most of the time over vegetated areas. It is widely known that single-pass interferometry is more successful in generating DSMs because the coherence in the images is extremely high, as mentioned earlier. There has been success with the single-pass InSAR Shuttle Radar Topographic Mission (SRTM) although such near global topographical coverage datasets are known to contain data voids over some areas. Further information on SRTM can be found in *Farr and Kobrick 2000*.

3.3.5.2 Stereoscopic SAR (StereoSAR)

Unlike InSAR, which exploits the recorded phase of the signal to determine elevation, StereoSAR utilizes the recorded amplitudes (DN values) from the SAR image pair. StereoSAR is quite similar to the operations that photogrammetry uses with optical imagery and image matching techniques to extract topographic information in the overlapping portion of the digital images. The difference with StereoSAR is that it relies on Radar imagery instead of optical imagery.

The lack of suitable stereoscopic pairs of SAR imagery had led to a decline in the interest in StereoSAR and when ERS-1 was launched, scientists became more engrossed with InSAR techniques because of the apparent capability to generate elevation data over large areas. However difficulties of phase unwrapping over steep terrain and forested areas made it difficult to use the repeat pass InSAR technique for all landscape types making it more suitable for flat, low-lying areas with short vegetation, especially in arid regions.

This inability of spaceborne InSAR to generate topographic information over steep vegetated terrain along with the increase in the availability of stereoscopic SAR imagery with the launch of Radarsat in 1995, has led to renewed interest in the use of the StereoSAR technique for the extraction of topographic information.

As yet, there are no planned launches of satellite SAR systems capable of single-pass interferometry which suggests that spaceborne InSAR cannot replace StereoSAR techniques anytime soon, especially in areas with dense vegetation; which is characteristic of the Caribbean islands. It appears that a synergistic approach between InSAR and StereoSAR may be a possible solution for Caribbean countries. In this study therefore, the focus would be on assessing the ability of StereoSAR to provide topographic information over such cloud affected and densely vegetated areas. In the next few sections the StereoSAR technique is presented in more detail since it is the focus of this research.

3.4 An Overview of the StereoSAR Technique

Stereoscopic SAR (StereoSAR), in the past referred to as *Radargrammetry*, is the science and technology involved with the extraction of topographic information from stereoscopic pairs of Radar imagery. The concept of stereoscopy is not a new one and has been in use for sometime now. Stereoscopic methods were first applied to Radar images in the 1960s when *La Prade 1963* showed that some specific SAR stereoscopic pairs could produce the same elevation parallaxes as with aerial photographs; this gave birth to what was know then as *Radargrammetry*. The difficulty in obtaining proper stereoscopic pairs at this time led to mainly theoretical studies, for example *Rosenfield 1968* and *Leberl 1979*. Although there were attempts to use Radar images from SIR-B (see *Leberl et al. 1986* and *Ramapriyan et al. 1986*), ERS-1 Roll-Tilt Mode (e.g. *Twu 1996*; *Twu and Dowman 1996*) and opposite-side Radar pairs (*Fullerton et al. 1986; Toutin 1996*), it was not until the launch of Radarsat-1 in 1995 that good quality stereoscopic Radar imagery became widely available, leading to a renewed interest in Radargrammetric applications. The recent launch of Envisat and the future launch of Radarsat-2 and other stereo-capable satellites (see section 2.9.3) opens up a whole range of possibilities for stereoscopic Radar applications. A more detailed review of Radargrammetry (from this point forward referred to as StereoSAR) can be found in *Leberl 1990* and more recently by *Leberl 1998*.

3.4.1 Basic Operating Principles

The basis of StereoSAR is in the observation of the same object, on the surface of the earth, viewed from two slightly displaced positions in space and using that information to compute the full three dimensional (3D) location of that object on an appropriate map projection. Figure 3.6 shows this principle where: A_1 and A_2 are the displaced positions of the sensor with respective slant ranges R_1 and R_2; B is the stereo baseline between the satellite positions; H the altitude of the sensor and h the elevation of the terrain object P; and $\Delta\theta$ is the intersection (parallax) angle. For optimal stereo viewing Δθ should be as large as possible (*Toutin and Gray 2000*) . The principles of StereoSAR are quite similar to the techniques used in photogrammetry, where using stereoscopy, the parallax of point P is determined and this converted to the height, h.

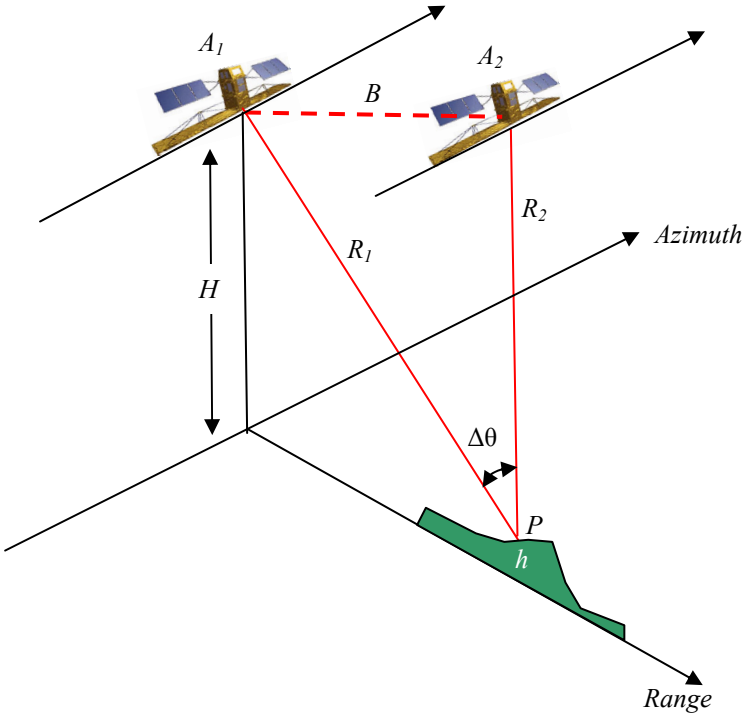

Figure 3.6: *Basic StereoSAR Principle*

3.4.2 StereoSAR Configurations

Several viewing configurations are possible when using the StereoSAR technique. The most common ones are parallel same side or opposite side orbits using steep or shallow look angles and are illustrated in Figure 3.7. A same side configuration is comprised of a stereo-pair made up of two ascending or two descending images, while the opposite side configuration consists of one ascending image and one descending image. The opposite side configuration provides parallax angles, which leads to a better geometry and therefore more accurate topographic information (*Toutin and Gray 2000*). Unfortunately, opposite side pairs are so dissimilar that it is impossible to automatically extract topographic information. It is therefore quite common to use a same-side ascending or descending pair, as a compromise between large parallax angles and accurate topographic information, when utilizing the StereoSAR technique with spaceborne SAR imagery.

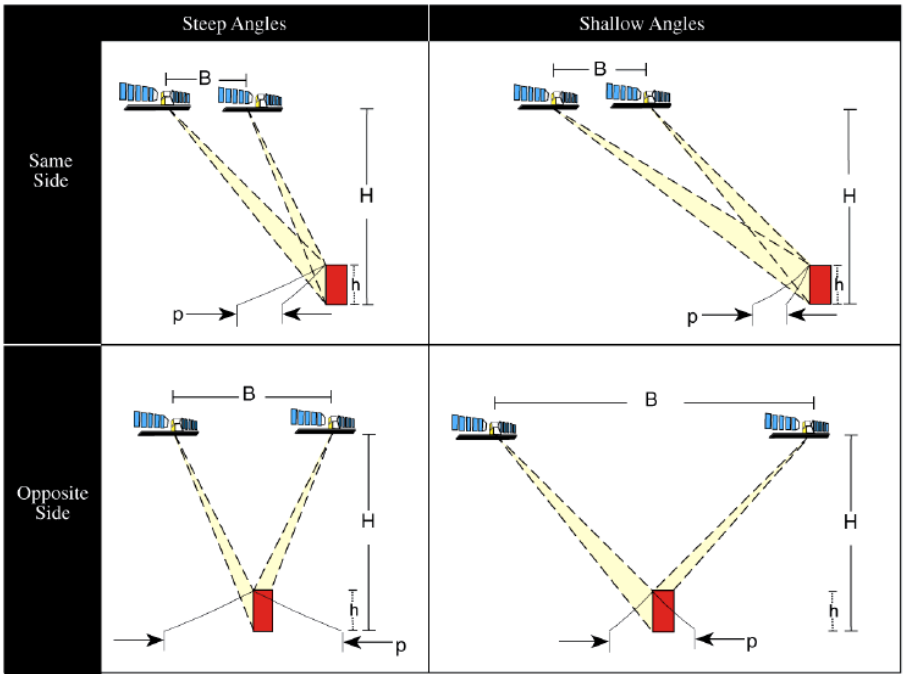

Figure 3.7: *Common StereoSAR Viewing Configurations (after Toutin and Gray 2000)*

A method of determining the minimum height that may be resolved when using different StereoSAR configurations was put forward by *Sowter 1998*, using some trigonometric relations that were based in part on Figure 3.8. Adding to this concept

it has been shown that it was possible to relate the spatial resolution of the SAR image pair and the difference in look angle between them, to the accuracy of heighting that may be achieved using that particular viewing configuration.

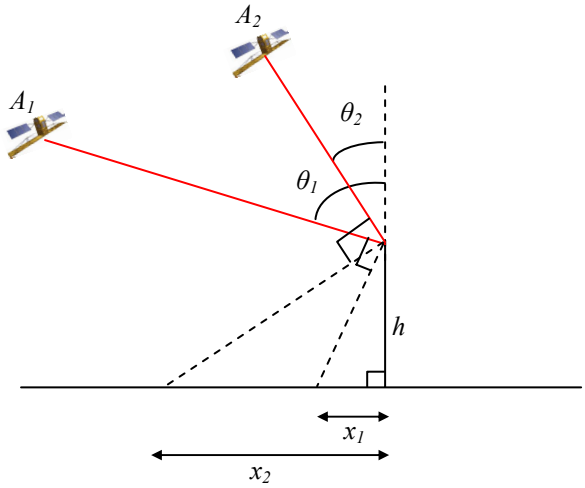

Figure 3.8: *Same Side StereoSAR Viewing Configurations*

The displacements x_1 and x_2, as shown in Figure 3.8, of a terrain point from its true position viewed from satellite positions A_1 and A_2 respectively, caused by the foreshortening effect of Radar, is given by Equation 3.1 and Equation 3.2.

$$x_1 = h \times \cot\theta_1 \qquad [3.1]$$

$$x_2 = h \times \cot\theta_2 \qquad [3.2]$$

According to *Sowter 1998* , if topographic information from two displaced viewing positions is required, as is the case with StereoSAR, then the main criterion is that the difference in displacements (parallax) caused by the viewing positions must be measurable, as indicated by Equation 3.3, where r is the spatial resolution of the SAR image pair.

$$|x_2 - x_1| \geq r \qquad [3.3]$$

The minimum height difference that may be measured using the StereoSAR technique for a particular incidence angle and spatial resolution can be found by substituting Equation 3.1 and Equation 3.2 into Equation 3.3, which would result in that shown in Equation 3.4 for a same-side configuration.

$$h_{\min} = \frac{r}{\cot\theta_2 - \cot\theta_1} \qquad [3.4]$$

Although trying to achieve the largest intersection angle, $\Delta\theta$, and consequently a large *B/H* ratio may lead to more accurate heights, it also tend to increase the chances for geometric effects such as layover and foreshortening as mentioned in section 2.7 leading to strong dissimilarities between the images. This creates problems for automatically matching the stereo-pair and can lead to poor results. In selecting stereoscopic image pairs, a trade-off will often have to be made between viewing configuration and vertical accuracy in arriving at an optimized configuration suitable for the extraction of topographic information. Table 3.1 shows the calculation of h_{min} values for a sample of image modes for both Radarsat and Envisat satellites based on the characteristics summarized in Table 2.3 and Table 2.4 respectively, for same-side StereoSAR configurations.

Table 3.1: *Minimum Height that can be resolved Using StereoSAR*

Sensor	Stereo-Pair	Angular Range (deg)	h_{min} (m)
Radarsat	S1 – S7	23 -47	9
	S2 – S7	27 - 47	12
	W2 – S7	35 - 47	25
Envisat	IS2 – IS7	23 - 44	9
	IS3 – IS7	29 - 44	16
	IS4 – IS7	34 - 44	28
	IS4 – IS6	34 - 41	38

3.4.3 StereoSAR Processing System Design

The extraction of topographic information over cloud affected and densely vegetated territories would require a system that is capable of ingesting stereoscopic pairs of Radar images, performing preliminary data processing, determination of parallaxes, conversion of these parallaxes to height and displaying the results in an appropriate map projection. The procedure for extracting topographic information using the StereoSAR technique is best illustrated using the flow diagram shown in Figure 3.9.

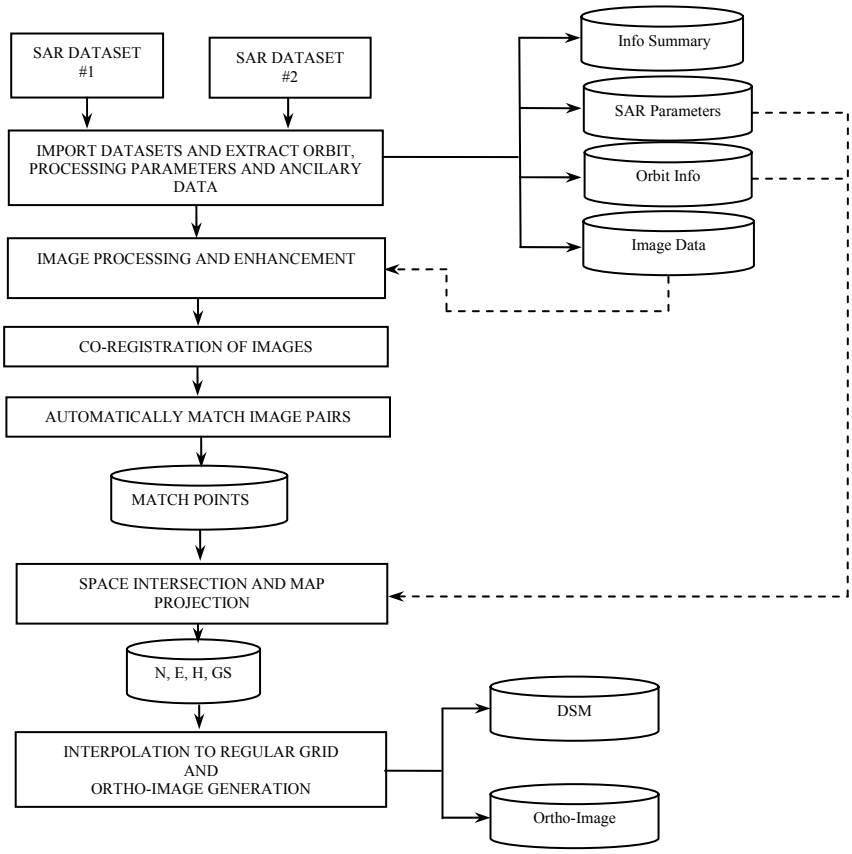

Figure 3.9: *StereoSAR Processing System Used for DSM Generation*

The critical areas in the process flow are the automatic image matching and space intersection stages, which are the main focus of this research project and these will be discussed in greater detail later in this thesis (see Chapter 4 and Chapter 5 respectively). Figure 3.9 will also form the basis for the design and implementation of the Nottingham StereoSAR system which has been developed as part of this research (see chapter 6). The following sections will briefly introduce the components of the system.

3.4.3.1 Data Input

The StereoSAR system developed, utilizes stereoscopic images obtained from both the Radarsat and Envisat sensors. The objective here is for the system to be able to read the data format and extract the image subset along with the required processing parameters. For Radarsat, the data is usually provided on CD ROM using a Committee for Earth Observation Satellite (CEOS) format which is fully described in *RSI 1997* and *RSI 2000*. A CEOS product comprises five files containing detailed information about the Radarsat image and the processing parameters used to create it. These files are as follows: Volume Directory; SAR Leader; SAR Data; SAR Trailer; and Null Volume Directory files. See *RSI 2000* for detailed information on the contents and structure of these files.

The Envisat data is also presented on CD ROM but in a different format to the CEOS structure used for Radarsat data. Only one file is distributed containing both the image and the required processing parameters. Detailed information on the format and file structure can be found in *ESA 2002*. Regardless of the format used, the StereoSAR system should be capable of extracting the following required parameters and imagery from the SAR dataset:

- Ellipsoid semi-major and semi-minor axes (*m*)
- Number of lines (rows) and pixels per line (columns) for the image (*pixels*)
- Pixel spacing (*m*)
- Azimuth time of first image line (*seconds of day*)
- Azimuth time of mid image line (*seconds*)
- Azimuth time of last image line (*seconds of day*)
- Azimuth time interval per image line (*decimal seconds*)
- Geodetic latitude and longitude of image centre (*decimal degrees*)
- State vectors (position and velocities) defining satellite orbit (*m and* m/s^2)
- Time interval between state vectors (*seconds*)
- Azimuth time of each state vector (*seconds of day*)
- Polynomial coefficients for ground-range to slant -range conversion
- Full SAR image or user defined subset of the image (*pixels*)

3.4.3.2 Pre-Processing and Enhancement

Once the images for the region of interest have been extracted it may be necessary to carry out some image pre-processing and enhancement to ensure that the tonal variations are accentuated enough to allow the identification of conjugate points during the image matching stage. This may be achieved by first removing the speckle noise that is common with SAR imagery using an appropriate speckle filter selected from those described in section 2.8.3. Next, radiometric enhancement is performed to increase the contrast between targets, using any of the standard methods in the literature such as standard deviation stretch or linear contrast stretch (see for example *Mather 2001* and *Lillesand et al. 2004*). Finally, the reference image is segmented into areas of high texture and low texture to generate a *texture mask* using a first order texture statistics based on *Ulaby et al. 1986a*. This texture mask is used in the matching algorithm, developed in this research, to adapt the key parameters of the matcher based on the existence of texture, or lack of, at a matching location. Further information on the pre-processing and enhancement algorithms used in this research, along with illustrations, can be found in section 6.2.2.

3.4.3.3 Co-Registration

In this step, the relative orientation of the reference image with respect to the search image is determined. Knowledge of this relationship is quite important because it assists in predicting the starting location of the search window in the search image during the image matching process. Very high contrast points between both images are matched and a polynomial fitted to these points using least squares. This polynomial is then used to predict the location in the search image of any point selected in the reference image. To minimize the effects of steep terrain, a hierarchical approach using image pyramids is implemented. Full description of the algorithm is given in section 6.2.3.

3.4.3.4 Stereo-Matching Image Pairs

In order to generate topographic information from stereoscopic SAR imagery, a dense array of conjugate points must be identified in the overlapping region of image

pairs using an appropriate stereo matching approach. This is one of the most critical steps in the processing chain since any errors generated here will have a significant effect on the quality of the DSM at the end. Given the importance of this step, chapter 4 has been dedicated to the treatment of this topic by providing a review of the stereo matching techniques that are available for use on SAR imagery and a detailed description of the stereo matching strategy developed as part of this research project.

3.4.3.5 Space Intersection

After the completion of the stereo matching in the previous step, all that exists is a list of image coordinates (row, column) for each of the matched pair of conjugate points determined in each image. At this stage, these do not represent any form of topographic information and would have to be some how transformed into a form recognizable by practitioners. Before this transformation process can occur, an appropriate modelling of the geometry of the SAR sensor must be accomplished. Once this SAR sensor model has been developed then it is just a matter of applying the model with ancillary data from the image header to determine the object space coordinates of the conjugate points in the list. This is also a critical step in the processing as any error generated at this stage will also affect the quality of the end product, the DSM. Chapter 5 presents detailed information on the mathematics and theory necessary for an understanding of space intersection and describes the SAR sensor model and space intersection algorithm developed in this research.

3.4.3.6 Surface Model Extraction

The space intersection process will generate mass points (also called a point cloud) based on the list of conjugate points. This point cloud, consisting of Easting, Northing, Elevation and Grey Scale value (E, N, H and GS), is not usually in a regularly spaced format. The objective of this processing step is to resample the point cloud into a regularly spaced grid that could be easily utilized in any GIS or image ortho-rectification application. In this research it was accomplished using the following steps:

1. Select the spacing (posting) for the grid (size)
2. Read all matched points into memory arrays for E, N, H and GS
3. Determine minimum and maximum E and N (minE, minN, maxE and maxN)
4. Determine map coordinates of upper left corner of grid (ULE, ULN)
5. Setup an empty grid using ULE, ULN, minE, minN, maxE, maxN and size
6. For each point in the memory array, determine its location in the grid and assign the elevation (H) to the empty grid
7. If more than one point is assigned to the same grid cell, keep a running total and determine average at the end
8. Filter the grid using majority and median filters of an appropriate kernel size to fill small holes and remove spikes
9. Display grid DSM

3.4.3.7 Ortho-Image Generation

The geometry of the SAR sensors carried on board spaceborne platforms tend to produce images that exhibit significantly greater radiometric and geometric sensitivity to local topographic relief than other optical imaging satellites such as SPOT5, Ikonos, QuickBird, etc. Before these SAR images can be used for making spatial measurements, conducting multi-temporal change detection or integrating with other datasets in a GIS environment, it is necessary to remove these geometric distortions. The process of removing geometric distortion from SAR imagery is called *geocoding* (*Bamler and Schattler 1993*), while for all other forms of imagery it is referred to as orthorectification. The main objective of geocoding, therefore, is to generate a 'map-like' representation of the SAR image – ideally an *Ortho-Image*.

There are basically two methods of accomplishing geocoding, either using a polynomial approach or by utilizing a parametric approach. The polynomial method requires a large number of ground control points (GCPs) to be identified in the SAR image that will allow the determination of polynomial coefficients to establish a

suitable mapping function for relating the SAR image coordinates to the object space coordinates, or rather the selected local or global map projection system. Depending on the incidence angle used for the image beam mode or the nature of the landscape it is often not possible to obtain a large number of GCPs in SAR imagery and this may affect the outcome of the geocoding process since it depends greatly on the distribution and quality of GCPs. A general review of the polynomial method can be found in *Naraghi et al. 1983*. A useful technique for the automatic extraction of GCPs from SAR imagery was proposed by *Chen 2000*. His technique was based on the simulation of SAR datasets by using a DEM. This implies that a DEM must be available, or first extracted from the image, before his technique can be implemented.

The parametric approach uses knowledge of the sensor geometry to effect the corrections. Three equations are used, the range and Doppler equations – analogous to the colinearity equations in photogrammetry, and an earth model described by an ellipsoid (see *Curlander 1982*, *Curlander 1984*, *Curlander et al. 1987* and *Kwok et al. 1990*). A digital model describing the topography of the earth's surface is also required. One of the applications of StereoSAR is the provision of the DSM used in geocoding. The procedure is accomplished by executing the following steps:

- An empty array covering the area of interest is created to hold the image grey values
- For each pixel in the array, the height is extracted from the DSM based on its (E, N) coordinates
- The E, N and H are projected into image space using the appropriate map projection definition and the three equations mentioned above via an iterative process.
- The grey value at this location in the image is assigned to the empty array.

This geocoding process is tremendously time consuming since it requires assessment of every pixel in the image and is not appropriate for an efficient system such as the one being developed in this research. Some authors have sought to overcome this by only computing the object to image projection at a few locations and then using a polynomial to fit to these locations. *Kim 2003* described a rectification procedure that

relies on a polynomial model derived from the imaging geometry without loss of accuracy. By using the polynomial model, he effectively eliminated the iterative process to find an image pixel corresponding to each output grid point. With the imaging geometry and ephemeris data, a geo-location polynomial can be constructed from grid points that are produced by solving three equations simultaneously. In order to correct the local distortions induced by the geometry and terrain height, a distortion model has been incorporated in the procedure, which is a function of incidence angle and height at each pixel position. With this function, it is straightforward to calculate the pixel displacement due to distortions and then pixels are assigned to the output grid by re-sampling the displaced pixels. Most of the necessary information for the construction of polynomial model is available in the leader file and some can be derived from others. Although algorithms like the one described by *Kim 2003* may speed up the process, it was still necessary to first generate DSM from the SAR images and then geocode the image in another independent process.

In this research a totally different approach, that has never been published, was adopted. This approach is extremely fast and geocodes the image whilst simultaneously generating the DSM. Since the main objective of the geocoding, as illustrated in the algorithms in the literature, is to replace the grid value on a map grid with the appropriate grey value from the SAR image, it would seem to make sense to extract this grey value during the image matching process. So instead of recording only the row, column values of the conjugate points, the grey value at the matched location in the reference image can also be recorded. During the resampling process to generate the DSM a duplicate grid is created and instead of assigning elevation values (as in step 6 in section 3.4.3.6) the grey scale (GS) values are assigned. This is demonstrated further in chapter 6.

3.5 Quality Assessment of Surface Models

Understanding the quality of the DEM datasets is crucial to their use in many studies and also in the detection of change obtained from the comparison of DEMs acquired at different temporal resolutions. *Wise 1998* and *Cooper 1998* noted that the quality

of DEM data is too often overlooked, and this can have serious implications for many applications. *Lane et al. 2004* have put forward a few reasons as to the importance of having some understanding of the quality of DEMs. First, there has been increased growth in the availability of digital data sources, some of which have unknown or poorly specified data quality. Secondly, digital data derived from numerous processes tend to have errors propagated at each stage of the process leading to magnified errors in DEM-derived parameters. Thirdly, new methods of data generation have led to increased automation for the production of DEMs which ultimately have led to a significant increase in the data whose quality is to be determined with a substantial reduction in manual quality control. Lastly, the volume of data generated automatically is extremely large in comparison to the available check data. The ability to assess errors in the dataset is therefore reduced to the point of becoming unreliable.

It is a fundamental principle of surveying that a measurement is not useful if it does not have a quality measure and this is supported by *Caspary and Joos 2002*; unless the quality of a DEM is well known, the dataset should not be used for any application. Information on DEM quality is of great importance since it affects for example, the reliability of any modelling exercise and can impact on the credibility of any decisions made from those results. What therefore do we mean by quality as it refers to spatial data? Quality may mean different things to different users depending on their respective needs or applications. *Veregin 1999* surmises that quality refers to the difference between the actual characteristics of the dataset and the relevant specifications that define it or the claims made about it. For the purposes of this report we will refer to the quality of a DEM as its fitness for a particular application (i.e. “fitness-for-purpose”).

How then do we determine the quality of a DEM? *Veregin 1999* identified several components of quality which included: accuracy, precision, spatial resolution, consistency and completeness. In surveying and mapping it is common to associate the quality of a DEM with the level of errors that the dataset contains. There is no such thing as an error-free DEM. Following traditional error analysis in surveying, *Cooper and Cross 1988* identified three categories of such errors: systematic errors,

random errors and gross errors (or blunders) which are thought to have a direct influence on data accuracy, precision and reliability, respectively. Systematic errors have a fixed pattern and are usually related to the sensor or the observing procedures used for the data collection. Such errors may not be easily detectable and if not eliminated can introduce significant bias or artefacts into the DEM being generated. If these errors can be identified, they can then be modelled, reduced or even eliminated (*Daniel and Tennant 2001*). System calibration and mathematical modelling are often used to aid the minimization of systematic errors. Random errors are due to the variations in the sensors or the environment and the observing procedures in use. They are therefore due mainly to inconsistencies in the measurement process and cannot be removed, even after eliminating systematic errors. They are usually dealt with through the use of statistics and rigorous adjustments such as least-squares (*Mikhail 1976*). Blunders or mistakes are often caused by human error and will affect the reliability of the DEM. The occurrence of these can normally be minimized by the use of good measurement/survey practices.

In assessing the quality of a DEM it is common practice (see for example: *Shearer 1990*; *Lane et al. 2004* and *Edwards et al. 2005*) to compare height values of random points derived from the DEM with height values of co-located points obtained by using a more accurate instrument/method than that used to derive the DEM being assessed. As an example, a DEM generated from LiDAR can be assessed using points observed with GPS or a total station survey. The difference between the DEM points and the GPS points will give residuals, which could be positive or negative, at these locations. By conducting statistical analysis on the residuals, one can arrive at estimates of the quality of the DEM under consideration. The statistical measures normally used are: Mean Error; Standard Deviation and the Root Mean Square Error. It is important to note that these are 'global' statistical measures and only represent the error at the sample locations and may not be representative of the quality of the entire DEM, which may have systematic error trends due to the interaction of the sensor with different types of landscape features.

- ***Mean Error (ME)***

  This statistical measure determines the extent to which the DEM is free from systematic errors or bias. The sign of the residuals are taken into account and will tend to zero if there are similar magnitudes of positive and negative values i.e. there is no systematic error. If a significant positive or negative value was determined then this would indicate the evidence of systematic error i.e. one surface is systematically higher or lower than the other. The Mean is computed as follows:

$$\bar{\Delta H} = \frac{\sum_{i=1}^{n} v_i}{n} \qquad [3.5]$$

  Where $\bar{\Delta H}$ is the mean error, ν is the difference between the DEM and a known height and *n* the number of points used.

- ***Standard Deviation (SD)***

  Standard deviation is another commonly used statistical expression based on the dispersion of random errors in the DEM. It shows how the values being considered vary with respect to the mean and gives a sense of the precision of the DEM. SD is computed as follows:

$$SD = \pm\sqrt{\frac{\sum_{i=1}^{n} (v_i - \bar{\Delta H})^2}{n}} \qquad [3.5]$$

  This statistic is also useful for detecting blunders or outliers as it relates to a probability density function where SD defines the area under the normal distribution curve and the 68% probability of any observation occurring within ±SD from the mean. It is common practice to reject as a blunder, any point that is not within ±3×SD from the mean residuals.

- ***Root Mean Square Error (RMSE)***

  The most widely used measure for reporting accuracy is the Root Mean Square Error (RMSE). Its widespread use may be due to the ease of computations and the ease with which the concept can be understood by most data users. It is a dispersion measure being approximately equivalent to the average deviation between two datasets. The RMSE is computed as follows:

$$RMSE = \pm\sqrt{\frac{\sum_{i=1}^{n} v_i^{\,2}}{n}} \qquad [3.7]$$

  The most common use of the RMSE is to provide a single global measure of deviation. Consequently, there is no indication of spatial variation over the surface of the DEM. As the name contains the word 'error' it is expected that there is no bias in the residuals.

3.6 Summary

The objectives of this chapter were to introduce the theory of surface modelling, review the techniques for accomplishing such a task and to outline the StereoSAR strategy that has been developed in this research. The stereo matching and space intersection stages have been identified as the most critical components in the StereoSAR process flow and these will be dealt with in more detail in the next two chapters. The most common methods of representing the quality of DSMs have been the use of statistical descriptors such as the mean and RMSE. These descriptors are usually global in nature and do not give a complete description of the spatial distribution of the errors.

Chapter 4

Digital Stereo Matching of SAR Imagery

4.1 Introduction

The most critical step in the extraction of elevation information from stereo pairs of synthetic aperture radar (SAR) images, acquired using spaceborne sensors, is the matching of conjugate points in the images to derive disparity (parallax) data whereby a digital surface model (DSM) can be constructed. This process of determining conjugate points in the stereo imagery is referred to as *stereo matching* (or image matching in some literature). The main difficulty in properly matching SAR imagery is the level of speckle noise (section 2.8) in the imagery and this has to be taken into account in the development of any matching strategy.

Two main methods are available for matching digital SAR images (*Toutin and Gray 2000*): a manual approach and an automated method. With the manual approach, a computer system is used to assist the operator in viewing the images stereoscopically while the corresponding points are selected individually; a process similar to that used in analytical photogrammetry. A SAR *Standard Mode* image usually has approximately 9000 rows by 9000 columns or 81,000,000 pixels each with grey values ranging from 0 to 255 for 8 bit data and 0 to 65535 for 16 bit data. Clearly, manually matching on the basis of individual pixels would be time consuming, costly and almost impossible if an economic DSM is to be produced. It would therefore seem that only a completely automatic matching strategy would be appropriate for digital SAR images; hence, this research work focuses on automated methods of stereo matching.

This chapter seeks to outline automated stereo matching theory and highlight the need for an alternative stereo-matching strategy for use with SAR imagery, which will help to overcome some of the problems experienced with existing matching techniques.

4.2 Automated Stereo-Matching Methods

Stereo-matching has been an area of much research for the past 20 years generating an enormous amount of literature. Most of this research has centred on developments for optical imagery from airborne (see *Ackerman 1984*; *Gruen 1985*; *Hannah 1989* and *Schenk 1996*) and spaceborne sensors such as SPOT (see *Otto and Chau 1989*; *Day and Muller 1989* and *Zhen 2001*); while there has been relatively little focus on the automatic matching of SAR imagery (e.g. *Twu 1996* and *Chen 2000*).

An early review of stereo matching methods is given by *Lemmens 1988* where he identified three approaches to matching imagery: *Signal Matching* – referred to today as area based matching; *Feature Matching*; and *Relational Matching*. A more recent overview of stereo matching techniques can be found in *Heipke 1996*. A brief overview of each method is given in the following sections. The result of automatic stereo matching is a *disparity file* or *disparity map*, specifying the relative displacements of match points between the image pair.

4.2.1 Area-Based Matching

Considered to be first generation stereo matching, Area-Based Matching (ABM) compares patches (areas) from both images by either minimizing the grey level differences or maximizing their correlation. The two fundamental techniques used for ABM are: Normalized Cross-Correlation (NCC) and Least Squares Matching (LSM). Other techniques such as *sum of mean normalized absolute difference* (MNAD) and *sum of mean normalized squared difference* (MNSD) have been discussed by *Leberl et al. 1994* but these are not suitable for use with SAR data because they do not take into account the radiometric difference between images which could lead to poor matches. Experiments conducted by *Leberl et al. 1994* using NCC, MNAD and MNSD identified NCC to be the most accurate.

The limitation with using patches of pixels is that they are sensitive to differences associated with the relief distortion, illumination and contrast changes; occlusion and shadows. Another limitation is that the use of similarity measures is only productive in local matching. There is no global consistency, i.e. a set of values in the reference

template may match more than one set of locations in the search image, thus producing false matches. To resolve the ambiguity, constraints must be incorporated into the matching strategy. This may involve limiting the area which is searched which will also result in reduced computational time. Techniques for limiting search space include enforcing epipolarity or the use of image pyramids to match images in a hierarchical sequence from the coarsest image to the finest image in the pyramid.

4.2.1.1 Normalized Cross-Correlation

In order to compute a match between conjugate points, two templates (one in each image) are used; a reference template in the left image and a search template in the right image (see Figure 4.1). The actual point to be correlated is the central point of the reference template. The templates are usually square and of fixed sizes (e.g. 3x3, 5x5, 7x7, 9x9, etc.). Since we do not know the exact position of the candidate point in the right image, a search area is selected with dimensions much larger than those of the search template centred on a predicted location. The reference template maintains its location for each point to be correlated in the search area, while the search template is shifted pixel by pixel across the search area and at each position the normalized correlation coefficient $\boldsymbol{\rho}$ between the reference template and search template is calculated.

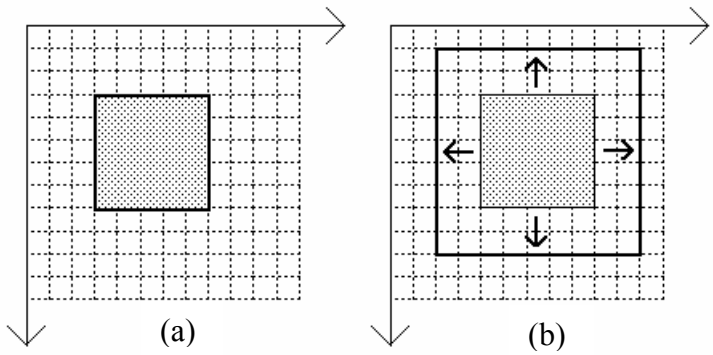

Figure 4.1: *Principle of cross correlation: (a) Reference Image and (b) Search Image (after Heipke 1996)*

The location with the largest correlation value within the search area is considered to be a match, providing it is above some predetermined threshold. When using the normalized cross-correlation, it is not necessary to balance the contrast or brightness between images before correlation and the method does not require an accurate estimate of the predicted starting location in the search image, however, the accuracy of a matched point is only good to ±1 pixel. The normalized cross-correlation coefficient is determined using (*Heipke 1996*):

$$\rho = \frac{\sum_{r=1}^{R}\sum_{c=1}^{C}(g_1(r,c)-\mu_1)(g_2(r,c)-\mu_2)}{\sqrt{\sum_{r=1}^{R}\sum_{c=1}^{C}(g_1(r,c)-\mu_1)^2\sum_{r=1}^{R}\sum_{c=1}^{C}(g_2(r,c)-\mu_2)^2}} \quad ; \quad -1 \le \rho \le 1 \qquad [4.1]$$

Where:

$g_1(r,c)$	individual grey values of template matrix
μ_1	average grey value of template matrix
$g_2(r,c)$	individual grey values of corresponding part of search matrix
μ_2	average grey value of corresponding part of search matrix
R, C	number of rows and columns of template matrix

4.2.1.2 Least Squares Matching

Unlike the normalized cross-correlation method - which maximizes a function of normalized grey value differences - the least squares matching (LSM) method involves minimizing grey value differences between conjugate points in the reference and search images. The incorporation of radiometric and geometric distortions in the adjustment results in a higher accuracy of matching than the NCC. *Lemmens 1988* and *Leica 2003* reported matching accuracies of better than 0.1 pixel. However, unlike NCC the LSM technique requires an estimate of the starting position in the search image to better than 2 pixels.

The possibility of using a least squares approach for matching stereoscopic pairs of images was first proposed in the 1980s (*Ackerman 1984*) and a modification to this approached called an *adaptive least squares correlation* technique was later presented by *Gruen 1985*. Here, the author assumes that the conjugate regions of a stereo pair can be represented by two dimensional functions $f(x,y)$ and $g(x,y)$ for the left and right image respectively. Correlation is established if $f(x,y) = g(x,y)$. This will not necessarily be the case because radiometric and geometric distortions plus noise are known to affect the images and these must be modelled; this results in:

$$f(x,y) = h_0 + h_1 * g[(a_0 + a_1x + a_2y),(b_0 + b_1x + b_2y)] \qquad [4.2]$$

With $a_0, a_1, a_2, b_0, b_1, b_2$ being the unknown parameters for an affine transformation and h_0, h_1 the unknown coefficients for the radiometric corrections. In order to apply a least squares approach, Equation 4.2 can be considered a non-linear observation equation and must be linearized, leading to:

$$\Delta g(x,y)+v(x,y) = h_1 g_x(x,y)da_0+h_1 x g_x(x,y)da_1+h_1 y g_x(x,y)da_2+h_1 g_y(x,y)db_0+ h_1 x g_y(x,y)db_1+h_1 y g_y(x,y)db_2+dh_0+g(x,y)dh_1 \qquad [4.3]$$

Where:

$v(x,y)$ = grey value difference residuals

$\Delta g(x,y) = f(x,y) - g(x,y)$ (observed grey value differences of the pixel array)

$g_x(x,y) = [g(x+1,y) - g(x-1,y)]/2$ (gradient function in the x direction)

$g_y(x,y) = [g(x,y+1) - g(x,y-1)]/2$ (gradient function in the y direction)

It is important to note that the linearized equation is implemented for related pixels in the reference and search templates. An [n x n] template in both the reference and target image will result in n^2 equations with 8 unknowns. One disadvantage of the least squares procedure is that it is very sensitive to initial approximations which could have an adverse effect on the matching. Another disadvantage with LSM is that it is very computationally intensive i.e. for a template size of 15 x 15 pixels there will be 225 equations in 8 unknowns to be solved iteratively for each window position. This is usually not an optimal solution to be used in a low-cost system for extracting elevations.

4.2.2 Feature-Based Matching (FBM)

The concept of feature matching was developed from the theories based on similar visual systems as those used by people, where it was demonstrated that the human brain can fuse individual features to reconstruct a 3D scene (*Marr and Poggio 1979*).

As the name suggests, this approach involves the matching of features that have been extracted from both images as opposed to patches of greyscale values in the case of the ABM method. According to *Schenk 1996*, these features could include points, edges or regions. Edges are by far the most popular feature adopted in the matching process, although in some photogrammetric applications feature points called *interest points* (*Forstner 1986*) are used. The speckled nature of SAR imagery makes the use of interest points problematic, unless they are good persistent scatterers that can be identified in both images.

FBM follows two stages: first, the edges are extracted from each image pair; secondly, there is the matching of the extracted edges to determine the conjugate points. Edges are usually extracted from the images using either: gradient operators such as Sobel and Prewitt (see *Pitas 2000*); or the zero-crossing of the second derivative proposed by *Marr and Hildreth 1980*. The best way of finding the second derivative of an image is to convolve it with the operator:

0	-1	0
-1	4	-1
0	-1	0

[4.4]

Dare 1999 used an FBM approach for the registration of SAR and SPOT images. Edges were extracted from both images using a Sobel operator and matched using dynamic programming.

FBM has not been very popular with stereo matching SAR images. According to *Toutin and Gray 2000*, edges tend to differ a lot in one image than the other especially in mountainous terrain. If features are well defined though, FBM can produce good results. However, because features tend to be sparse in the imagery there tend to be a low number of conjugate points which may not be dense enough to generate a DSM grid. If a feature-based method is used, an extra processing step is required for feature detection in the stereo pair, which will increase the computational time required for generating disparity maps.

4.2.3 Relational Matching

According to *Heipke 1996*, features in an image may be either characterized as local or global. Local features such as points, line and edges were mentioned earlier in section 4.2.2. Global features include polygons and other complex structures which are usually composed of many related local features. The matching of global features and their internal relationship is termed *relational matching* or *structural matching*. In this technique the corresponding image structure can be identified automatically without any a-priori information. However, the process is incredibly time consuming.

4.2.4 Hybrid Matching Techniques

The stereo matching techniques reviewed in the previous sections should not be seen as competitors but rather as complementary methods. Their possible combination can lead to benefits as opposed to applying each matching technique individually. Since FBM techniques do not require approximate starting values, it can be used to generate approximate values to seed the ABM matching process; thus, hybrid approaches between FBM and ABM may achieve better and faster solutions for the matching problem, in theory. If the algorithm will have to execute a lot of processing to extract features and prepare them for matching (e.g. clutter removal, linking edges, etc.), then such an approach may not be appropriate for implementation in a fast, low-cost DSM generation system.

4.3 The Challenges of Matching SAR Imagery

Despite considerable progress, the problem of extracting elevation data from SAR images to form a realistic representation of that portion of the earth's surface under consideration is still not completely solved. *Ostrowski and Cheng 2000* conceded that although DSM from SAR is a well established technique, it is still proving to be a challenge because of the characteristics of the imagery. The main difficulty they reported was in obtaining a large number of accurate stereo matches (conjugate points) while at the same time reducing the amount of false matches, blunders and artefacts in the derived DSM. Essentially, the problem is one of correctly stereo matching the pair of SAR images.

The factors proving to be a challenge for correctly matching pairs of SAR images can be summarized as follows (*Leberl 1990*; *Ostrowski and Cheng 2000*):

1. Distortion due to terrain (both geometric and radiometric)
    a. Geometric - slopes facing the sensor are usually affected by foreshortening or layover, while slopes facing away from the sensor are stretched.

    b. Radiometric - due to the direct reflection of the antenna signal, slopes facing away from the sensor are darkened or shadowed.

2. Speckle noise - helps to reduce the similarity between images. This noise is the main source of problems for stereo matching SAR images (see section 2.8)

3. Large featureless areas, especially in flat and homogeneous regions. This causes the matching to fail or produce sparse false matches of speckle pattern.

4. Illumination direction. Repeat pass SAR stereo pairs can be obtained from a same-side or opposite-side configuration. Because the illumination direction is different for opposite-side images, the dissimilarity is greatest for this image pair, making automatic matching almost impossible.

Successful matching relies on the similarities between image pairs, so dissimilarities caused by the factors above presents an obstacle. Stereo matching algorithms must be designed so that they are robust against these factors.

4.4 Previous Research on Stereo Matching SAR Imagery

Research into the automatic matching of stereoscopic pairs of spaceborne SAR imagery dates as far back as the 1980s and since this time has followed three routes which can be summarised as: area based matching using correlation; area based matching using least squares; and hybrid approaches using a combination of area-based and feature-based matching methods. Examples of these research efforts are outlined in the following paragraphs.

Ramapriyan et al. 1986 conducted automated matching for pairs of SIR-B images. The techniques applied were adapted from those originally developed for use on optical data. They used a hierarchical approach with a *sum of mean normalized absolute difference* (MNAD) for determining correlation but an accuracy assessment of the constructed surface model was not given. They however predicted that with accurate ground control absolute elevations with a standard deviation of ±120m could be obtained.

Denos 1991 and Denos 1992 presented a procedure for stereo matching Seasat and SIR-B data respectively. To handle the problem of speckle, the author implemented a coarse-to-fine pyramidal approach. She also noted that applying a speckle filter increases the coverage of matched points. The algorithm was based on that developed by *Otto and Chau 1989* for the matching of SPOT imagery. The Otto-Chau stereo matcher is based on the Gruen's adaptive least squares correlation technique and incorporates a region growing mechanism. Good initial seed points are required to start the matching process. The approach tends to leave large gaps in the generated surface where the matcher was unable to 'grow' disparity values as evidenced by the examples in *Denos 1992*. Again, no accuracy assessment was given for the derived surface model.

Twu 1996 carried out research into stereo matching ERS-1 RTM imagery and tested some of the parameters of the coarse-to-fine pyramidal approach previously outlined by *Denos 1992*. His methods of selecting the parameters were solely based on trial and error and the problem of automatically determining an optimal number of seed points still existed. *Chen 2000* sought to progress this work further using Radarsat imagery by providing answers to the following questions: how many tiers of the image pyramid are suitable? How many seed points are necessary for the correlation of SAR image pairs? What is an adequate uncertainty radius for predicting seed points? To address these issues, *Chen* developed an optimized parameter decision strategy. In the end, *Chen's* strategy still required the user to manually input a value for the maximum parallax parameter.

Aside from the least squares matching, other researchers investigated the possibility of merging area-based and feature-based methods for stereo matching SAR imagery but at the moment providing little improvement to the matching process. *Sylvander et al. 1998* attempted to improve the correlation performance by using edge detection to enhance the image structure. They used Radarsat standard mode imagery that was resampled to a *quasi-epipolar* geometry and then processed both images with a ROEWA (Ratio Of Exponentially Weighted Averages) multi-edge detector. The authors noted that the results did not indicate any improvements with or without edges in the stereo matching process.

Undoubtedly, the most common method of stereo matching used by researchers was the normalized cross-correlation with computation of the correlation coefficient using Equation 4.1 (see for example, *Simard et al. 1986*; *Toutin 2002*). *Leberl et al. 1994* performed automated image matching experiments to identify the robustness and accuracy of matching two radar images, taken by the Magellan spacecraft, using current matching algorithms. They found that the normalized cross-correlation (NCC) method achieved the best results with a deviation of ± 2 pixels when compared with a human operator. *Paillou and Gelautz 1999* instead of matching patches of greyscale values convolved the radar image with a linear gradient operator optimized for noise removal and went on to match these gradient images using the NCC method. Their preliminary results showed a 10-15% improvement in surface reconstruction which may not be significant and consistent over all landscapes.

4.5 The IESSG Adaptive Matching Algorithm (*IAMA*) Design

The automatic stereo matching of image pairs is the most difficult step in the processing chain, especially for SAR imagery. Yet, it is the most important because it dictates the quality of the topographic data being extracted. The objective of stereo matching, as mentioned earlier, is that for each pixel in a reference image the automatic matcher tries to locate its conjugate in the search image for a stereoscopic pair.

In the review of the literature from the previous section, it was revealed that researchers used NCC, LSM or hybrid techniques combining area-based and feature-based matching; the most popular at the moment being NCC which is usually implemented using a hierarchical approach based on image pyramids. A number of parameters, referred to as *strategy parameters*, are used to control the operation of the stereo matching process and these include: correlation threshold; template size; starting and stopping pyramids; and the size of the search area (x-parallax). *Gooch and Chandler 1998* conducted studies to identify a set of optimized values for strategy parameters used with the matching of aerial photographs in photogrammetry.

Previous researchers (e.g. *Sowter 1998* and *Ka and Kim 2001*), using a hierarchical area-based matching approach, maintained fixed template sizes and correlation threshold values throughout the matching process. The use of fixed values can be problematic especially in low textured or homogeneous areas. In this research, a modified approach to stereo matching was developed. The area-based normalized cross-correlation method of determining conjugate points is retained because it does not require accurate estimates for starting the matching process and for the low-cost system being developed achieving sub-pixel accuracy would be too time consuming. The idea of matching on a hierarchical level is also maintained since this helps in minimizing the search area thus speeding up the processing time of the algorithm, which is good for the low-cost system.

However, this is where the similarity with previous approaches ends. In this development, the algorithm is allowed to automatically adapt the matching template size, correlation threshold and the x-parallax strategy parameters based on the texture, or lack thereof, in the imagery. It is important for this development to use a method of masking the image into texture and non-texture (or low texture) areas that is efficient, yet simple to implement. Figure 4.2 presents the process flow for the *IESSG Adaptive Matching Algorithm* developed as part of this research.

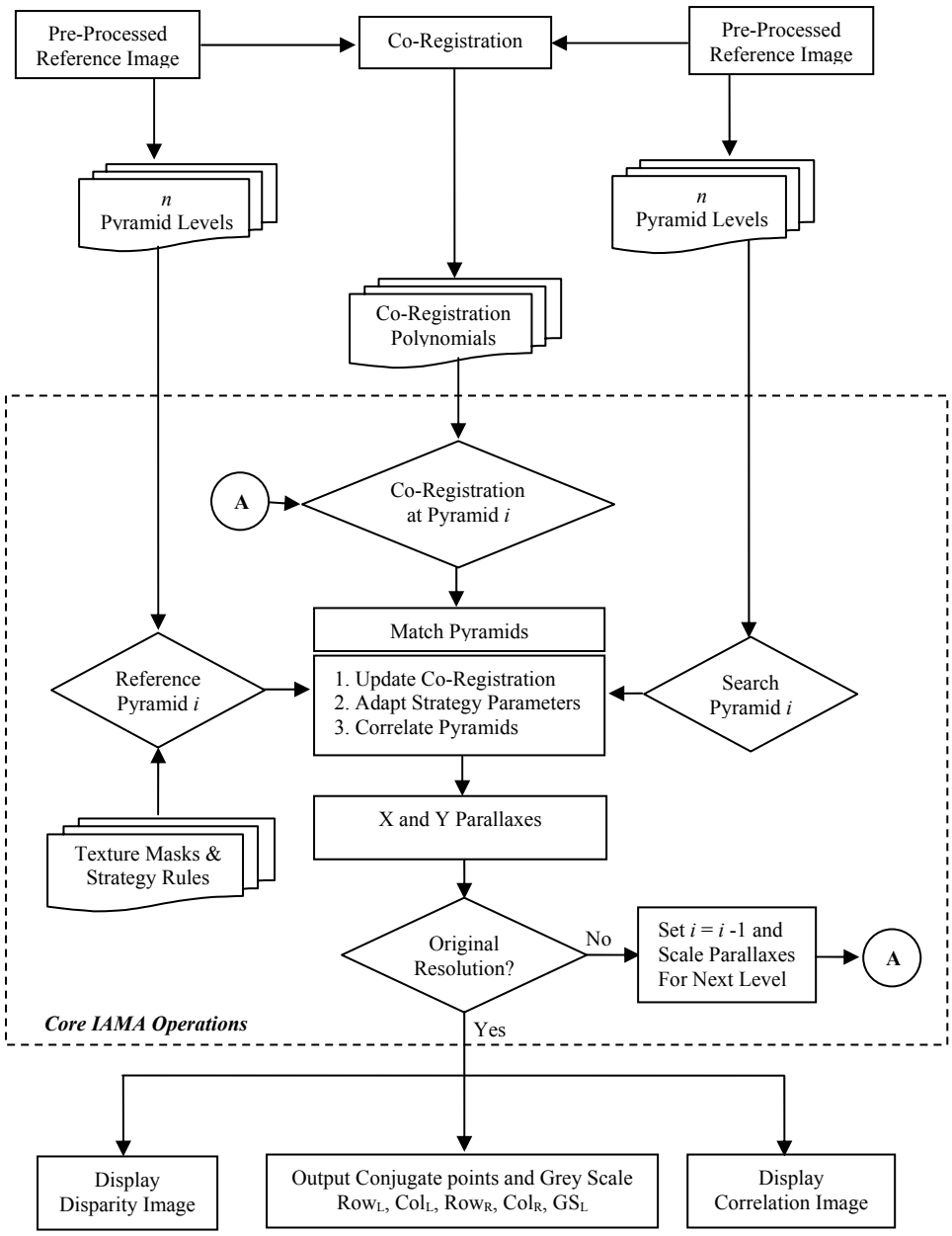

Figure 4.2: *Overview of the process Flow for the IESSG Adaptive Matching Algorithm (IAMA)*

The following sections will describe in more detail some key concepts used in the development of the *IESSG Adaptive Matching Algorithm.*

4.5.1 Texture Masks

Texture refers to the spatial variation of tonal elements as a function of scale (*Haralick et al. 1973*) and can be very useful in interpreting radar images and discriminating among different landscape types (*Ulaby et al. 1986a*). In order to describe texture it is necessary to select some measure that encapsulates the information. *Tso and Mather 2001* and *Ulaby et al. 1986a* described several approaches, with varying complexity, for the determination of textured areas in SAR images. This research opted for a method which would be simple to implement and would not increase the processing time of the system, since the intent is to develop a fast low-cost application. The choice therefore was the use of a first order statistical texture method capable of separating spatial variability attributed to intrinsic scene texture from that attributable to speckle. If speckle in the SAR image can be accounted for then the remaining texture is primarily a function of the surface characteristics. Texture mask was generated based on the following relationship outlined in *Ulaby et al. 1986a* :

$$\left(\frac{\sigma_Z}{\mu_Z}\right)^2 = \left(\frac{\sigma_T}{\mu_T}\right)^2 \times \left(\frac{\sigma_S}{\mu_S}\right)^2 + \left(\frac{\sigma_T}{\mu_T}\right)^2 + \left(\frac{\sigma_S}{\mu_S}\right)^2 \qquad [4.5]$$

where

σ_Z and μ_Z are the standard deviation and mean of a fixed sized window being moved across the image.

$\left(\frac{\sigma_Z}{\mu_Z}\right)^2$ being made up of two components - speckle and scene texture.

$\left(\frac{\sigma_T}{\mu_T}\right)^2$ is the normalized texture variance.

$\left(\frac{\sigma_S}{\mu_S}\right)^2$ is the normalized speckle variance.

Knowing σ_Z, μ_Z and the normalized speckle variance, which is usually 1/*N* for intensity images and 0.273/*N* for amplitude images (where *N* is the number of looks), an estimate of the normalized texture standard deviation can be computed by rearranging Equation 4.5 to give:

$$\left(\frac{\sigma_T}{\mu_T}\right) = \sqrt{\frac{\left(\frac{\sigma_Z}{\mu_Z}\right)^2 - \left(\frac{\sigma_S}{\mu_S}\right)^2}{1+\left(\frac{\sigma_S}{\mu_S}\right)^2}} \qquad [4.6]$$

The result is usually a decimal value less than 1 and would have to be stretched to a range 0-255 and threshold to form the required texture mask for this project. Determining an appropriate moving window size, threshold value and illustration of some examples of the texture mask are dealt with in section 7.5.2.3.

4.5.2 Image Pyramids

The term image pyramid implies the representation of an image using a structure that contains various resolution levels. It is essentially a hierarchy of digital images portraying the same location. There are two main parameters defining the structure of the image pyramid:

- The *reduction factor*, which determines the rate at which the number of pixels decrease from one pyramid level to the other (usually 2).

- The *reduction window*, which associates a set of pixels of the level directly below to every (higher level) cell. It covers the area of its associated cell.

An image at pyramid level I_{i+1} can be generated from an image at the previous level I_i by averaging the greyscale values of the *n* x *n* pixels from the previous higher resolution level. In this research n = 2.

It has been shown that a multi-resolution or hierarchical approach to stereo matching using an image pyramid can be faster than one without, as the search range in each level is reduced (*Sun 1998*). Besides fast computation, more reliable disparity data can be obtained by exploiting the pyramidal data structure since the reduction in image resolution also reduces the dissimilarities that may exist between the images in the stereo pair. *Sun 1998* noted that there are three useful properties of a hierarchical stereo matching scheme that has been implemented using image pyramids: (a) the pull in range or search range can be increased because at the coarse pyramid level only approximate starting values are required; (b) the convergence speed of the matching can be improved; and (c) reliability of finding correct matches can be increased. Figure 4.3 shows a typical image pyramid structure.

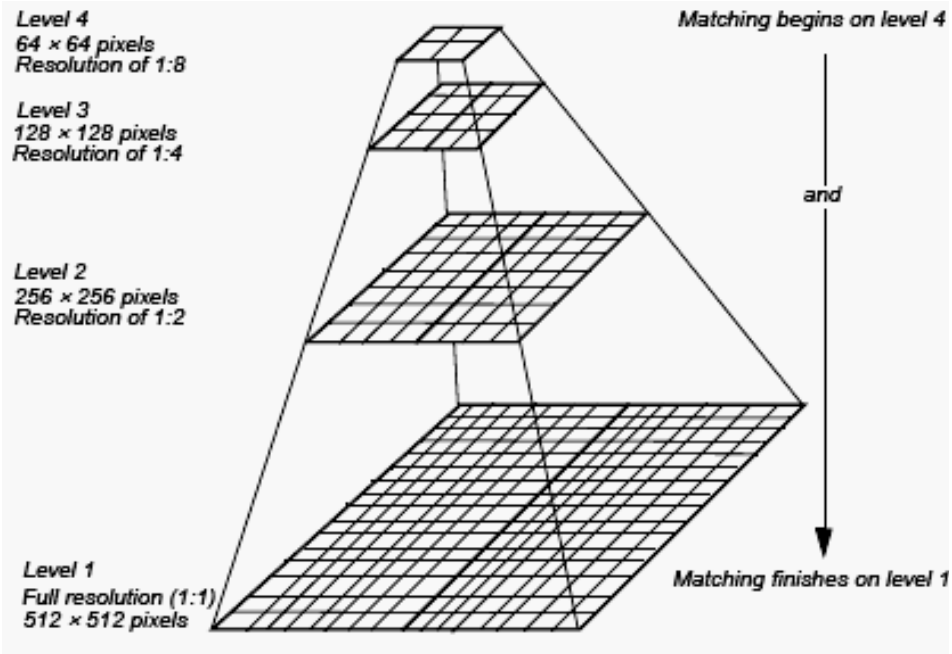

Figure 4.3: *Typical Structure for an Image Pyramid Comprising Four Levels (after Leica 2003)*

4.6 Summary

To generate topographic information from stereoscopic SAR imagery, a dense array of conjugate points must first be identified in the overlapping region of the stereo pair using an appropriate stereo matching strategy. Of the stereo matching methods available, previous research studies have shown that the normalized cross-correlation method offers the best solution for SAR imagery. Although LSM approach can give the most accurate matches this is only possible if good estimates for seed points are known, which is not usually the case; moreover, the LSM approach is quite computer intensive requiring numerous computations per pixel location.

This chapter presented an overview of the stereo matching of stereoscopic SAR imagery and outlined the *IESSG Adaptive Matching Algorithm* developed as part of this research, for integration into the StereoSAR system. The polynomials generated from the co-registration process are used as the basis for seeding the matching, which is implemented in a hierarchical approach using image pyramids. A texture mask generated from a first order texture statistic is used to adapt the strategy parameters in areas of low texture. The texture mask it not intended to guarantee a match occurring, but rather to make the algorithm aware of the low textured areas so that it can be more suspicious of matches that occur in these areas. The output from the algorithm is a disparity file containing the image coordinates of the conjugate points successfully passed from the various layers of the image pyramid. The next chapter demonstrates how the disparity file can be used to generate 3D points of the landscape as a first step to obtaining a model of the terrain surface.

Chapter 5

Space Intersection Strategies

5.1 Introduction

The generation of topographic data from spaceborne stereoscopic Synthetic Aperture Radar (StereoSAR) imagery, requires the use of a precise sensor model for relating image coordinates to object space and involves a process normally referred to as space intersection. Previous methods required the use of ground control points (GCPs) in determining the StereoSAR sensor model (see for example *Toutin 1995*; *Leberl et al. 1986*; and *Raggam and Gutjahr 1998*). The location of GCPs in SAR imagery can be very problematic especially over developing countries where there are very few regular or planned features well positioned and distributed over the image and often times not large enough to be clearly defined by the Radar resolution.

For SAR imagery there is a need for the development of a GCP-free space intersection strategy, especially over developing countries where it will not always be possible to have access to some of the steep terrain that tend to characterize some of the landscapes, especially in the Caribbean. Such GCP-free algorithms will certainly allow real 'remote sensing' applications to be developed thus providing the opportunity for the generation of information over hazardous and inaccessible areas. One factor limiting the use of GCP-free space intersection algorithms in the past was the lack of SAR systems with suitably stable and accurate orbits. *Chen 2000* and *Chen and Dowman 2001* implemented a space intersection algorithm for use with Radarsat but had to use two GCPs to remove systematic biases in the elevation contributed by the uncertainty in the satellite orbital parameters. The new Envisat satellite provides a more stable and accurate orbit and should, at least in theory, be able to facilitate the development of GCP-free space intersection strategy thereby eliminating the need for GCPs to remove systematic errors at the end. There are at present no studies or experiments that evaluate the capability of the Envisat SAR sensor for providing GCP-free space intersection.

In this chapter, an algorithm for a rigorous sensor model for use with StereoSAR imagery is described. The mathematics relevant to the model development is first presented, and then an outline of the flow for the algorithm is given before the testing of the algorithm using Envisat data and a comparison in performance with Radarsat. The test data used is described in section 7.3.

5.2 Intersection Theory

Consider two radar satellites in space, imaging the same ground location such that a pair of overlapping images is acquired. The solution for the ground position of any conjugate point - determined from the stereo matching process - will be the intersection of the range and Doppler equations formed for each satellite. This is based on the stereo principle whereby the complete 3D position of a ground point can be determined by imaging the same point from two different positions in space. Figure 5.1 illustrates the basic principle involved in the space intersection for a same side repeat-pass orbit pair.

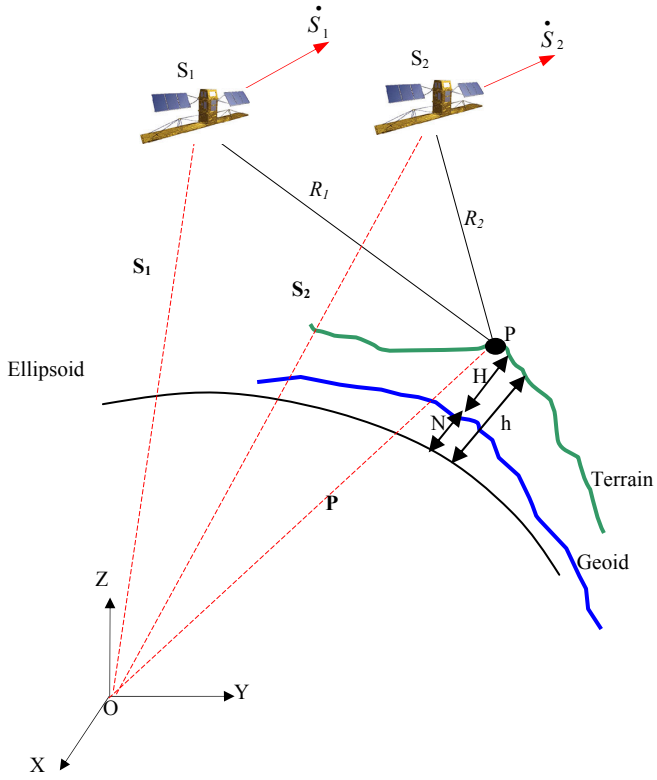

Figure 5.1: Space Intersection Principle

Here, the ground point P is being imaged from satellite positions S_1 and S_2; $\dot{S}_1$ and $\dot{S}_2$ are the velocity vectors while $\mathbf{S_1}$ and $\mathbf{S_2}$ represent the position vectors of the respective satellites. P is the location of the ground point and its position vector given by **P**. The orthometric height (H) of point P is usually determined by subtracting the geoidal height (N) from the ellipsoid height (h). Several models exist for geoidal height; in the Caribbean it is the Carib97 and globally it is the EGM96. The quality of the geoidal model will affect the final elevations.

In the figure, all position vectors are given with respect to a geocentric Earth Centred Earth Fixed (ECEF) Cartesian system with its centre at O. The range and Doppler equations, which were first proposed by *Curlander 1982* for the geocoding of single SAR images, can be formed for each satellite orbit and used as observation equations in the space intersection process. The basic equations for a single satellite are given as (*Curlander 1982)*:

Range Equation:

$$R^2 = |\mathbf{S} - \mathbf{P}|^2 \qquad [5.1]$$

Doppler Equation:

$$f_D = \frac{2(\mathbf{S} - \mathbf{P}) \bullet (\dot{\mathbf{S}} - \dot{\mathbf{P}})}{\lambda |\mathbf{S} - \mathbf{P}|} \qquad [5.2]$$

Where:

S - the state vector to the observing satellite

P - the position vector of the target point on ground with coordinates (X_P, Y_P, Z_P)

$\dot{S}$ - the velocity vectors of that satellite

X^S,Y^S,Z^S - the coordinates for the position of the satellite

R - the ranges measured from satellite (S)

f_D - the Doppler shift frequencies for the images from satellite (S)

λ - the wavelength of the coherent signal used by the sensor

$\dot{P}$ - the velocity vector of the target point on the earth's surface i.e $\dot{P} = \boldsymbol{P}^*\boldsymbol{\omega_e}$

($\boldsymbol{\omega_e} = [0 \;\; 0 \;\; \omega_e]^T$, $\omega_e = 7.292115167e^{-5}$ rad/sec; the earth rotation constant)

According to *Dowman 1992* and *Chen and Dowman 2001*, the problem of space intersection can be solved for the unknown ground point P (X, Y, Z) using the basic equations [5.1] and [5.2] for two same-side orbits to form a system of four observation equations:

$$F_1 = [(X^{S1}-X_P)^2 + (Y^{S1}-Y_P)^2 + (Z^{S1}-Z_P)^2] - (R_1)^2 \quad [5.3]$$

$$F_2 = [(X^{S2}-X_P)^2 + (Y^{S2}-Y_P)^2 + (Z^{S2}-Z_P)^2] - (R_2)^2 \quad [5.4]$$

$$F_3 = \frac{2(\mathbf{S}_1 - \mathbf{P}) \bullet (\dot{\mathbf{S}}_1 - \dot{\mathbf{P}})}{\lambda |\mathbf{S}_1 - \mathbf{P}|} - f_{D1} \quad [5.5]$$

$$F_4 = \frac{2(\mathbf{S}_2 - \mathbf{P}) \bullet (\dot{\mathbf{S}}_2 - \dot{\mathbf{P}})}{\lambda |\mathbf{S}_2 - \mathbf{P}|} - f_{D2} \quad [5.6]$$

In their study, *Dowman and Chen* performed the space intersection solution in an Inertial Coordinate system, maybe because the state vectors for Radarsat are usually given in that system. But if we consider performing the solution in an Earth Centred Earth Fixed (ECEF) system, then the intersection solution can be greatly simplified, thus increasing the processing speed of the algorithm without much loss in accuracy. The SAR imagery from Radarsat-1 and Envisat ASAR sensors are usually given in Zero-Doppler format which means that $f_D = 0$, which further suggests that the resultant velocity vector $(\dot{\mathbf{S}} - \dot{\mathbf{P}})$ is orthogonal to the resultant range vector $(\mathbf{S} - \mathbf{P})$; in other words:

$$f_D = (\mathbf{S} - \mathbf{P}) \bullet (\dot{\mathbf{S}} - \dot{\mathbf{P}}) = 0. \quad [5.7]$$

By converting the state vectors to an ECEF system, the velocity of the ground point can be equated to zero thus simplifying equation [5.7] further, leading to:

$$f_D = (\mathbf{S} - \mathbf{P}) \bullet \dot{\mathbf{S}} = 0 \quad [5.8]$$

The simplified system of equations now becomes:

$$
\left.
\begin{aligned}
F_1 &= [(X^{S1}-X_P)^2 + (Y^{S1}-Y_P)^2 + (Z^{S1}-Z_P)^2] - (R_1)^2 \\
F_2 &= [(X^{S2}-X_P)^2 + (Y^{S2}-Y_P)^2 + (Z^{S2}-Z_P)^2] - (R_2)^2 \\
F_3 &= (\mathbf{S_1} - \mathbf{P}) \bullet \dot{\boldsymbol{S}}_1 - f_{D1} \\
F_4 &= (\mathbf{S_2} - \mathbf{P}) \bullet \dot{\boldsymbol{S}}_2 - f_{D2}
\end{aligned}
\right\} \qquad [5.9]
$$

In the system of equations [5.9], the position of the satellites and the ranges to the ground point can be computed from information contained in the header files for both images. The coordinates of the earth point P are the only unknowns in the equations and the solution of these four equations will lead to the values for the three unknowns. Because the solution is over determined, i.e. four equations and three unknowns, a rigorous approach such as that of least squares (*Mikhail 1976*) would be adopted to determine the position vector $\mathbf{P} = [X_P, Y_P, Z_P]^T$ of the ground point.

5.3 Conversion of State Vectors

Before any attempt is made to solve the unknown position of (P), the position of the satellites must be located in their respective orbits. Since the state vectors modelling the Radarsat satellite in its orbital cycle are given in an inertial system, they must be somehow related to each other. An obvious approach would be to rotate the state vectors of each satellite into the ECEF system which would greatly simplify computations. The relationship between the Earth Centred Inertial (ECI) system and the ECEF system is given in Figure 5.2.

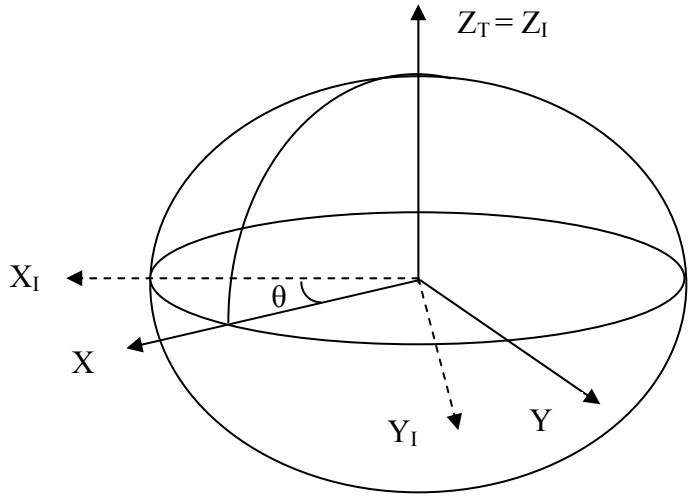

Figure 5.2: *Relationship between ECI and ECEF systems*

Both systems are Cartesian and their centres are assumed to coincide with the centre of mass of the earth. X_I is in the direction of the first point of Aires, Z_I coincides closely with the main spin axis of the earth and Y_I completes the right- handed Cartesian ECI system. The ECEF system is defined by X_T pointing in the direction of the intersection of the Greenwich meridian and the equator; Z_T coinciding with the mean spin axis of the earth and Y_T completing the right-handed Cartesian system. The Greenwich Apparent Sidereal Time (GAST) is the angle separating the two systems; in Figure 5.2 this angle GAST is represented by θ. It follows therefore, that the ECEF coordinates of the satellite can be found by rotating the Inertial Reference Frame of the ECI system about the Z axis by an amount θ.

$$\begin{bmatrix} X \\ Y \\ Z \end{bmatrix}_T = R(\theta) \begin{bmatrix} X \\ Y \\ Z \end{bmatrix}_I$$

Where R(θ) implies a rotation about the Z axis and given by:

$$\begin{bmatrix} Cos\theta & Sin\theta & 0 \\ -Sin\theta & Cos\theta & 0 \\ 0 & 0 & 1 \end{bmatrix}$$

Hence

$$\begin{bmatrix} X \\ Y \\ Z \end{bmatrix}_T = \begin{bmatrix} Cos\theta & Sin\theta & 0 \\ -Sin\theta & Cos\theta & 0 \\ 0 & 0 & 1 \end{bmatrix} \begin{bmatrix} X \\ Y \\ Z \end{bmatrix}_I \qquad [5.10]$$

Equation [5.10] rotates the position vector into the ECEF system. The velocity vector of the satellite has to be converted to the ECEF system as well. This is accomplished using equation [5.11] which takes into account the rotation of the earth using the universal earth rotation constant ω_e (*Clarke 1991*).

$$\begin{bmatrix} \dot{X} \\ \dot{Y} \\ \dot{Z} \end{bmatrix}_T = \begin{bmatrix} -\omega_e Sin\theta & \omega_e Cos\theta & 0 \\ -\omega_e Cos\theta & -\omega_e Sin\theta & 0 \\ 0 & 0 & 0 \end{bmatrix} \begin{bmatrix} X \\ Y \\ Z \end{bmatrix}_I + \begin{bmatrix} Cos\theta & Sin\theta & 0 \\ -Sin\theta & Cos\theta & 0 \\ 0 & 0 & 1 \end{bmatrix} \begin{bmatrix} \dot{X} \\ \dot{Y} \\ \dot{Z} \end{bmatrix}_I \qquad [5.11]$$

This could be simplified using results from equation [5.10], leading to:

$$\left.\begin{aligned} \dot{X}_T &= \omega_e Y_T + \dot{X}_I \text{Cos } \theta + \dot{Y}_I \text{Sin } \theta \\ \dot{Y}_T &= -\omega_e X_T - \dot{X}_I \text{Sin } \theta + \dot{Y}_I \text{Cos } \theta \\ \dot{Z}_T &= \dot{Z}_I \end{aligned}\right\} \qquad [5.12]$$

The angle GAST (θ) is critical for the successful conversion of the state vectors and it should be determined as accurately as possible and is related to Greenwich Mean Sidereal Time (GMST) by:

$$\text{GAST} = \text{GMST} + \textit{equation of equinox}$$

Clarke 1991 and *Twu 1996*, in their work with SIR-B and ERS data at University College London (UCL), ignored the determination of the *equation of equinox* citing the difficulty in calculating its value; thus equating GAST to GMST for the purpose of their work. Indeed, based on work carried out by *Agrotis 1984* and *Moore 1986* the computation of a value for the *equation of equinox* is not at all trivial. However, *Goncalves and Dowman 1998* pointed out that ignoring this value can lead to an error of up to 35m when converting from ECI to ECEF coordinates. Fortunately, in this present study with Radarsat data, a value of GAST for the first state vector at time (t_0) is contained within the image header file. GAST for all other satellite positions at time (t) can then be determined using the following relationship (*Goncalves and Dowman 1998)*:

$$\text{GAST}(t) = \text{GAST}(t_0) + 1.002\,737\,822(t - t_0)\,\frac{2\pi}{86400} \qquad [5.13]$$

The state vectors for the Envisat satellite are usually given in an ECEF coordinate system; hence no conversion is necessary for the orbital data from this satellite.

5.4 Determination of Satellite Position and Velocity

The state vectors for the satellite positions are usually given at evenly spaced intervals and for Radarsat this interval is usually 480 seconds, making it the least precise orbital information when compared with ERS and Envisat which are usually given at approximately 4 second intervals. For the space intersection solution it is necessary to determine the position of the satellite in its orbit at a given azimuth line in the image which will never usually coincide with the spacing of the state vectors, given that the entire image sequence is recorded in approximately 13 seconds. The two main procedures for determining satellite position and velocity is by *interpolation* of a series of narrowly spaced state vectors or by *propagating* an orbit, based on a starting position and knowledge of the forces acting upon the satellites.

Various authors have used several procedures for this task. *Twu 1996* used a cubic spline to interpolate the orbit for ERS satellites, while *Goncalves and Dowman 1998* used a gravity force model and a Runge-Kutta integrator on Radarsat orbits for geocoding. *Chen 2000* worked with Radarsat orbits but did not outline his procedure for determining satellite positions.

5.4.1 Orbit Propagation

In this method of determining the position and velocity, the forces acting on the satellite are modelled. *Agrotis 1984* identified these forces as: (1) gravitational, due to the influences of the earth, moon, sun & planets; and (2) surface forces such as atmospheric drag. The greatest influence on Low Earth Orbiting (LEO) satellites such as Radarsat and Envisat is due mainly to the gravitational attraction of the earth and this effect can be modelled using the potential function given by *Jon 1991*:

$$U = \frac{GM}{r}\left[1 - \sum_{n=2}^{\infty} J_n \left(\frac{a_e}{r}\right)^n P_n \sin\varphi\right] \qquad [5.14]$$

where:

GM - universal gravitational constant

r - radius of the satellite orbit

a_e - radius of the earth

J_n - represents coefficients determined from observations

$P_n \sin\varphi$ - Legendre polynomial

n - the degree of the expansion

The acceleration of the satellite due to the earth's gravity field can then be determined by taking the gradient of the potential, ∇U. From the resulting acceleration vector, the position and velocity (state vector) of the satellite can be determined by integrating once for the velocity and twice for the position. Restricting Equation 5.14 to an expansion order of n = 4, the mathematical models for the acceleration in the X, Y and Z components are given by *Seeber 2003* as:

$$\left.\begin{aligned}
\ddot{X} &= \frac{GMX}{r^3}\left(1 - J_2\frac{3}{2}\left(\frac{a_e}{r}\right)^2\left(5\frac{Z^2}{r^2}-1\right) + J_3\frac{5}{2}\left(\frac{a_e}{r}\right)^3\left(3\frac{Z}{r}-7\frac{Z^3}{r^3}\right) - J_4\frac{5}{8}\left(\frac{a_e}{r}\right)^4\left(3-42\frac{Z^2}{r^2}+63\frac{Z^4}{r^4}\right)\right)\\
\ddot{Y} &= \frac{GMY}{r^3}\left(1 - J_2\frac{3}{2}\left(\frac{a_e}{r}\right)^2\left(5\frac{Z^2}{r^2}-1\right) + J_3\frac{5}{2}\left(\frac{a_e}{r}\right)^3\left(3\frac{Z}{r}-7\frac{Z^3}{r^3}\right) - J_4\frac{5}{8}\left(\frac{a_e}{r}\right)^4\left(3-42\frac{Z^2}{r^2}+63\frac{Z^4}{r^4}\right)\right)\\
\ddot{Z} &= -\frac{GMX}{r^3}\left(1 + J_2\frac{3}{2}\left(\frac{a_e}{r}\right)^2\left(3-5\frac{Z^2}{r^2}\right) + J_3\frac{3}{2}\left(\frac{a_e}{r}\right)^3\left(10\frac{Z}{r}-\frac{35}{3}\frac{Z^3}{r^3}-\frac{r}{Z}\right) - J_4\frac{5}{8}\left(\frac{a_e}{r}\right)^4\left(15-70\frac{Z^2}{r^2}+63\frac{Z^4}{r^4}\right)\right)
\end{aligned}\right\} \quad [5.15]$$

Numerical integration of the acceleration vector can be obtained using the widely known 4th order *Runge-Kutta* method, for which algorithms are available in *Press et al. 2002*. An initial state vector, the step size (in seconds) and values for J_n will be required. In this study, only values for J_2, J_3 and J_4 were available in the image header so all terms higher than J_4 were ignored; moreover, it is well known that these terms are insignificant when compared to the effect of J_2. Figure 5.3 outlines the steps.

This method is only appropriate if the initial state vector is in an ECI system. Given that the Envisat orbits are in an ECEF system, this method of orbit determination

would not be suitable. One advantage of this method is that only one state vector is required. The disadvantage is that the process is computationally intensive.

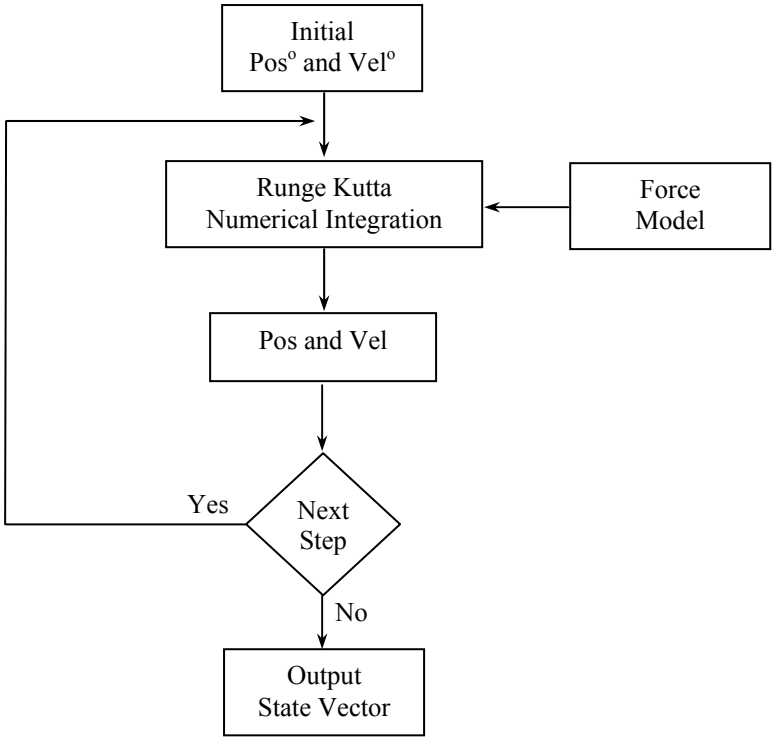

Figure 5.3: *Flow Diagram for Orbit Propagation Method*

5.4.2 Orbit Interpolation

Interpolation is essentially a method of estimating values that lie between two known values. Several techniques exist for the interpolation and the most common are cubic spline and polynomials. *Shukla 2001* made graphical comparisons between the different methods for interpolating narrowly spaced data and concluded that the cubic spline offers the best solution. *Goncalves and Dowman 1998* reported that polynomials or cubic spline are inappropriate for use on the widely spaced orbital data of Radarsat and will lead to poor quality interpolated values and suggest the use of orbit propagation techniques.

Interpolation of SAR satellite orbits have been restricted in the past to the more accurate orbit of ERS using cubic spline (for example, *Twu 1996*). The Envisat orbits are similarly spaced to the ERS; therefore, the cubic spline would also be appropriate for interpolating this orbit. The mathematical model defining the cubic spline can be found in any *numerical recipes* book which also contain source code and will not be outlined here (see *Press et al. 2002*).

The IESSG at the University of Nottingham have been involved with the interpolation of GPS orbits for some time now. For this purpose they utilized an *Everett* method for interpolation (see *Agrotis 1984* and *Moore 1986*). Until now, this method has not been considered for the interpolation of the widely spaced Radarsat orbits and if successful, could drastically improve processing time for the space intersection algorithm when compared to orbit propagation methods which are quite computer intensive.

Given a function *f(t)* which has data points at discrete locations t_i, at a constant interval *dt*, then the function can be interpolated within the interval t_i to t_{i+1} by using the Everett central difference formulae (*HMSO 1956* and *Fox 1958*):

$$f(t) = E_0 f(t_i) + E_2 \delta^2 f(t_i) + E_4 \delta^4 f(t_i) + E_6 \delta^6 f(t_i) + E_8 \delta^8 f(t_i) + E_{10} \delta^{10} f(t_i) + ..$$
$$+ F_0 f(t_{i+1}) + F_2 \delta^2 f(t_{i+1}) + F_4 \delta^4 f(t_{i+1}) + F_6 \delta^6 f(t_{i+1}) + F_8 \delta^8 f(t_{i+1}) + F_{10} \delta^{10} f(t_{i+1}) + ..$$

where

$$u = \frac{t - t_i}{dt}$$

$$E_0 = 1 - u \qquad E_2 = \frac{u(1-u)(2-u)}{3!}$$

$$E_4 = \frac{(-1-u)u(1-u)(2-u)(3-u)}{5!} \qquad E_6 = (u+2)E_4(u-4)\frac{3!\ 5!}{7!}$$

$$E_8 = (u+3)E_6(u-5)\frac{3!\ 5!\ 7!}{9!} \qquad E_{10} = (u+4)E_8(u-6)\frac{3!\ 5!\ 7!\ 9!}{11!}$$

and

$$F_0 = u \qquad F_2 = \frac{u(u^2-1)}{3!}$$

$$F_4 = \frac{u(u^2-1)(u^2-4)}{5!} \qquad F_6 = (u+3)F_4(u-3)\frac{3!\ 5!}{7!}$$

$$F_8 = (u+4)F_6(u-4)\frac{3!\ 5!\ 7!}{9!} \qquad F_{10} = (u+5)F_8(u-5)\frac{3!\ 5!\ 7!\ 9!}{11!}$$

The term $\delta^n f(t_i)$ is the n[th] central difference of the function $f(t_i)$ such that

$$\delta^2 f(t_i) = f(t_{i-1}) - 2f(t_i) + f(t_{i+1})$$

$$\delta^4 f(t_i) = f(t_{i-2}) - 4f(t_{i-1}) + 6f(t_i) - 4f(t_{i+1}) + f(t_{i+2})$$

$$\delta^6 f(t_i) = f(t_{i-3}) - 6f(t_{i-2}) + 15f(t_{i-1}) - 20f(t_i) + 15f(t_{i+1}) - 6f(t_{i+2}) + f(t_{i+3})$$

$$\delta^8 f(t_i) = f(t_{i-4}) - 8f(t_{i-3}) + 28f(t_{i-2}) - 56f(t_{i-1}) + 70f(t_i) - 56f(t_{i+1}) + 28f(t_{i+2}) - 8f(t_{i+3}) + f(t_{i+4})$$

$$\delta^{10} f(t_i) = f(t_{i-5}) - 10f(t_{i-4}) + 45f(t_{i-3}) - 120f(t_{i-2}) + 210f(t_{i-1}) - 252f(t_i) + 210f(t_{i+1}) - 120f(t_{i+2}) + 45f(t_{i+3}) - 10f(t_{i+4}) + f(t_{i+5})$$

The normal practice is to truncate the series after the n^{th} central difference, where n must be an even integer. This implies that n+2 data points must be available and evenly distributed both sides of t. For the Radarsat satellite, 12 state vectors are available which mean that the 10[th] order is the highest that can be achieved using the Everett method.

5.4.3 Experimental Results

Using the data provided for this research, several tests were conducted to select the orbit determination method(s) that would be most appropriate for the GCP-free space intersection algorithm. The quality of the Radarsat orbit as indicated by Radarsat International is 20m radial, 20m across-track and 100m along track. The quality of the Envisat DORIS orbit is better than 20cm in all directions. These tests and the results achieved are outlined below.

Determination of Runge-Kutta Step Size

As mentioned before, in this study the orbit integration algorithm applies a 4th order Runge-Kutta single step method to numerically integrate the resultant acceleration on the satellite. To determine the optimal step size to be used, experiments were conducted using two Radarsat state vectors in the ECI system – one to start the propagation and the other to act as a check on the results. Table 5.1 shows the state vector pair chosen for three SAR images – two standard and one wide mode, while Table 5.2 summarizes the satellite and earth parameters extracted from the image header and utilized by the propagation algorithm.

Table 5.1: *Known starting (t_o) and ending (t_1) state vectors for each image set*

Image Mode		**X (m)**	**Y (m)**	**Z (m)**	$\dot{X}$ **(m/s)**	$\dot{Y}$ **(m/s)**	$\dot{Z}$ **(m/s)**
W2	t_o	5322975.68	-2232128.66	4248024.97	3480.48216	-2956.37201	-5897.94219
	t_1	6275225.10	-3320458.71	1013579.44	404.36889	-1483.71019	-7297.10634
S7	t_o	1011569.51	-5679920.12	4251824.92	-596.19119	-4531.41612	-5894.91692
	t_1	613652.18	-7072357.66	1018315.76	-1027.23593	-1149.29251	-7296.31839
S1	t_o	619803.65	-5736838.94	4250641.43	-905.61052	-4478.60453	-5895.81502
	t_1	127283.06	-7098030.73	1016868.07	-1103.76398	-1074.62113	-7296.50231

Table 5.2: *Satellite and earth parameters*

Reference Ellipsoid (a_e)		6378140 m
Earth's Gravity Field	J_2	1.0826158×10^{-3}
	J_3	$-2.5388099 \times 10^{-6}$
	J_4	-1.65597×10^{-6}
Gravitational Constant (GM)		$3.98599446 \times 10^{-14}$

The propagation algorithm starts with t_o and determines the state vector 480 seconds later using steps of 1, 2, 3, 4, 5, 10, 15, 30, 60, 120, 240 and 480 seconds. The computed position and velocity were compared with the known values at t_1 and the difference tabulated. The results for each of the three images are shown in Table 5.3, Table 5.4 and Table 5.5.

Table 5.3: *Experimental Results Using W2 State Vectors*

Step Size	dX	dY	dZ	$d\dot{X}$	$d\dot{Y}$	$d\dot{Z}$
1	10.730	-6.458	5.185	0.0328	-0.0332	0.0002
2	10.730	-6.458	5.185	0.0328	-0.0332	0.0002
3	10.730	-6.458	5.185	0.0328	-0.0332	0.0002
4	10.730	-6.458	5.185	0.0328	-0.0332	0.0002
5	10.730	-6.458	5.185	0.0328	-0.0332	0.0002
10	10.730	-6.458	5.185	0.0328	-0.0332	0.0002
15	**10.731**	**-6.459**	**5.184**	**0.0328**	**-0.0332**	**0.0002**
30	10.744	-6.470	5.164	0.0328	-0.0332	0.0002
60	10.958	-6.644	4.841	0.0332	-0.0334	0.0005
120	14.729	-9.631	-0.317	0.0394	-0.0362	0.0041
240	85.345	-63.573	-85.354	0.1399	-0.0846	0.04887
480	1466.499	-1105.401	-1672.892	1.568	-0.8585	0.1769

Table 5.4: *Experimental Results Using S7 State Vectors*

Step Size	dX	dY	dZ	$d\dot{X}$	$d\dot{Y}$	$d\dot{Z}$
1	2.009	-12.574	6.219	-0.0056	-0.0495	0.0043
2	2.009	-12.574	6.219	-0.0056	-0.0495	0.0043
3	2.009	-12.574	6.219	-0.0056	-0.0495	0.0043
4	2.009	-12.574	6.219	-0.0056	-0.0495	0.0043
5	2.009	-12.574	6.219	-0.0056	-0.0495	0.0043
10	2.009	-12.574	6.218	-0.0056	-0.0495	0.0043
15	**2.009**	**-12.575**	**6.217**	**-0.0056**	**-0.0495**	**0.0043**
30	2.007	-12.591	6.197	-0.0056	-0.0496	0.0043
60	1.977	-12.866	5.875	-0.0055	-0.0500	0.0046
120	1.512	-17.657	0.720	-0.0045	-0.0567	0.0081
240	-5.508	-106.292	-84.254	0.0094	-0.1673	0.0530
480	-131.735	-1832.680	-1670.545	0.134	-1.786	0.182

Table 5.5: *Experimental Results Using S1 State Vectors*

Step Size	dX	dY	dZ	$d\dot{X}$	$d\dot{Y}$	$d\dot{Z}$
1	-1.975	-11.842	3.868	-0.0167	-0.0390	-0.0042
2	-1.975	-11.842	3.868	-0.0167	-0.0390	-0.0042
3	-1.975	-11.842	3.868	-0.0167	-0.0390	-0.0042
4	-1.975	-11.842	3.868	-0.0167	-0.0390	-0.0042
5	-1.975	-11.842	3.868	-0.0167	-0.0390	-0.0042
10	-1.975	-11.842	3.868	-0.0167	-0.0390	-0.0042
15	**-1.975**	**-11.843**	**3.866**	**-0.0167**	**-0.0390**	**-0.0042**
30	-1.978	-11.859	3.846	-0.0167	-0.0390	-0.0042
60	-2.028	-12.131	3.524	-0.0167	-0.0394	-0.0039
120	-2.819	-16.878	-1.632	-0.0162	-0.0462	-0.0003
240	-15.902	-104.801	-86.620	-0.0099	-0.1575	0.0445
480	-260.227	-1818.067	-1673.191	0.0030	-1.7810	0.1734

It can be observed that in all three cases there is no benefit in using a step smaller than 15 seconds so this step size was chosen for use with the Runge-Kutta integration. It should also be noted that when using a step size of 15 seconds the maximum orbit deviation from the known value would be approximately 12.5 m as seen in the Y component in Table 5.4 which is well within the accuracy of the satellite orbit and about the pixel spacing of the imagery. The main draw back with this method is that it is very time consuming.

Significance of Ignoring Terms Higher than J_2

In the orbit propagation method, terms up to J_4 can be utilized in modelling the influences on the SAR satellite. The significance of using terms higher than J_2 was tested by selecting a pair of state vectors and propagating the orbit in steps of 15 sec from one state vector to the other using first, J_2 only terms and second, all terms up to J_4. A comparison between the two sets of results was made and the differences are illustrated in Figure 5.4. The largest deviation is approximately -3.5m in the Y axis which is well within the known accuracy of the satellite orbit. There appears to be no benefit in using terms higher than J_2 hence terms higher than J_2 were ignored.

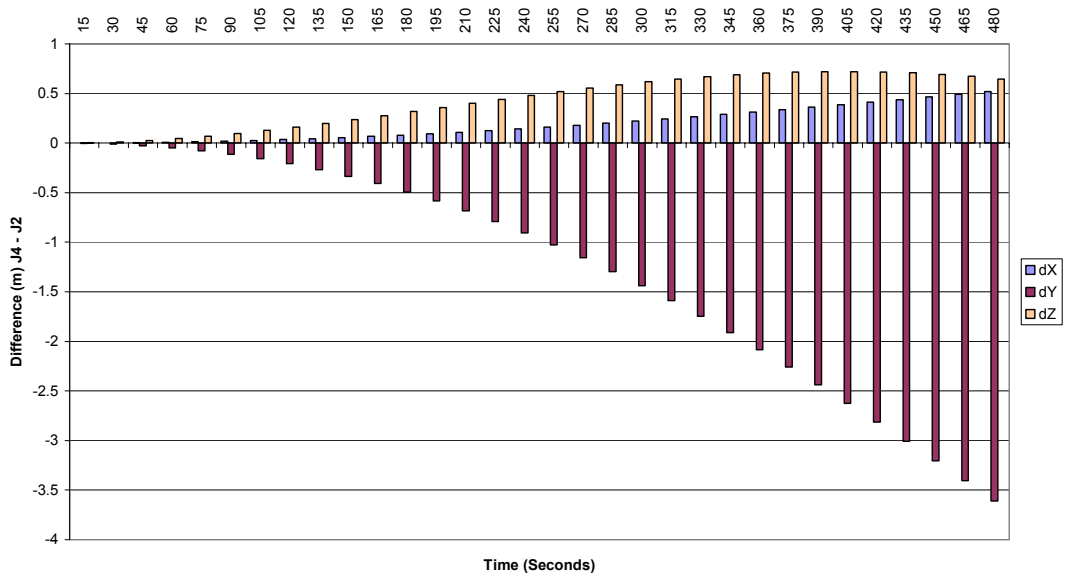

Figure 5.4: *Test of Significance of Ignoring Terms Higher than J_2*

Choice of Order for Everett Interpolation Method

The Everett method can be implemented with a 4^{th}, 6^{th}, 8^{th}, or 10^{th} order. The choice of order will affect the quality of position and velocity interpolated. Experiments were carried out to assess the appropriate Everett order to use in this study. The accurate DORIS orbit for Envisat is available on the internet at intervals of 60 seconds. A segment of this orbit was acquired and filtered to reflect the 480 seconds spacing of Radarsat and the Everett method was used to compute the missing 60 seconds values applying a 6^{th}, 8^{th} and 10^{th} order. The interpolated 60 seconds positions and velocities were compared with the known DORIS values and the differences tabulated. The results are illustrated in Figure 5.5, Figure 5.6 and Figure 5.7. Table 5.6 and Table 5.7 give the summary of the statistics. The results show that an 8^{th} order Everett method would be appropriate for interpolating the widely spaced satellite orbit.

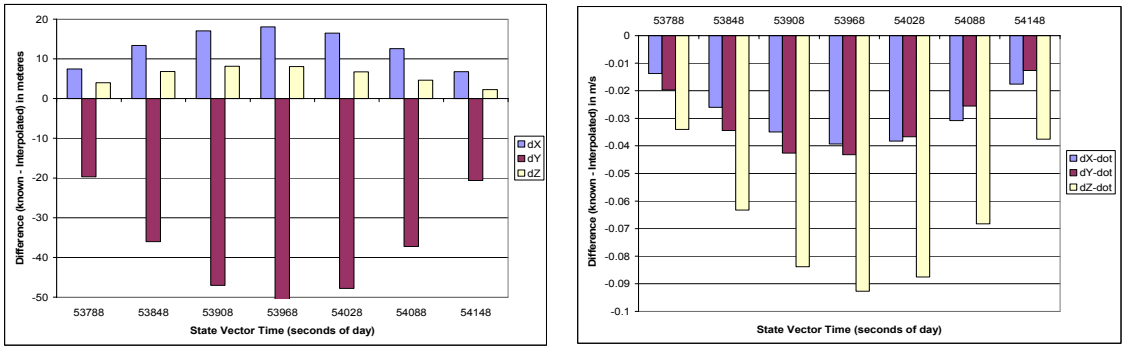

Figure 5.5: *Everett Interpolation at 6^{th} Order. Position differences left, velocities right*

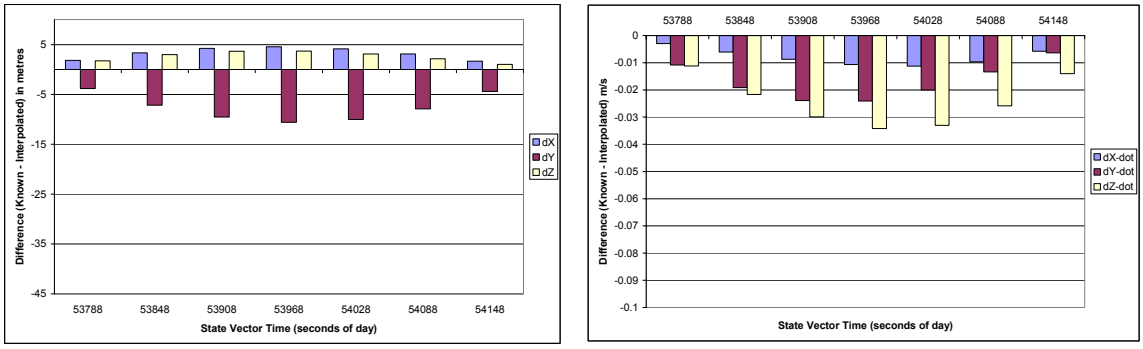

Figure 5.6: *Everett Interpolation at 8^{th} Order. Position differences left, velocities right.*

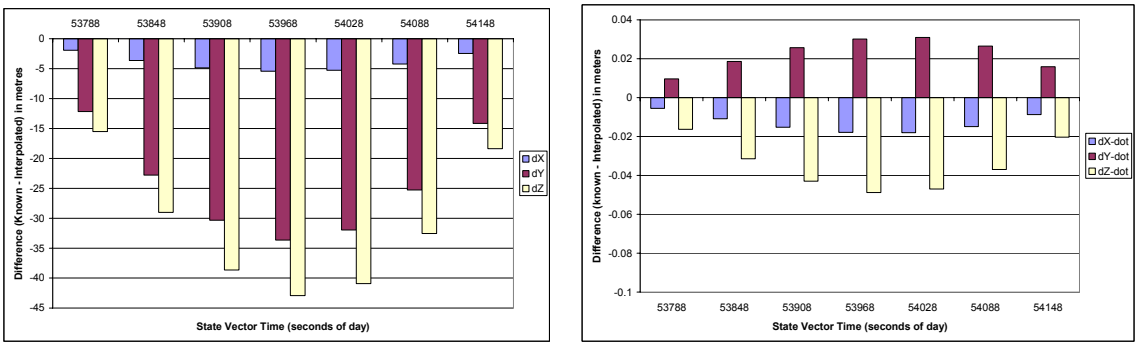

Figure 5.7: *Everett Interpolation at 10th Order. Position differences left, velocities right.*

Table 5.6: *Summary of Statistics for Interpolated Positions*

Interpolation Method		Mean Diff	Std Dev	Min	Max
6th Order Everett	dX	13.103	4.550	6.772	18.092
	dY	-37.053	12.805	-51.106	-19.680
	dZ	5.803	2.227	2.242	8.152
8th Order Everett	**dX**	**3.260**	**1.158**	**1.653**	**4.539**
	dY	**-7.634**	**2.702**	**-10.600**	**-3.817**
	dZ	**2.621**	**1.009**	**1.041**	**3.674**
10th Order Everett	dX	-3.965	1.368	-5.431	-1.929
	dY	-24.333	8.523	-33.644	-12.166
	dZ	-31.132	10.832	-42.905	-15.507

Table 5.7: *Summary of Statistics for Interpolated Velocities*

Interpolation Method		Mean Diff	Std Dev	Min	Max
6th Order Everett	dX	-0.029	0.010	-0.039	-0.014
	dY	-0.031	0.012	-0.043	-0.013
	dZ	-0.067	0.023	-0.093	-0.013
8th Order Everett	**dX**	**-0.008**	**0.003**	**-0.011**	**-0.003**
	dY	**-0.017**	**0.007**	**-0.024**	**-0.006**
	dZ	**-0.024**	**0.009**	**-0.034**	**-0.011**
10th Order Everett	dX	-0.013	0.005	-0.018	-0.006
	dY	0.022	0.008	0.010	0.031
	dZ	-0.035	0.013	-0.049	-0.016

Comparison of Everett Interpolation and Orbit Propagation

To investigate whether there were any significant differences between both methods of orbit determination each method was used to generate state vectors between two predetermined intervals and the results compared. The difference between both methods is presented in Figure 5.8. It is important to note that with the orbit propagation method, the error in the determination increases with distance from the initial state vector. However, with the Everett method the interpolation is controlled at the starting and ending state vectors so that the largest error would most likely be at the mid point, 240 seconds in this case, which show a difference of 5m. The largest difference of 12.5m is at the end and due mainly to the reason stated earlier.

In any case, all differences are much smaller than the known errors in the Radarsat orbits. The Everett interpolator would therefore prove to be a fast and easily implemented method for orbit determination. However, since the software system being developed in this research would be used as a platform for launching other research activities at the IESSG, both methods have been included in the system. Later in this thesis, comparisons will be made to assess the accuracy of the elevations generated from the *IESSG Space Intersection Algorithm* using both orbit determination methods.

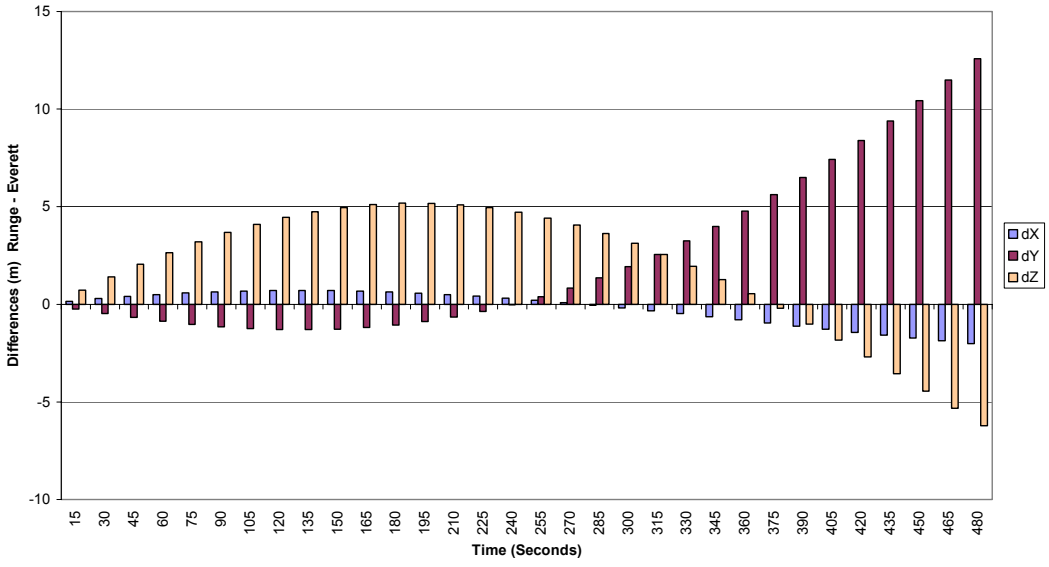

Figure 5.8: *Comparison of Output from Everett and Runge-Kutta Methods*

5.5 Slant Range and Azimuth Time

The image extracted from SAR dataset is usually in a row, column (*r, c*) format similar to the arrangement for most optical imagery. For use in the space intersection algorithm, the location of the pixels must be known with reference to the SAR coordinate system, i.e. the slant range (*R*) and azimuth time (*t*) must be accurately known. It is therefore necessary to define the relation between the (*r, c*) and (*R, t*) coordinates which is illustrated in Figure 5.9.

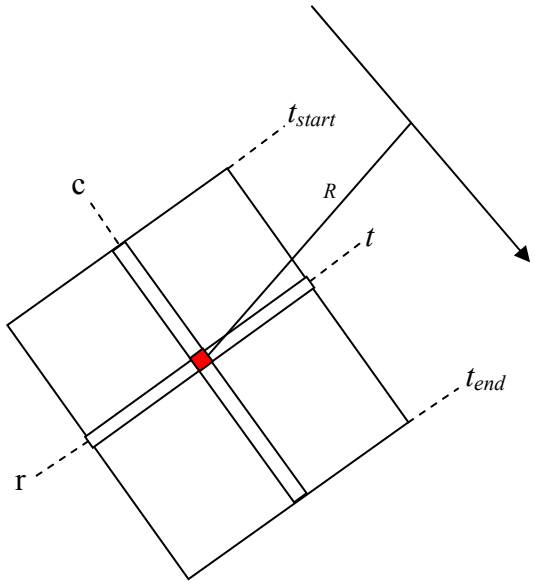

Figure 5.9: *Relationship Between row, column (r, c) and range, time (R, t) Coordinates*

From the header data extracted during the data import, the start and end times (t_{start} and t_{end}) of the image can be easily determined. The number of rows (N_{rows}) and number of columns (N_{cols}) making up the image can also be determined from the header information. The azimuth time *t* for any row *r* in the image can be found using the relationship shown in Equation 5.16.

$$t = t_{start} + \frac{t_{end} - t_{start}}{N_{rows} - 1} \times (r - 0.5) \qquad [5.16]$$

The slant range can be found using a specific polynomial developed for this purpose (see *RSI 2000*), the coefficients for which are contained in the image header and

extracted when the image was imported into the StereoSAR system. The slant range R for any column position c in the image can be found using the following relationship shown in Equation 5.17, where a_i represents the coefficients for the ground range to slant range polynomial.

$$R = \sum_{i=0}^{5} a_i \times (pixel\_spacing \times c)^i \qquad [5.17]$$

5.6 Datum Transformation and Map Projection

The geodetic datum used by the SAR sensors (Radarsat and Envisat) are very similar to the geocentric system used by WGS84. The datums used by most countries on the other hand are non-geocentric; for example, in the Caribbean a different local datum is used for each island and there is no unification of these systems. It is therefore necessary to transform the 3D positions determined in WGS84 to the local datum. The study area (see section 7.1) for this research uses the non-geocentric JAD-69 datum based on a Clarke 1866 ellipsoid. Since sub-metre accuracy was not required, a three parameter transformation was implemented based on the Newsome parameters (*Newsome 2000*) for transforming between WGS84 and JAD-69. After converting to the local ellipsoid, the geographical coordinates need to be projected to the local grid, in this case the Jamaican Grid. The mapping frame adopted in the study area is the Lambert Conformal Conical (LCC) projection with one standard parallel. Parameters for the JAD-69 datum and LCC projection for Jamaica can be found in *Girvan 1984* and these are summarised in Table 5.8.

Two algorithms were developed to perform the datum transformation and map projection functions based on the theory and mathematical models presented by *Moore 2001* and *Maling 1991*. To ensure that the algorithm performed correctly they were tested against known coordinate information selected from the Jamaica Survey Department database. The result of the test is presented in Table 5.9, which shows that the differences are negligible and will not contribute to any errors in the coordinates computed by the space intersection algorithm.

Table 5.8: *Summary of Datum and Map Projection Parameters for Study Area*

System	Jamaica National Grid 1969		
Datum	Name	JAD 1969	
	Ellipsoid (Clarke 1866)	a	6378206.4m
		f	1/294.978
	Shift from WGS84	ΔX	-65.33m
		ΔY	-212.46m
		ΔZ	-387.63m
Map Projection	Name	Lambert Conformal Conic	
	Origin	φ_o	18^o N
		λ_o	77^o W
	Standard Parallel	φ	18^o N
	Scale Factor	SF	1.0000
	False Origin	E	250 000m
		N	150 000m

Table 5.9: *Comparison of Coordinates from Map Projection Algorithm with Known Values*

Projected Coordinates		***Known Coordinates***		***Residuals (Known-Projected)***	
N (m)	***E (m)***	***N (m)***	***E (m)***	***VE (mm)***	***VN (mm)***
146944.516	272270.380	146944.520	272270.379	4	-1
145167.601	279735.120	145167.604	279735.120	3	0
142975.499	273102.093	142975.501	273102.091	2	-2
142049.258	273571.576	142049.261	273571.576	3	0
142835.135	271623.935	142835.139	271623.935	4	0
199448.275	189953.617	199448.274	189953.617	-1	0
174799.487	164804.726	174799.487	164804.725	0	-1
184123.777	267568.727	184123.776	267568.727	-1	0
148118.128	272251.182	148118.129	272251.181	1	-1
142499.586	266561.280	142499.587	266561.280	1	0
			RMSE	**2**	**1**

5.7 The Space Intersection Algorithm Design

The theories and mathematical models presented in the previous sections were used to develop what will be referred to in this study as the *IESSG Space Intersection Algorithm,* which is one of the objectives of this research. The algorithm assumes that a file containing the list of conjugate points, determined during the stereo matching phase, exists on the computer executing the program. The flow of the algorithm is illustrated in the block diagram shown in Figure 5.10. This algorithm has been coded in C# and tested with Radarsat and Envisat images of the study area; the experimental results are given in section 5.8.

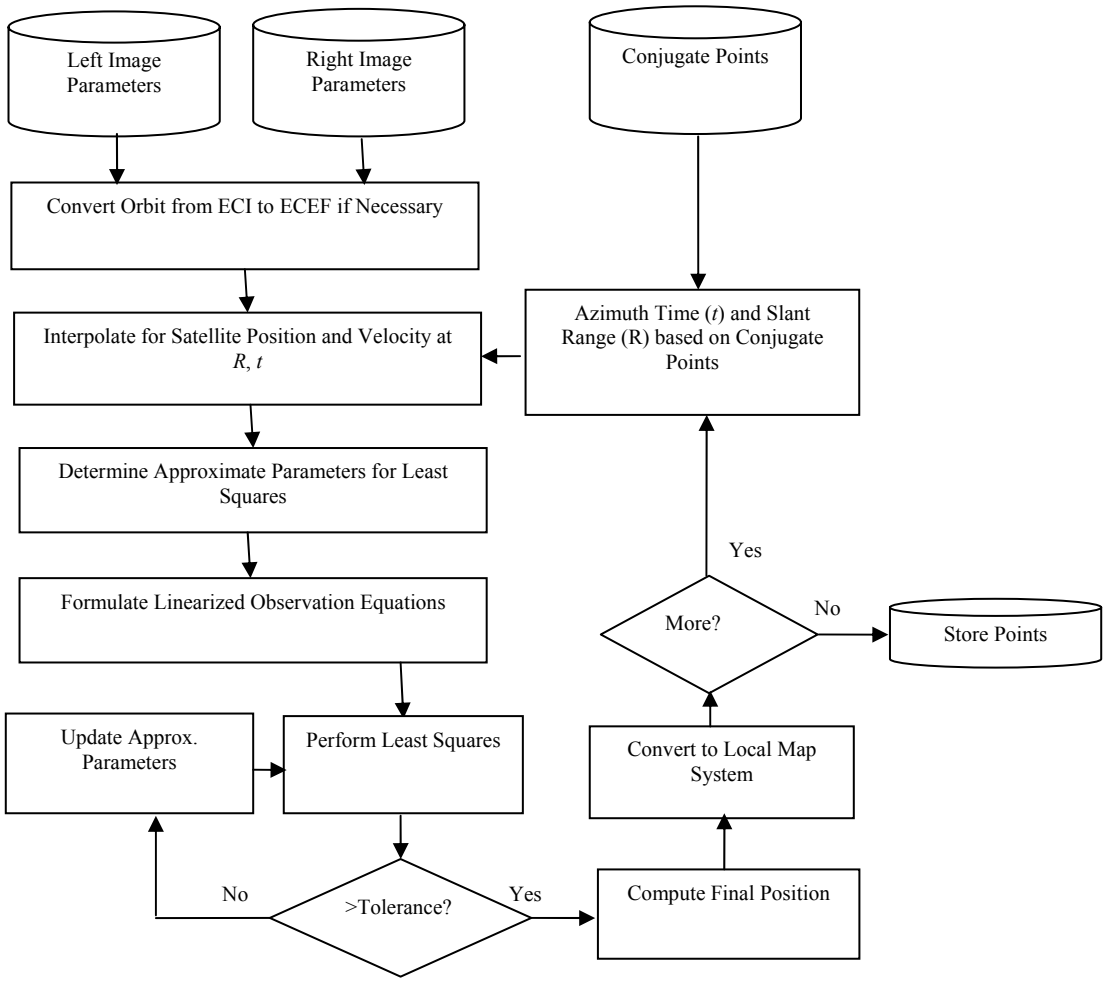

Figure 5.10: *Flow Diagram for the IESSG Space Intersection Algorithm*

5.8 Performance of the Space Intersection Algorithm

To assess the performance of the IESSG Space Intersection Algorithm, only 28 clearly visible points over the entire expanse of the SAR image could be found. The points included: jetties, intersection of roads, bridges, intersection of road and railways, airport runway, reservoir corners, etc. Most of these points were along the coastline of the island and therefore not optimally distributed over the entire scene due mainly to the lack of suitably contrasting and easily identifiable locations, which is a major problem when attempting to extract features for SAR imagery. This is why space intersection algorithms that do not rely on GCPs in their formulation are needed. Nevertheless, these check points proved useful in validating the algorithm.

In the case of Radarsat, the Erdas Imagine software was used to manually extract the image coordinates of the check points for input to the space intersection algorithm outlined earlier in Figure 5.10. For Envisat, the Beam 3.1 toolkit, readily available on the internet (www.brockmann-consult.de), was used for the manual image coordinates extraction. Manual measurement accuracy was estimated at ± 1 pixel. The known planimetric positions of the check points were determined from the precision IKONOS imagery product generated by *Space Imaging* and 1:50 000 scale topographic maps available for the study area (see section 7.3), while the elevations at these known locations were extracted from the reference DSM. The accuracy of the known values for the check points are estimated to be 2m in plan and 2m to 5m in elevation depending on the slope of the terrain where the point is located. The results obtained using the space intersection algorithm are presented in the following sections and have also been published in *Edwards et al. 2004*.

There are very few published works with which to compare our results. Work done by *Chen and Dowman 2001* showed results of: -62m to + 54m in Easting; -60m to +42m in Northing; and -34m to +24m in Height. This is after using two GCPs to remove systematic errors. Their results also showed that there was no improvement in height between using a weighted and non-weighted least squares approach for the space intersection.

5.8.1 Performance Using Envisat

Several stereo pairs were formed based on the available Envisat imagery. The results from the space intersection algorithm, after comparison with the known coordinates, are presented in Table 5.10. The first observation made is that there is great consistency between the means of all four sets of stereo pairs. Surprisingly, the systematic biases in the heights are the lowest at less than 7.5m which implies that no GCPs whatsoever are required when using imagery from the Envisat satellite in this space intersection algorithm. The biases in the along-track direction are the largest at ~25m. This is about the resolution of the Envisat sensor and within the measurement accuracy. *Chen 2000* implemented a weighted least squares technique that had the effect of reducing the biases in the along-track direction. Unfortunately this reduction was only of the order of ~ 2m and may not be worth the additional processing time for the algorithm, especially in a low-cost system.

Table 5.10: *Accuracy Statistics of Check Points from Space Intersection Using Envisat Data*

Stereo Pair	***Intersection***	***Component***	***Mean***	***Std Dev***	***Min***	***Max***	***Spread***
IS2 IS6	18°	N	24.8	9.4	6.5	45.3	38.8
		E	7.7	13.9	-13.6	46.9	60.5
		H	-4.1	6.7	-19.0	10.0	29.0
IS3 IS6	12°	N	24.1	11.8	11.1	63.3	52.2
		E	10.7	15.6	-22.6	38.9	61.5
		H	-7.5	11.5	-29.0	11.0	40.0
IS2 IS7	21°	N	26.5	9.5	12.2	47.4	35.2
		E	5.8	14.1	-11.4	33.3	44.7
		H	-1.1	8.8	-13.0	17.0	30.0
IS3 IS7	15°	N	25.6	9.4	8.9	36.9	28.0
		E	4.9	19.4	-28.3	28.9	57.2
		H	-1.0	14.5	-29.0	18	47.0

5.8.2 Performance Using Radarsat

From the Radarsat datasets available for this research two stereo pairs were formed. The results presented in Table 5.11 show systematic biases in all directions with the greatest being in the height component (H) of the order of 50m. The standard deviation (std. dev.) suggests that if the systematic trend can be removed, then height accuracy of ~ 12 – 20m can be achieved. Except for the height component there appear to be no consistency in the biases between the two sets of stereo pairs. These results suggest that when using Radarsat imagery, if accuracy in height of better than 50m is required then GCP points will be required to remove the systematic bias in the height.

Table 5.11: *Accuracy Statistics of Check Points from Space Intersection Using Radarsat Data*

Stereo Pair	***Intersection***	***Component***	***Mean***	***Std Dev***	***Min***	***Max***	***Spread***
S1 S7	23°	N	44.7	15.8	16.0	94.9	78.9
		E	15.3	18.6	-22.2	52.9	75.0
		H	-51.3	11.7	-80.0	-35.0	45.0
W2 S7	12°	N	17.2	13.8	2.6	56.3	53.8
		E	11.6	26.2	-41.3	72.9	114.1
		H	-54.4	19.4	-95	-13	82

5.8.3 Comparison of Space Intersection Results

There were no published works found in the literature comparing the performance of the Envisat and Radarsat satellites using a GCP-free SAR sensor model. Table 5.12 shows a summary of results obtained by *Chen and Dowman 1996* using datasets from the brief RTM mode of ERS, while Table 5.13 shows a summary of results obtained by *Chen 2000* using datasets from Radarsat, without using any ground control in both cases.

Table 5.12: *Statistics from Check Points using Space Intersection with ERS (copied from Chen and Dowman 1996)*

	Same Side 1			Same Side 2		
	E	N	H	E	N	H
Minimum (m)	-48	-91	-116	-85	-64	-103
Maximum (m)	137	93	8	72	45	28
Mean (m)	51	6	-42	4	-7	-51
Std. Dev (m)	70	35	52	37	23	64

Table 5.13: *Statistics from Check Points using Space Intersection with Radarsat (copied from Chen 2000)*

Configuration	Component	Mean(m)	Min (m)	Max (m)
Case 1 S1 – S7	E	143.9	70	277
	N	153.8	24	219
	H	53.2	20	70
Case 2 S1 – S7	E	-249.8	-304	-189
	N	-48.8	-102	23
	H	215.8	178	247

Comparison of the results from GCP-free space intersection presented in the above tables between ERS, Radarsat and Envisat shows that the superior orbit of the Envisat satellite allows it to out perform the other sensors. The results also confirm that the IESSG Space Intersection Algorithm is functioning properly and when used with Envisat imagery has the potential to generate elevations with standard deviation ranging between 6 to 14 m, depending on stereo configuration, without the use of any ground control whatsoever. However, this does not take into account the sensitivity of the algorithm to errors in the stereo matching process and this is investigated later in the thesis (see section 7.7).

5.9 A Multiple Ray Approach to Space Intersection

To date, the few space intersection procedures used in reported works have relied solely on intersecting rays from two repeat pass satellites imaging from different incident angles. The stability and accuracy of the Envisat satellite have been demonstrated in the previous section and the possibility exists that by including more intersecting rays this will increase the redundancy in the least squares solution for the space intersection thereby improving the solution.

To investigate the use of multiple rays in the space intersection process, the *IESSG Space Intersection Algorithm* was modified to allow the inclusion of observations made from a third satellite position. Since StereoSAR is restricted to same side orbits, there is a limitation on the range of intersection angles possible and therefore the number of satellites that can be added so that a suitable stereo baseline still exists. Figure 5.11 shows the new space intersection configuration that was developed in this research.

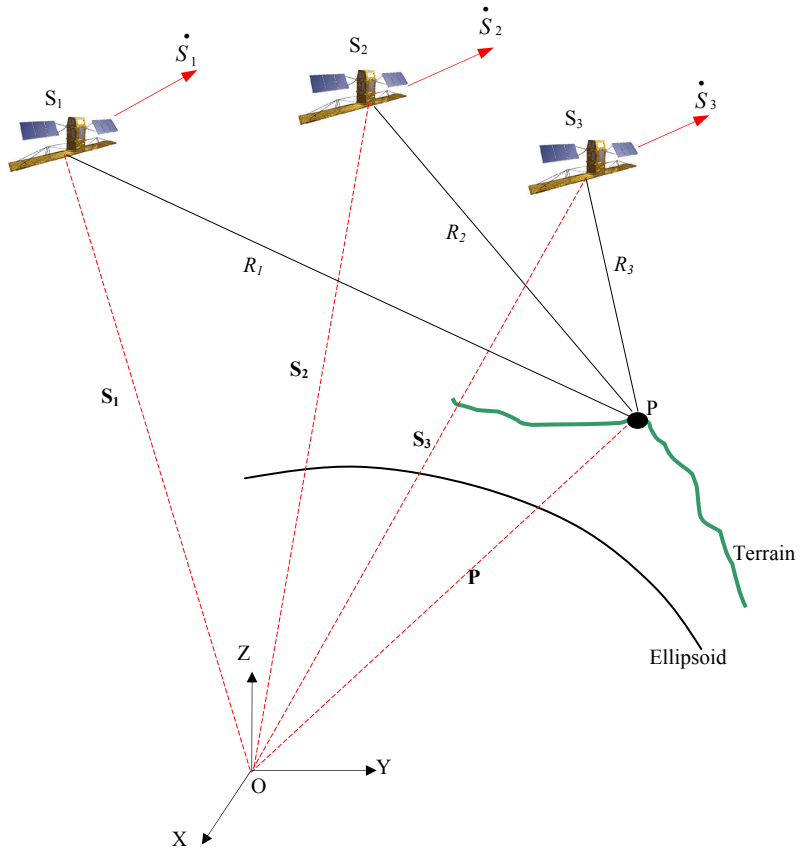

Figure 5.11: *Multi-Ray Space Intersection Approach*

The *Multi-Ray* Space Intersection Algorithm was tested using data from the Envisat IS2-IS4-IS6 and IS2-IS4-IS7 stereo configurations, since these provided the optimal spacing possible with the image triplets. The results of the *Multi-Ray* approach are shown in Table 5.14 utilizing the points from section 5.8. While this new approach showed some improvement in the elevations of the points tested, some points had to be rejected as blunders. This is because the use of multiple rays makes the algorithm more sensitive to errors in the conjugate points due in part to the reduced baseline and also the rigidity in the solution provided by the third ray. Another observation in the results was the magnification of the errors in the Northings as evidenced by the increased spread when compared with Table 5.10. An advantage of using multiple rays would therefore be the identification and removal of blunders carried over from the stereo-matching phase. What is now required is the development of a stereo matching method capable of utilizing image triplets; unfortunately time did not allow for this investigation and development in this research.

Table 5.14: *Statistics for Check Points from Multi-Ray Space Intersection Using Envisat Data*

Triplet Configuration	***Component***	***Mean***	***Std Dev***	***Min***	***Max***	***Spread***
IS2-IS4-IS6	N	3.3	43.7	-64.1	92.1	156.2
	E	-1.6	15.1	-28.8	25.1	53.9
	H	-0.2	6.6	-9	12	21
IS2-IS4-IS7	N	21.2	47.6	-44.8	89.1	133.9
	E	1.7	28.2	-34.8	49.1	83.9
	H	1.1	10.3	-13	19	32

5.10 Summary

One of the objectives of this research was to develop a GCP-free space intersection algorithm. This chapter outlined the theory and mathematical models used for such a development and presented some experimental results from testing the algorithm. Although a few authors (e.g. *Sowter 1998*; *Chen and Dowman 2001*) have used a similar intersection approach in their work, the details of the algorithm used have not been fully published and so the algorithm used in this research was developed from

first principles. One of the difficulties encountered was in identifying a larger number of points to include in the test; this goes back to the problems of determining ground control in SAR images. While it highlights topography well, it is difficult to distinguish cultural features, hence the need for an algorithm that does not rely on GCPs in formulating the sensor geometrical model. The comparison of results between Envisat and Radarsat shows that, with Envisat, for the first time it is possible to use satellite SAR stereoscopic data without the need for any GCPs whatsoever in the space intersection algorithm.

Chapter 6

The Nottingham StereoSAR Software

6.1 Introduction

StereoSAR software was developed as part of this research project for specific use with Radarsat and Envisat data, based on the DSM process flow outlined in Figure 3.9, the adaptive stereo-matching algorithm described in Chapter 4 and the space intersection algorithm presented in Chapter 5. There exist very few commercial packages capable of exploiting the full capabilities of stereoscopic SAR imagery for the extraction of topographic data. However, all require the use of GCPs - which are often difficult to identify in SAR imagery - in the formulation of a solution and the code is often not revealed making it difficult to modify specific processes. They are essentially "black box" tools. The screen shot in Figure 6.1 illustrates the interface for the application which has been appropriately named *Nottingham StereoSAR Software*. The general idea was to develop each module using the recently released C# programming language and then attach these modules as events to the related buttons shown on the interface. This chapter describes the modules developed as part of the system and demonstrates their use with the Radarsat SAR datasets described in section 7.3.

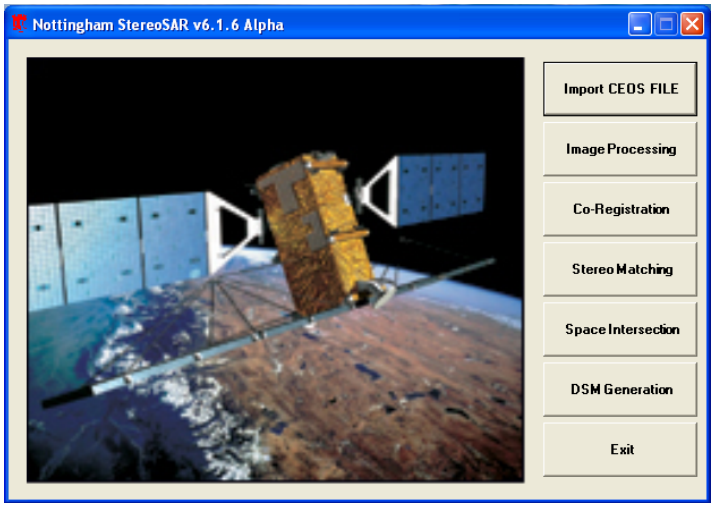

Figure 6.1: *The Nottingham StereoSAR Software interface*

6.2 Algorithms and Software Design

The Nottingham StereoSAR software system comprises of six modules, the code of each capable of being modified without affecting significantly the running of the application. This modular structure meant that development of each module could be implemented and tested independently. Also, it helps to maintain a logical structure to the system making it easy for other researchers to quickly follow the process. The use of a Windows™ based graphical user interfaces (GUI) as opposed to command line prompts or DOS™ based interfaces, has allowed increased ease of operation for first time users of the software allowing the quick recovery from invalid input of parameters from these users. This makes the *Nottingham StereoSAR Software* an ideal platform for conducting investigations into the extraction of topographic information from stereoscopic spaceborne SAR imagery. The six software modules are each described in the following sections.

6.2.1 Import Module

Data from Radarsat is usually provided in a Committee for Earth Observation Satellites (CEOS) format which is fully described in *RSI 2000*. The CDROM from the data provider Radarsat International, or other local distributors, contains five files consisting of various descriptive records. For this application the only two files of interest and to be read by the import module are: the file containing the SAR data called *dat_01.001*; and the file containing the relevant processing parameters called *lea_01.001*. Four files are created by the *Import Module* and each file has a unique extension as shown in Figure 6.2.

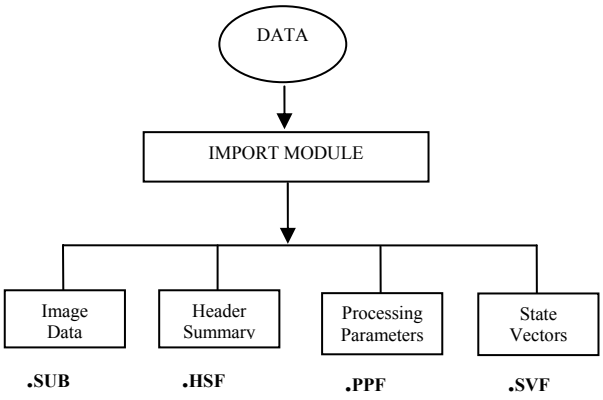

Figure 6.2: *Flow Diagram for Import Module*

The interface for this module is shown in Figure 6.3. Input data required include the location on the computer of the SAR data files for the reference and search images; the leader file containing the processing parameters for each image in the stereoscopic pair; if extracting a subset, the upper left row and column based on the reference image; and the width and height of that subset. If the *Auto Detect Search Extents* option box is checked, no information on the search extents is required; the software will use preliminary latitude and longitude in the data file to compute the search extents based on the location of the reference extents. The software is designed to clip the search extents such that it is 64 pixels larger in width and height, than the reference image subset. The user can view a summary of the processing parameters using the *View Report* button provided as shown in Figure 6.4 and selecting the appropriate file with the *.hsf* extension.

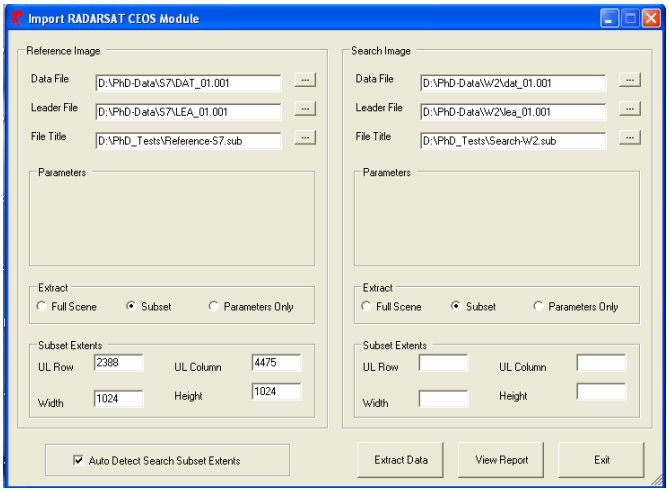

Figure 6.3: *GUI for Import Module*

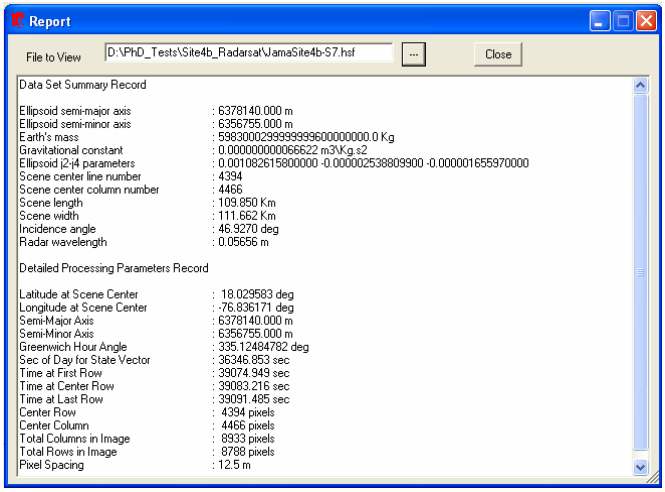

Figure 6.4: *GUI for Viewing Header Summary and State Vector Files*

Envisat data became available near the end of this research project so a specific import module was not developed for this dataset given that it was distributed in a non-CEOS format. To extract the required image data, processing parameters and state vectors, a set of tools called *Beam 3.1* available at http://www.brockmann-consult.de/beam/ were utilized. The Beam toolbox also provides Application Programming Interfaces (APIs) so that at some future date the *Nottingham StereoSAR Software* can be upgraded to allow the direct importation of Envisat ASAR data.

6.2.2 Image Pre-Processing and Enhancement Module

The term *image enhancement* refers to the manipulation of pixel values, or pixel range of values, such that the image's appearance is altered. This allows the information in the image to be readily interpreted for a particular task. This module facilitates all the necessary pre-processing and enhancement tasks required before the image matching stage. The following routines have been developed as part of this module:

- ***Linear Contrast Stretch*** – to perform a min-max stretch on the image
- ***Standard Deviation Stretch*** – performs a standard deviation stretch
- ***Sigma Nought Stretch***- technique developed to stretch image using sigma nought values
- ***Speckle Filtering*** – despeckling image using Gamma-Map, Frost , Enhanced Lee and Median filters using kernel sizes from 3x3 to 11x11
- ***Texture Mask*** – segments the reference image into areas of high texture and low texture. This mask is used as an essential part of the *Adaptive Stereo Matching* algorithm developed in this study

Figure 6.5 to Figure 6.7 show screen shots of examples of the interfaces for the various options in the *Image Processing* module.

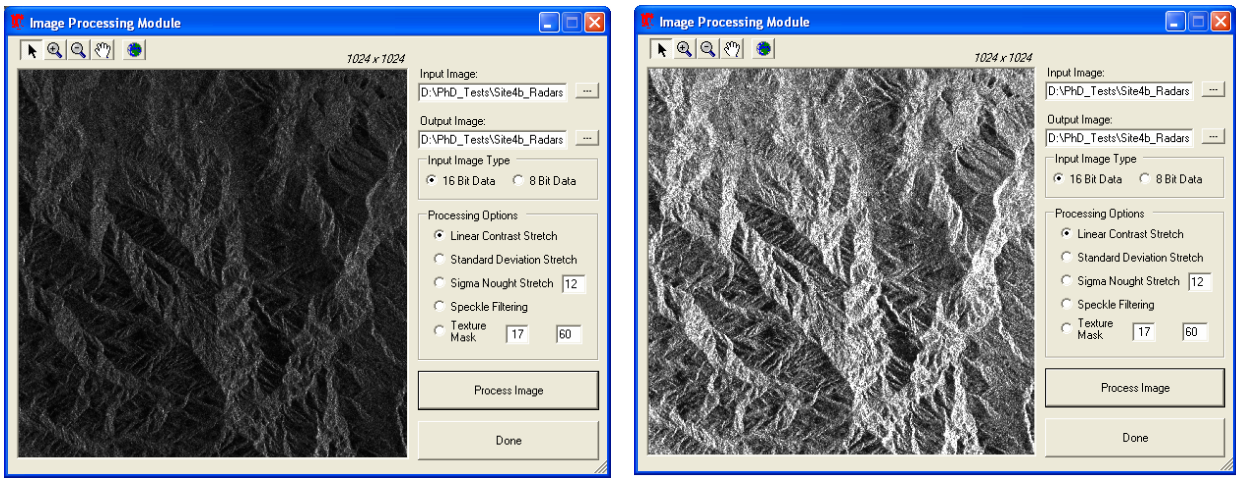

Figure 6.5: *Min-Max Linear Stretch Left: Original and Right: 480 – 28000*

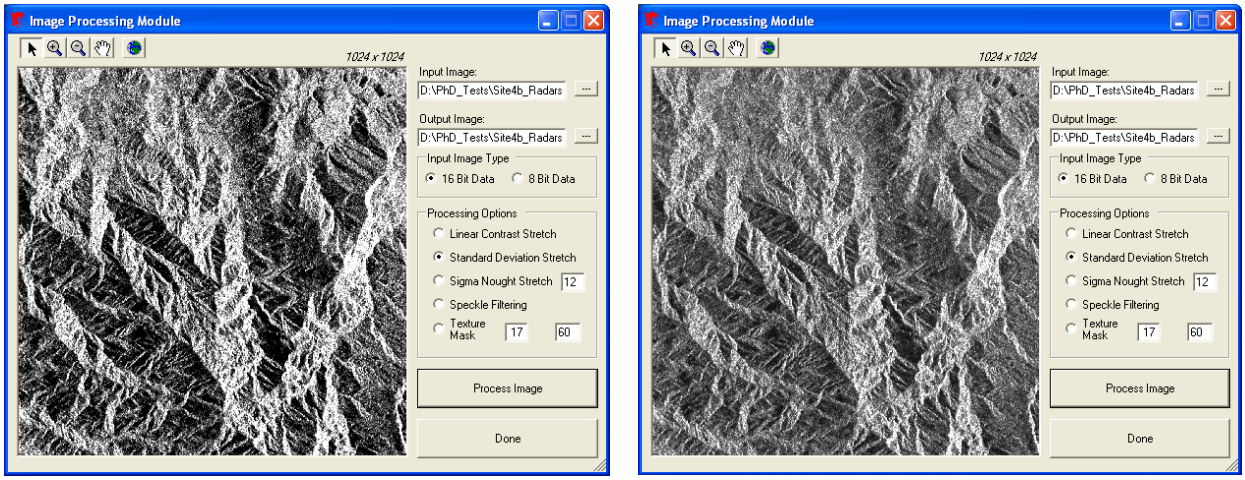

Figure 6.6: *Standard Deviation (SD) Stretch Left: 1SD and Right: 2SD*

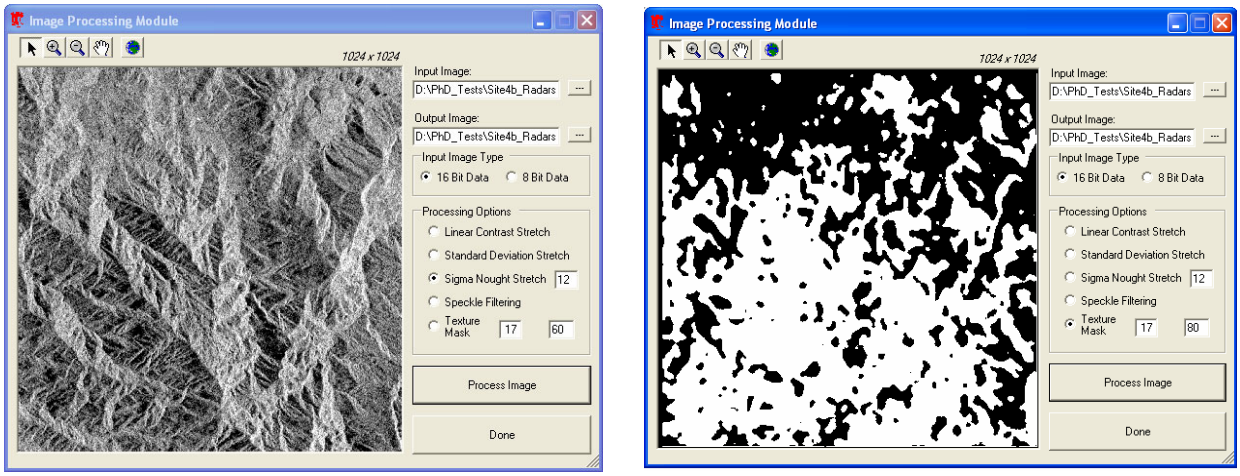

Figure 6.7: *Left: Sigma Nought Stretch and Right: Example of a Texture Mask*

6.2.3 Co-Registration Module

The main objective of the *Co-Registration Module* is to provide initial information on the registration of the reference and search images using a hierarchical approach based on image pyramids. Starting at the coarsest pyramid level, the software determines automatically the offset between the reference and search images on a pixel by pixel basis using an implementation of the area-based matcher. The points above a high correlation threshold, for example 0.9, are selected to be passed on to the next pyramid level by scaling their matched row and column positions 2 times. These scaled locations act as starting positions on the next level and the correlation repeated. Again, only points above this high threshold are selected to go to the next level. This process is repeated until the finest pyramid level is reached. Points selected on this final level (*tie-points*) are fitted with a 2^{nd} order least squares polynomial and the coefficients of the polynomial determined.

Figure 6.8 shows an example of this result with the selected points reaching the finest level represented by yellow crosses in the image co-registration display. The image coordinates and computed coefficients are also displayed. In arriving at these final points, the image co-registration GUI gives the user the options to change starting pyramid level, template sizes, search areas and correlation thresholds. This affords a lot of flexibility for conducting investigations when assessing the performance of the co-registration.

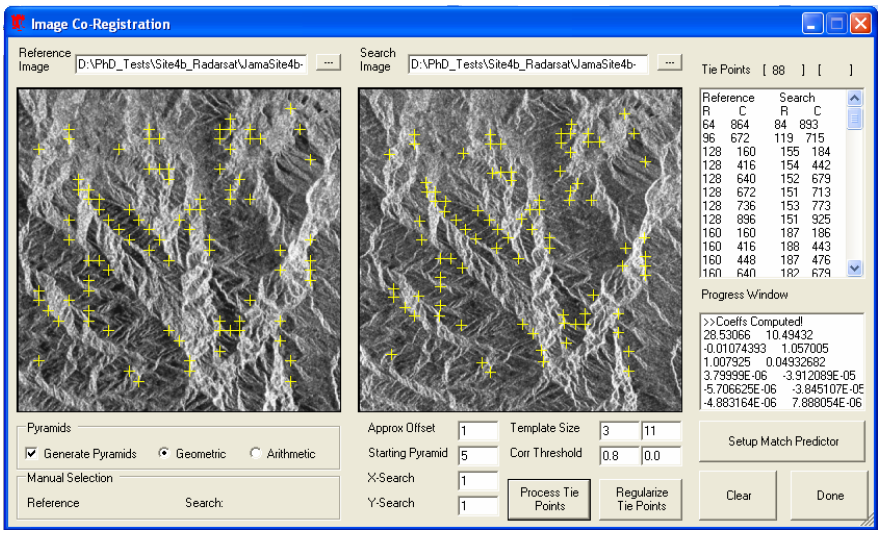

Figure 6.8: *Image Co-Registration GUI Showing Output from the Preliminary Registration*

The automatically generated tie-points may not necessarily cover the entire image area due mainly to the starting template size. To overcome this and increase the number of possible tie-points on the finest level, the polynomial coefficients computed previously were used to predict the location in the search image of every 25th pixel from the reference image. At these predicted locations the area-based matching algorithm, using a high threshold coefficient, attempted to locate the point. A new set of polynomial coefficients are computed from these dense set of tie-points based on this final automatic image co-registration as shown in Figure 6.9.

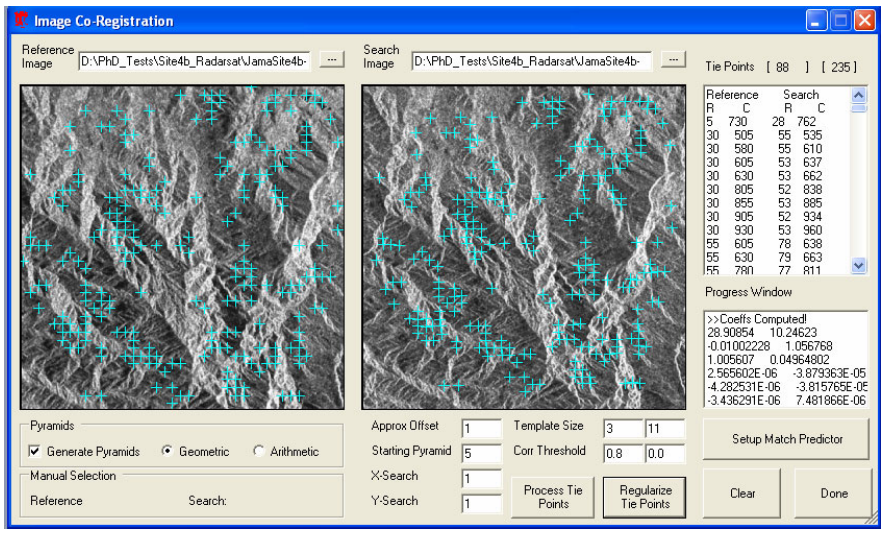

Figure 6.9: *Output from the Final Automatic Registration*

These new set of coefficients are then used to compute for the search image the predicted location of every pixel from the reference image and a matrix containing the shifts in row and column (Δr, Δc) between these two images generated. This matrix forms the basis of the co-registration elements and describes the relative orientation between the reference and search image. To reduce the effects of geometric distortion on these elements, the matrix is scaled by a factor of 2 to generate coarse levels similar to the image pyramid concept and the same number of levels as the pyramids generated for the matching process. This would certainly ensure consistency with the hierarchical approach adopted during the stereo matching phase.

6.2.4 Stereo Matching Module

This module and its interface were designed to allow easy interaction with any level of user. The algorithm is based on the Adaptive Matching Strategy that was outlined in section 4.6. The interface for this module is illustrated in Figure 6.10. The required inputs include:

- Reference image
- Search Image
- Values for the 6 strategy parameters (default values usually pre-set)
- Texture mask

while the primary output is the parallax file containing the image coordinates of the conjugate points and the reference image greyscale value at the matched location. A progress window allows the user to track the activities and determine the time taken for a particular aspect in the stereo matching process.

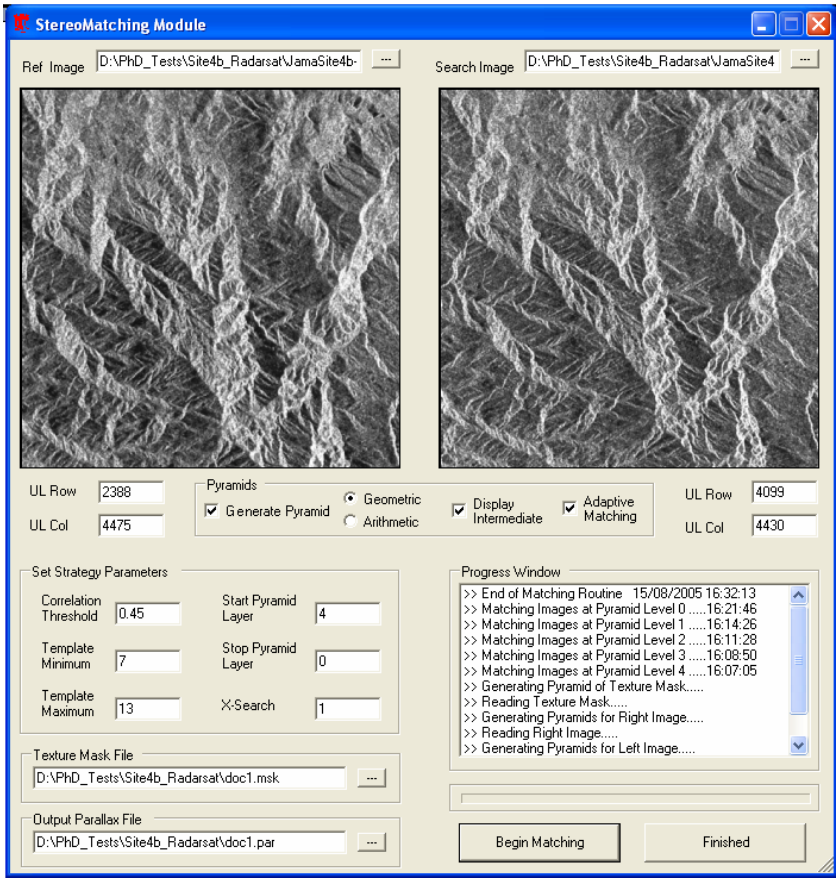

Figure 6.10: *GUI for Stereo Matching Module*

Unlike other StereoSAR applications, for example the add-on option for ERDAS, this software allows the user the flexibility to view the results of each pyramidal level during the hierarchical processing. The advantage of this feature is that it allows experimentation with various values for the strategy parameters and the user does not have to wait until the entire matching process is completed to see the effect of varying a particular parameter. Figure 6.11 gives an example of the output at pyramid level 4.

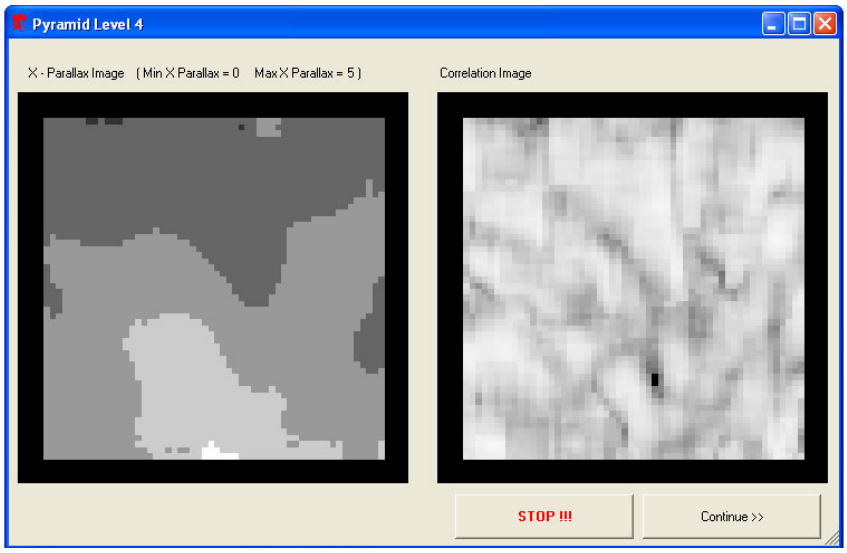

Figure 6.11: *Example Output of Matching Results on Pyramid level 4*

This GUI shows two images, the parallax image on the left and the correlation image on the right. In this example, the correlation threshold was set to 0.45 so in the correlation image all values below the threshold are shown as black while values above are shown in shades of grey tending towards white as the correlation goes to 1. In the parallax image, failed areas are filled in with a linear interpolation and filtered with both a majority and median filter. The importance of this image is not only to provide an output picture, but to let the user/investigator see how well the interpolation and filters are working.

This window provides a useful tool for researchers so that for the first time it is possible to investigate a set of optimized parameters not only as a basis of the final DSM, but more importantly, consideration for the influence at the intermediate levels

can be taken into account in arriving at a set of parameters that are capable of adapting at each pyramid level if necessary. If the user/investigator is satisfied with the choice of strategy parameters at this pyramid level the process is allowed to continue to the next level as shown in Figure 6.12 and the other level illustrated in Figure 6.13. Otherwise, the process is stopped, the choice of strategy parameters amended and the process restarted.

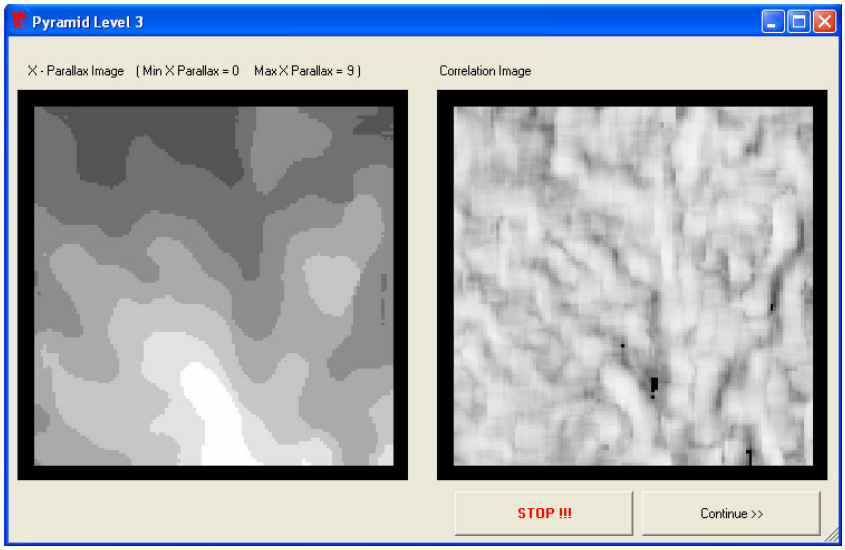

Figure 6.12: *Example Output of Matching Results on Pyramid level 3*

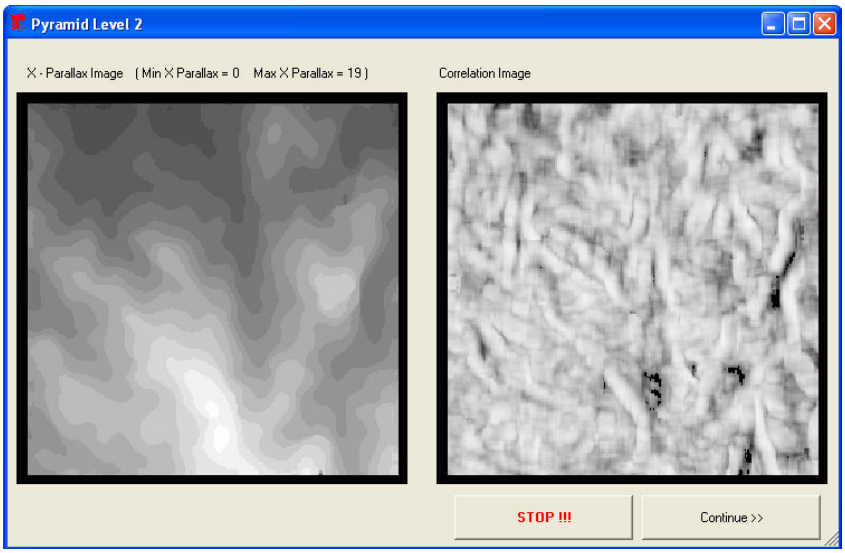

Figure 6.13: *Example Output of Matching Results on Pyramid level 2*

By pyramid level 1, the details of the topography are well highlighted in the parallax image as shown in Figure 6.14. As evident in the correlation image, more failed areas tend to occur as the finer pyramid levels are attained. This is due mainly to the geometric distortions causing dissimilarity between the images and this is most significant on the last level or the original image as seen in Figure 6.15. It is here that the real value of the interpolation and filters are derived by ensuring that there are few data voids as possible in the parallax image.

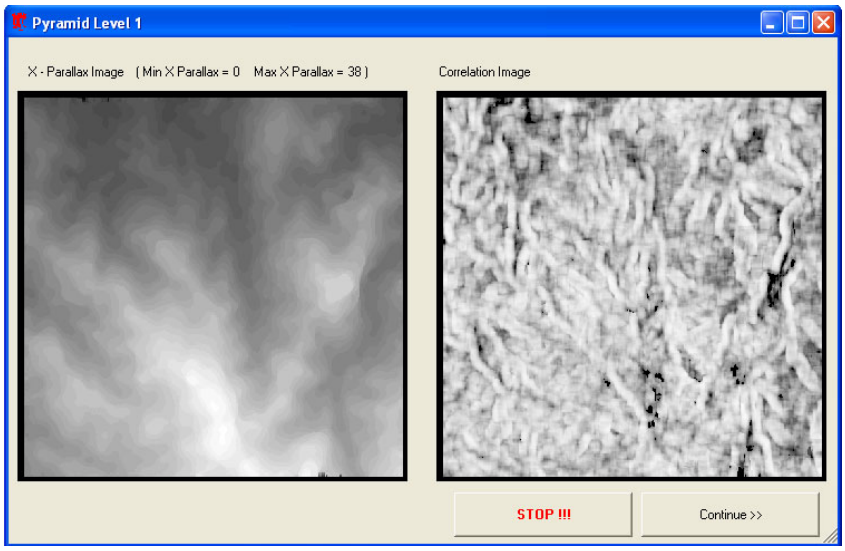

Figure 6.14: *Example Output of Matching Results on Pyramid level 1*

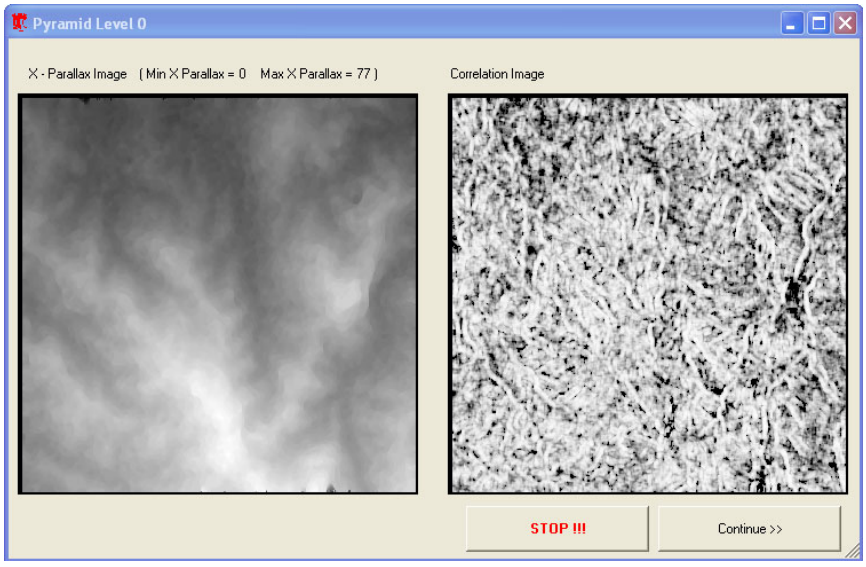

Figure 6.15: *Example Output of Matching Results on Pyramid level 0*

The user is provided with the option to turn off the intermediate display once the optimized parameters are selected. The entire stereo matching process takes between 15 – 30 minutes for a 1024x1024 image subset depending on the values set for the strategy parameters, especially the X-Search parameter. At the end of the stereo matching process the list of image coordinates for the conjugate points are written to a binary file with extension ***.par***.

6.2.5 Space Intersection Module

The sole objective of this module is to take the image space coordinates of the conjugate points and project them into object space coordinates in an appropriate mapping system. The mathematical models and algorithms developed in chapter 5 are used in this module. Figure 6.16 shows the GUI for the space intersection module and the primary inputs are: the orbit information and processing parameters for the reference and search image; the name and location of the parallax file; the orbit determination method; the orbit direction (ascending or descending); and the map projection, which in this research is limited to the global UTM and the local projection of the study area.

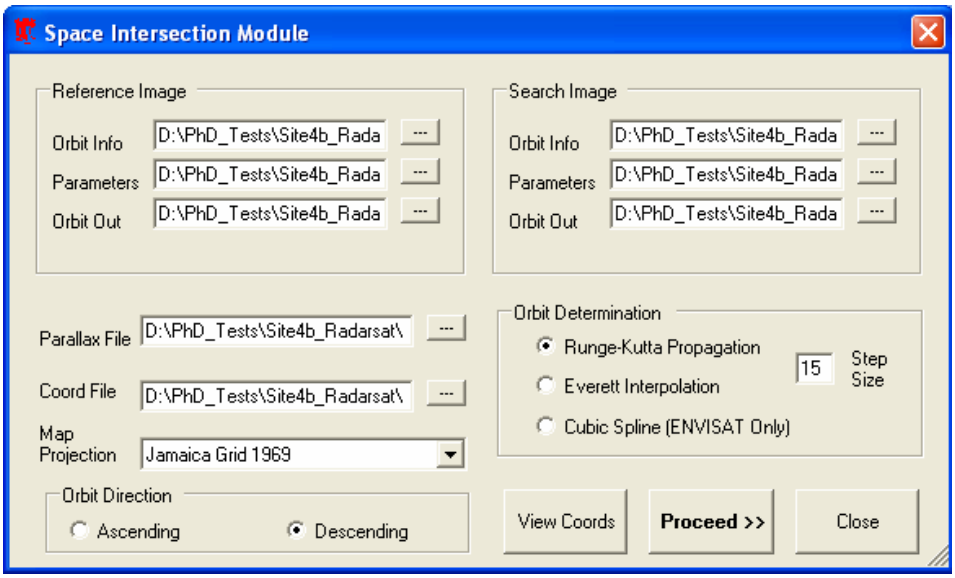

Figure 6.16: *GUI for the Space Intersection Module*

The main outputs from the space intersection are a binary and ASCII point cloud file containing the E, N, H and greyscale value for each matched location. The binary file with extension **.bin** is used in the DSM generation module, while the ASCII file with extension **.asc** was created to allow the user the flexibility of inspecting the un-gridded points in a GIS software of their choice. All output units are in metres.

6.2.6 DSM Generation Module

Most spatial analysis in a GIS would require the data is in some raster format, mainly grid based, which makes it easy and efficient to implement cell based manipulation. The objective of the DSM generation module is to resample the point cloud generated in the space intersection module into a user specified grid size thereby resulting in a raster grid DSM. The algorithm used here follow the steps outlined previously in section 3.4.3.6 and Figure 6.17 shows an example of the output from the process.

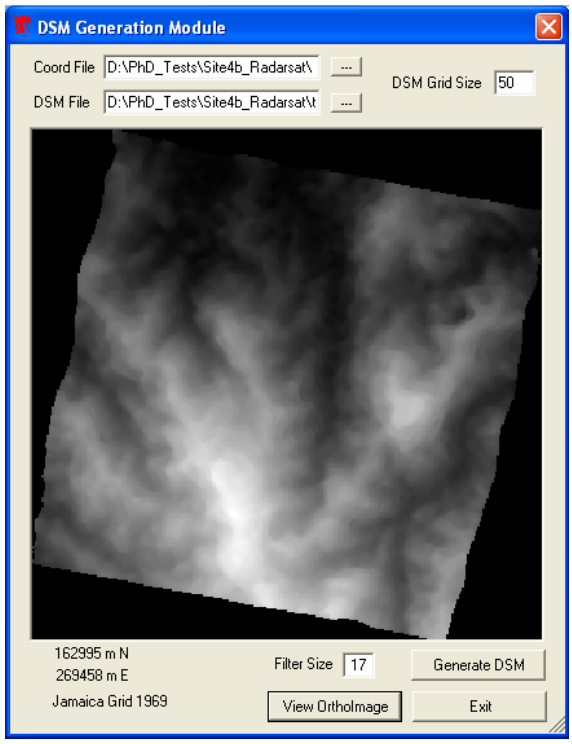

Figure 6.17: Example of an *Automatically Generated StereoSAR DSM*

The inputs into the module are the name and location of the binary coordinate file, and the size (posting) for the required DSM grid. The output is the grid DSM file with a **.bil** extension which can be readily displayed in ERDAS Imagine or ESRI ArcGIS without any further formatting. It takes less than 15 seconds to resample the DSM from the point cloud for a site 1024x1024 pixels using a desktop Pentium 4 computer.

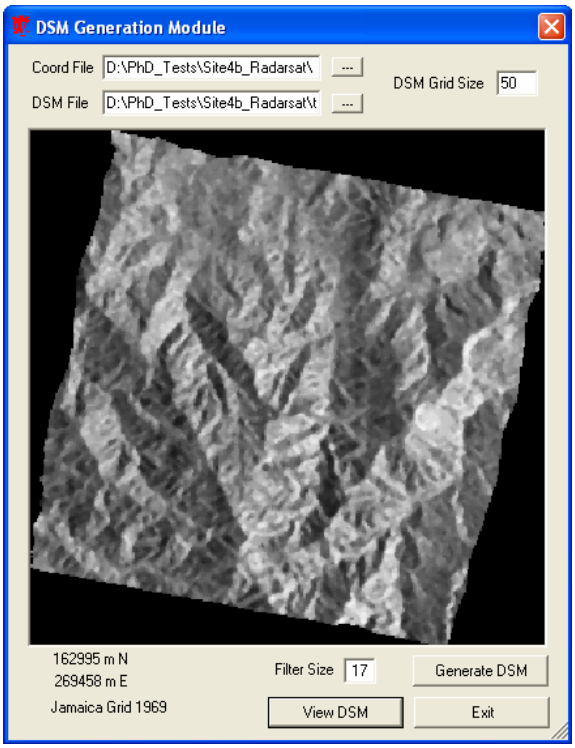

Figure 6.18: *An Automatically Generated SAR Ortho-Image*

As mentioned in section 3.4.3.7, a technique was implemented to simultaneously geocode the SAR image while generating the DSM using the procedure described in that section in an extremely fast and efficient manner. No further input is required from the user and all is that is required is to press the *view orthoimage* button on the GUI and straight away the ortho-image appears. Figure 6.18 illustrates an example of the type of ortho-image capable from the system. At this stage the two main products from the Nottingham StereoSAR System, the DSM and ortho-image, have been achieved.

6.3 Software Testing and Validation

As with any computer software, an important stage in the development cycle is the process of checking whether the modules are integrated properly and performing their required tasks correctly and efficiently. Three strategies were used in validating the StereoSAR system. In the first case, intermediate results were outputted to the screen and compared with manual computations. Secondly, the debugging utility in MS visual studio .Net – the programming environment used for this project – was employed to view the values of variables during the execution of the programs to ensure that the correct values were being read and the correct intermediate results passed on to other modules. Thirdly, the program was applied in a controlled situation where there can only be one outcome. An example of this was in the validation of the stereo matching algorithm. The same image was used as both the reference and search image therefore from this configuration it was expected that the parallax image should be all zeros and the correlation image should be all ones for all output at each pyramid level. This was in fact the case when tested.

The software was also used by both undergraduate (BEng) and masters (MSc) students for conducting their SAR related projects. Although these students were not SAR experts, they were able to use the program with minimal guidance and there were no reports of the StereoSAR system crashing at any stage of their work. The author is fairly confident that the software is robust enough for a low-cost system for use over cloud affected developing countries such as the Caribbean.

6.4 Summary

The *Nottingham StereoSAR system* was presented in this chapter. The function of each module was examined and some typical outputs demonstrated. Tests conducted to the system show it to be operating within acceptable parameters given the limitation of the images that it employs. The design of the system is modular which would make it easy for any advancement or modification to be made in the future. The fact that it is driven mainly by GUI's makes it easy for almost any level of user to perform topographic extraction with minimal guidance. In the next part of the

thesis, the performance of the system will be critically assessed. Since no GCPs are required, the system makes real ‘remote sensing’ applications possible.

Chapter 7

Application over a Tropical Region

7.1 Introduction

Knowledge of topography forms an essential part of any Geographical Information System (GIS) and central to many spatial modelling activities; the geo-referencing of earth observation imagery; and the visualization of landscapes. Tropical regions, comprising of many developing countries, are usually affected by persistent cloud cover problems making it difficult and sometimes costly to apply optical or laser-based techniques for the generation of topographic information at the national level.

In this research project, a prototype system capable of extracting low-cost topographic information over cloud affected developing countries situated in tropical regions has been developed. This system incorporates a stereo matching algorithm that adapts the key strategy parameters based on a texture mask generated over the area of interest; details presented in chapter 4. The system also incorporated another algorithm, developed from fundamentals principles, to transform the parallaxes created in the stereo-matching phase to a local map projection and height datum without using any knowledge of ground control points (GCPs) whatsoever. This was described in chapter 5 where results on its performance were also presented. The integration of these algorithms, along with other key components, to form the *Nottingham StereoSAR System* was presented in chapter 6 which also illustrated how the system works and the typical outputs that can be generated .

This chapter demonstrates the application of the system over cloud affected developing countries, to test and critically assess its performance for generating StereoSAR DSMs of these tropical regions. The study area and datasets used are first described followed by the validation of the reference DSM being used to assess the quality of the StereoSAR DSM developed here. Next, the methodology adopted for the DSM generation using the *Nottingham StereoSAR System* is outlined and finally useful discussions are presented.

7.2 Description of Study Area

The requirement is to generate a stereo-derived DSM over a tropical region, in this case, part of the Caribbean island of Jamaica (Figure 7.1), using the *Nottingham StereoSAR System*. This site is a mountainous island of 10,991 km^2 with its tallest peak, the Blue Mountains in the east, rising to 2,256m. The island is situated at 77^0 W and 18^0 N and is the third largest of some twenty-five islands in the Caribbean Sea forming the West Indies. Jamaica has been chosen because it best represents the surface characteristics that dominate the Caribbean landscape with its varying land use types and topographical features (Figure 7.2). It is the only island with a dataset capable of validating the results of this study. Recent attempts (*Edwards 2002*) to generate a DSM over the island using ERS tandem interferometry failed due to the low coherence over the hilly and vegetated areas (see Figure 3.5). This site, therefore, provides an excellent opportunity to test the capabilities of our StereoSAR algorithms as a complementary approach for the extraction of low-cost topographical information from spaceborne SAR imagery over cloud affected developing territories.

Figure 7.1: *Map of the Caribbean Region Showing the Location of Jamaica. The Study Area is to the North East Covering 13.5 km x 13.5 km and is Depicted in the Inset (base map © Islandbride.com)*

Figure 7.2: *Terrestrial photos showing examples of Jamaica's landscape (© E. P. Edwards)*

7.3 Description of Datasets

For testing the StereoSAR system developed in this research, the SAR data used were acquired from both Radarsat and the new Envisat sensors since these are the only sensors available to date capable of producing stereoscopic pairs from multiple incidence angles. The next two sections describe these stereoscopic datasets.

7.3.1 Radarsat SAR Images

Radarsat satellite images required for this research have been acquired over the study area. Two *standard mode* (S1 and S7) images and one *wide mode* (W2) image were collected. These acquisitions were planned using the *Radarsat Swath Planner* software, kindly donated by Radarsat International, which determined the next possible imaging date and time; this information was passed on to Radarsat for use in programming the satellite. Figure 7.3 shows the interface for the swath planning software used in this research. Full explanations on using the software can be found in *RSI 1998*. Table 7.1 details the characteristics of these images.

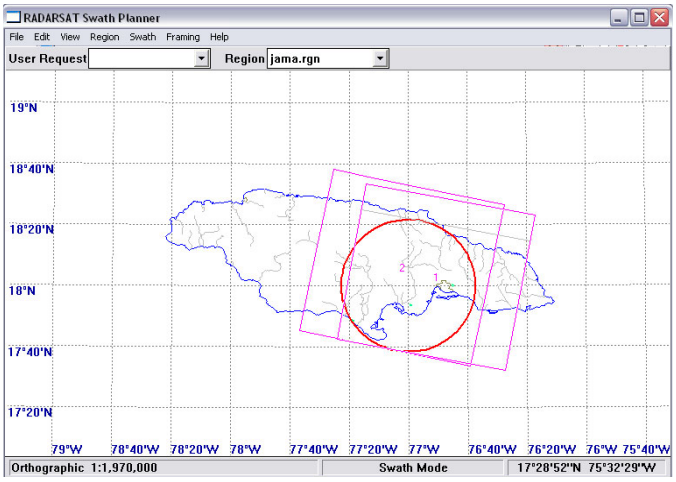

Figure 7.3: *Screen shot showing the planned position of overlapping image pairs S1 & S7 (magenta) for the area of interest (red).*

Table 7.1: *Characteristics of RADARSAT images*

	Image 1	Image 2	Image 3
Scene Date	22-Mar-02	26-Mar-02	23-May-02
Scene Time (GMT)	11:07:47	10:51:14	10:59:21
Beam Mode	Standard 1	Standard 7	Wide 2
Scene Size (pixels)	9489x9091	8788x8933	12606x10958
Pixel Spacing (m)	12.5	12.5	12.5
Incidence Angle (deg)	23.5	47	35
Number of Looks	4	4	4

7.3.2 ENVISAT ASAR Images

Five Envisat ASAR datasets were acquired using the image mode for beam positions IS2, IS3, IS4, IS5, IS6 and IS7 with HH polarization in the C-band of the electromagnetic spectrum. These beam positions were chosen to provide a suitable range of incidence angles for testing the space intersection algorithms developed in section 5.7 while allowing the formation of appropriate stereo pairs with minimal layover and enough similarity between images for the automatic stereo matching.

The planning of Envisat acquisitions was conducted using the Display Earth remote sensing Swath Coverage Window (DESCW) software tool from ESA available at *http://earth.esa.int/descw*. DESCW allows the user to search an online database for archived imagery or plan a new acquisition. For this research project a file containing the acquisition parameters was generated using DESCW and sent to ESA for programming the satellite for the next available acquisition slot. Figure 7.4 shows an example of a planning session using DESCW, while Table 7.2 summarises the characteristics of the acquired SAR images.

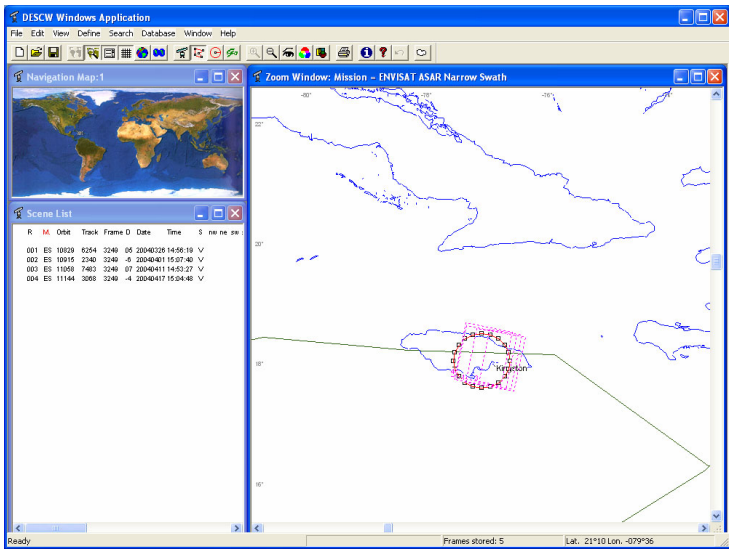

Figure 7.4: *Screen shot showing planned location of ENVISAT ASAR scenes (magenta)*

Table 7.2: *Characteristics of ENVISAT ASAR images*

	Image 1	Image 2	Image 3	Image 4	Image 5
Scene Date	01-Apr-04	22-May-04	25-Oct-04	26-Mar-04	11-Apr-04
Scene Time (GMT)	15:07:49	15:05:01	15:02:14	14:56:30	14:53:36
Image Swath	IS 2	IS 3	IS 4	IS 6	IS 7
Scene Size (pixels)	8411 x 8547	8726 x 6640	8696 x 7004	8570 x 5737	8624 x 4587
Pixel Spacing (m)	12.5	12.5	12.5	12.5	12.5
Incidence Angle (deg)	23	29	34	41	44
Number of Looks	4	4	4	4	4

7.3.3 Topographical Maps

Topographical maps, published by the Jamaica Survey Department, the national mapping agency, were scanned and geo-referenced to the local mapping frame by the Jamaica Forestry Department and made available for this project. The maps were at a scale of 1:50 000 and have not been updated since the 1980s. Due to lack of financial resources, the Survey Department does not have any plans to update these maps anytime soon. For this project these maps provide a means of qualitatively assessing the StereoSAR DSM and for providing GCPs for validating the space intersection algorithm. Figure 7.5 shows a topographical map extract over the study area.

Figure 7.5: *Topographical Map of Study Area at 1:50,000 Scale*
(© The Jamaica Survey Department)

7.3.4 Digital Contour Data

Contours digitized from the 1:50 000 scale topographic maps were available for the study area from the Jamaica Forestry Department in a GIS ready format (i.e. ESRI shapefile). These digital contours were used in the research to overlay on top of the StereoSAR DSM and conduct qualitative analysis on the generated DSM. Figure 7.6 shows a subset of the contours covering the study area.

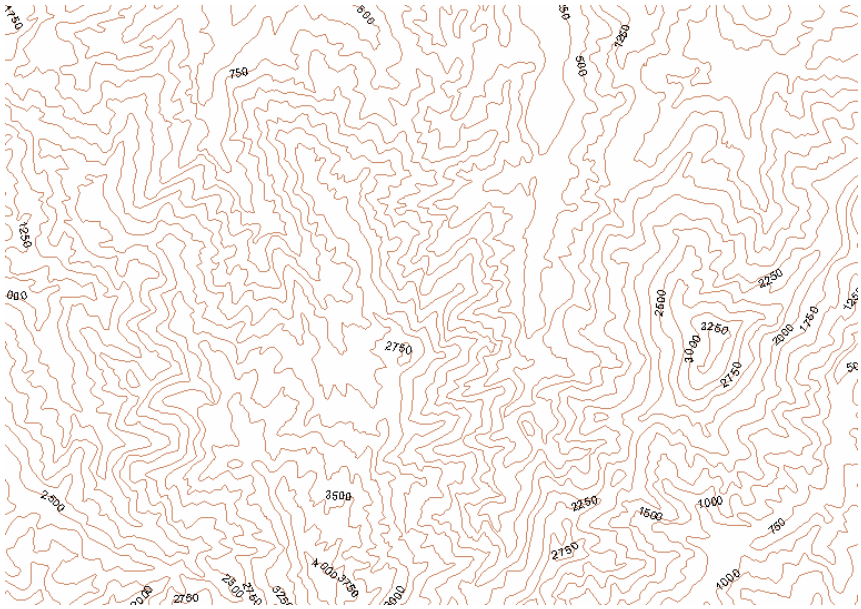

Figure 7.6: *Example of Digital Contours Covering Study Area*

7.3.5 Reference DSM

To conduct an evaluation of the potential of the Nottingham StereoSAR System for generating topographic information at the national level, it is necessary to compare the DSM product from the system with a product of higher quality and generate the statistical measures presented in section 3.5. Analysis of these statistical measures would lead to information about the quality of the StereoSAR DSM and its suitability for national topographic mapping. Therefore the quality of the reference DSM is quite critical.

Until now, the assessment of SAR DSM products have been conducted by comparing them with DEMs generated using contours derived from photogrammetric methods (see for example, *Premalatha 2001*; *Ka and Kim 2001*; *Chen 2000*; *Toutin 2000*; and *Sowter 1998*). Photogrammetry and SAR are two differing technologies operating in different parts of the electromagnetic spectrum and may make observations to different first surfaces in the landscape. The contours derived from the photogrammetric method are often time influenced by the subjectivity and experience of the operator and the interpolation methods used to generate the resulting reference DEM add more uncertainty to the quality of that dataset (*Smith et al. 2005*).

This research was fortunate to benefit from the availability of a high resolution single-pass airborne InSAR DSM generated from data observed during March/April 2002. The InSAR mission was carried out using an AeS-1 airborne system by the German company Aerosensing on behalf of Space Imaging. The AeS-1 is a full interferometric SAR system using two X-band radar antennas separated by a base length of 2.51m. A detailed description of the system and data processing chain can be found in *Wimmer et al. 1999*. The DSM product is generated with *Type III* specification, i.e. grid spacing of 5m and accuracy of 3m – 5m depending on the slope of the terrain (*www.intermap.com*). Elevations are given with reference to the EGM96 geoid and the horizontal datum used is WGS84. The final DSM is projected to the local Jamaican Grid system. For the first time it was possible to compare StereoSAR DSM with a reference surface generated using a related technique. Figure 7.5 shows a sample of the colour coded InSAR DSM for the test site used in this research project.

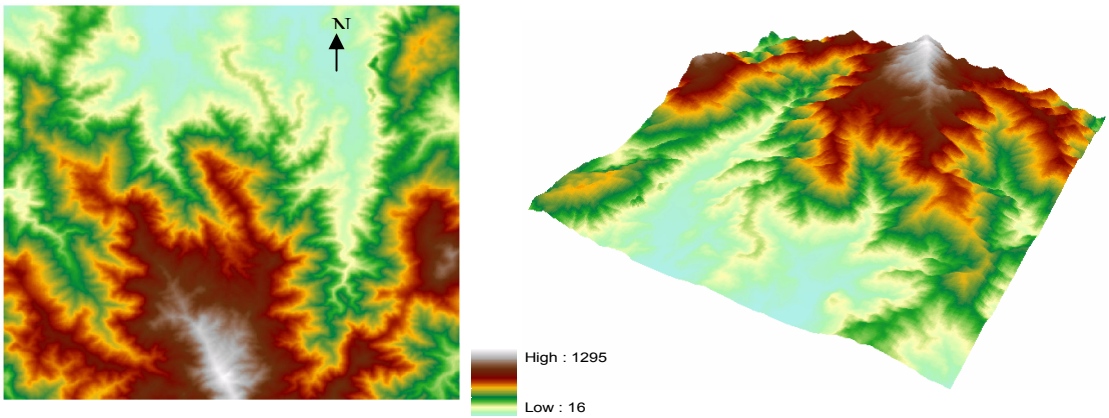

Figure 7.7: *Airborne InSAR DSM of Study Area. Left: Plan View; Right: Perspective View from NW*

7.4 Validation of the Reference DSM

The validation of any surface model requires the identification and use of other higher accuracy elevation data usually referred to as the 'ground truth' dataset or *reference DSM*. Having identified and acquired this 'ground truth' it is crucial to ascertain whether this reference surface is:

1. Better in both vertical and horizontal positional accuracy
2. Identical in geo-location projection
3. Identical in vertical datum
4. Identical in elevation model posting spacing in the case of higher order grid elevation data

To investigate and validate the quality of the InSAR reference DSM, Differential GPS (DGPS) techniques were adopted using a Trimble GeoExplorer 3 GPS roving receiver with an external antenna attached and a Trimble 5700 receiver as the base station. Mapping quality receivers like the GeoExplorer 3, are capable of determining horizontal positions with accuracy of ±1m and vertical positions with accuracy ± 1-3m if the observations are differentially corrected. These estimates are consistent with the findings in previous work conducted by this author using similar equipment - Garmin GPS receivers (see *Edwards 1994*). Sub-meter accuracy can be achieved by smoothing the code with the carrier signal, but this requires the collection of at least 10 minutes of data (*Trimble 2001*) which is not usually ideal when using the kinematic mode.

The GeoExplorer GPS unit was installed in a vehicle platform and configured for the kinematic mode of observation. The base receiver was mounted at a known WGS84/JAD69 station at the head quarters of Spatial Innovision Limited. The system was first tested over the National GPS Calibration Baseline (NGCB) located at the Heroes Circle Park in Jamaica to verify its accuracy in the kinematic mode. With the antenna mounted on the roof, the vehicle was positioned such that the NGCB point of interest was vertically below the antenna as shown in Figure 7.8 and more than 200 kinematic positions recorded at 1 sec interval.

Figure 7.8: *Calibration of GeoExplorer3 GPS Unit Integrated with Vehicle Platform*

The observations were differentially corrected using the base station data and the computed values compared with the known coordinates of the NGCB station. The results showing the differences are illustrated in Figure 7.9 and the summary of statistics for the vertical component is shown in Table 7.3.

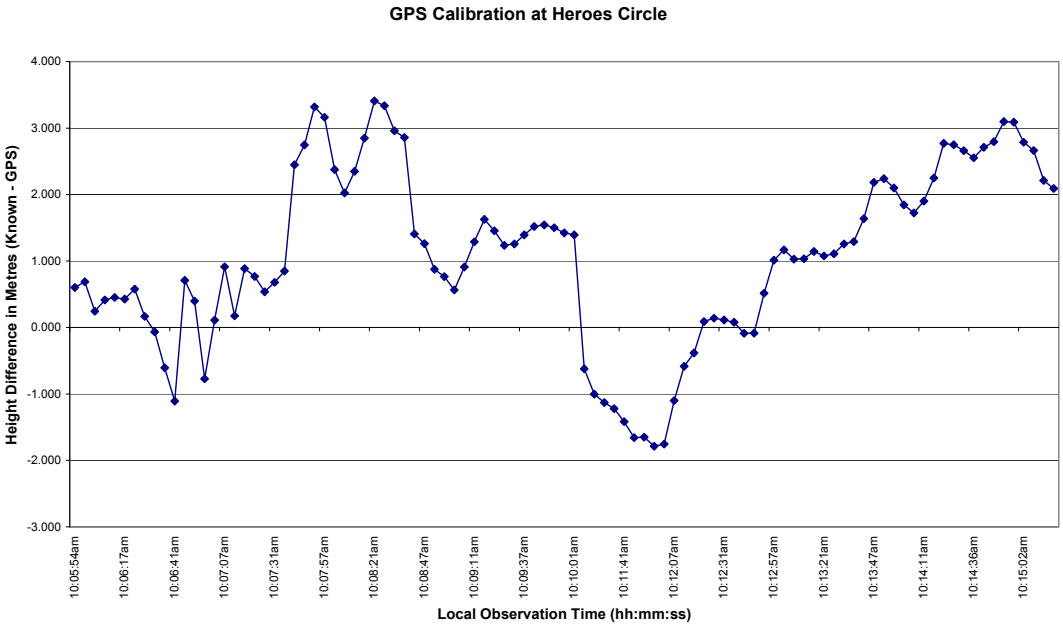

Figure 7.9: *Height Differences between NGCB Station and GeoExplorer Kinematic Positions*

Table 7.3: *Summary of Statistics for Vertical Differences between NGCB Station and GeoExplorer3*

# of samples	Mean (m)	Std. Dev (m)	RMSE (m)	Min (m)	Max(m)
215	1.1	0.96	2.1	-1.8	3.4

The statistics show that there is a systematic bias of ~ 1m existing after differential corrections and this may be due to the difference between the multipath scenarios at the base and roving stations; the GeoExplorer's external antenna is mounted on the vehicle's metallic surface and the base station has an ideal environment for recording GPS observations. Nevertheless, the RMSE which takes into account this bias is within the expected accuracy for the InSAR surface and will be useful in validating that reference surface. If the bias can be mitigated though, the positioning quality of the GeoExplorer receiver would improve to ~ 1m as indicated by the standard deviation.

The validated GeoExplorer 3 onboard the vehicle platform was used to acquire transects across the landscape for comparison with the InSAR reference DSM in an attempt to verify its quality. Foliage and the lack of accessibility over the study area prevented a direct validation of this site. However, the assumption was made that if the same InSAR technique was used for all areas then validating an accessible site in close proximity to the study with similar terrain characteristics would be useful in revealing the quality of the reference DSM.

Figure 7.10 shows an example of one of these transects superimposed on a subset of the 1:50,000 topographical map of the same area. The plan positions of the processed DGPS points compared well with the map sheet indicating no significant horizontal datum defects in the projected DGPS points. To assess the vertical datum component, the InSAR elevations at the location of the DGPS points were extracted using ESRI ArcGIS 9.0 and a profile showing the comparison of both InSAR and GPS was derived along the transect from South to North. This result is illustrated in Figure 7.11.

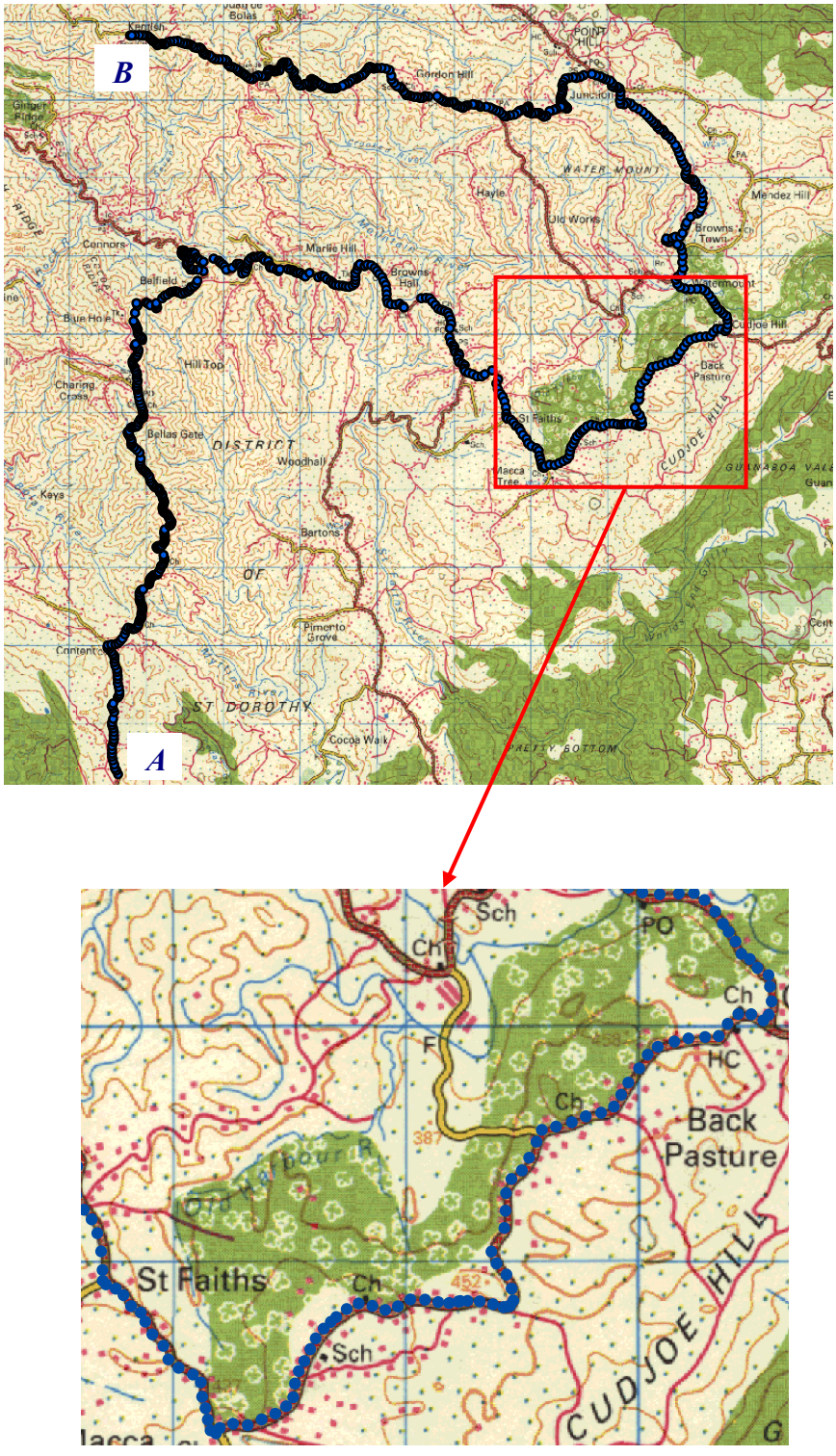

Figure 7.10: *GPS Transect Superimposed on 1:50 000 Topographical Map of Same Area (Base Maps © The Jamaica Survey Department)*

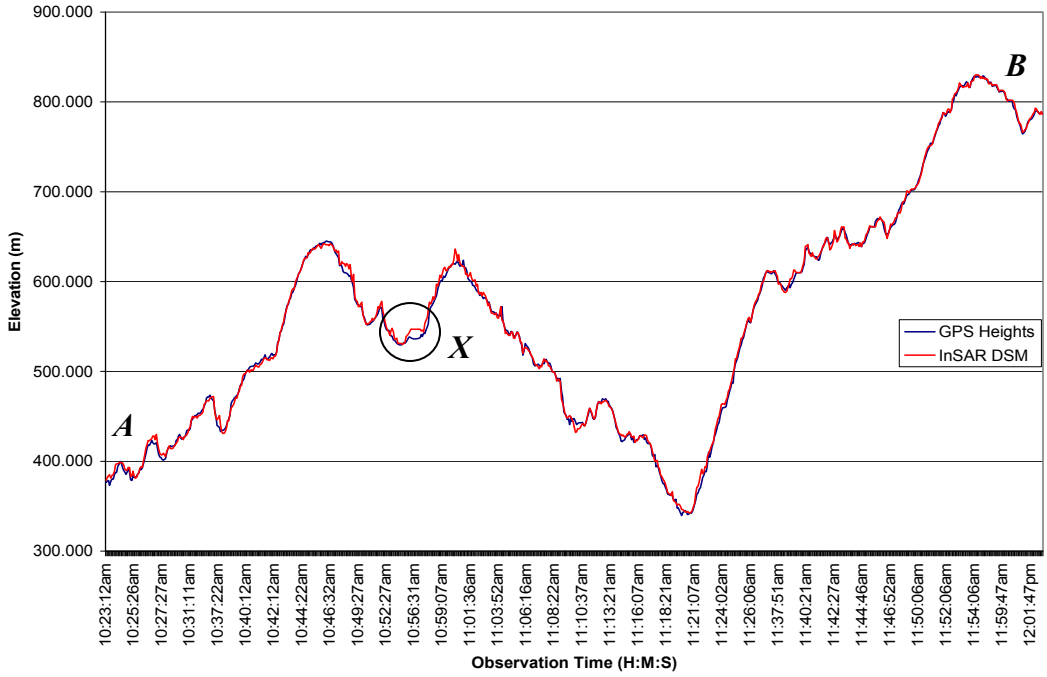

Figure 7.11: *Profile Comparing the Elevations Derived from DGPS with the Reference DSM*

The DGPS heights compare extremely well for the fore slopes as well as for the back slopes. There are a few areas with discrepancies approaching the 10m mark, an example is labelled ***X*** in Figure 7.11; this can be expected since some of these areas have canopy overhanging the roadway travelled which will be recorded as the first surface for InSAR and at times create problems for the GPS solution. Generally, the comparison is very good. An inspection of the profile from ***A***-***B*** does not indicate any systematic shifts in positions or heights which would suggest that the reference DSM is well registered in the local map projection and vertical datum and therefore suitable for use as a reference surface in critically assessing the StereoSAR DSM.

Having established the quality of the reference DSM, the comparison process will require the subtraction of the StereoSAR DSM from the 'ground truth' data. In the case of grid data, the grid subtraction will be valid for the ground areas that are modeled by both grids. In the case of high accuracy point data, such as DGPS points, the subtraction will be valid for each discrete point. In the next section, the strategy used in this research to generate the StereoSAR DSM is described in detail before proceeding to the comparison of the surfaces.

7.5 DSM Generation Strategy

An efficient strategy for extracting topographic information from spaceborne imagery will comprise of a number of steps arranged so as to produce optimized products. The software used for DSM generation is that developed as the *Nottingham StereoSAR System* during this research, using the process flow outlined in Figure 3.9 and the algorithms described in chapter 4 and chapter 5. The operation of the software was already illustrated in chapter 6.

In this section, the steps used for the DSM generation strategy are described, and illustrations are made in appropriate places using the datasets presented in section 7.3. From the available spaceborne SAR images, subsets for three stereo pairs were selected over the study area and included one from Radarsat (S7-W2) and two from Envisat (IS7-IS4 and IS6-IS4). The stereo pairs were selected such that the effects of layover and foreshortening in the steep terrain were not excessive and that there were enough similarities between the image pairs to allow the automatic stereo matching to occur.

7.5.1 Image Extraction

The summary of characteristics for the Radarsat and Envisat images used in this research was presented previously in Table 7.1 and Table 7.2 respectively. The first step in the generation of a StereoSAR DSM is to decide on the location and extents of the area of interest; then select the most suitable stereo pairs that are capable of generating topographic information; finally, extract the subsets for the area and process the images. A useful tool for supporting the selection of study areas or test sites is an *anaglyph.* It is an economical means of visualizing the landscape since the product, once it is created, does not require any expensive specialist viewing equipment or software. An anaglyph was created for this project area (see Figure 7.14) using the Envisat IS3 and IS7 datasets and the ERDAS Imagine 8.7 software. The anaglyph shows the study area selected for DSM generation and can be viewed with the red/blue glasses provided at the back of this thesis. As can be seen, the anaglyph is 100% cloud free and reveals useful 3D visual topographic information of a part of Jamaica's landscape.

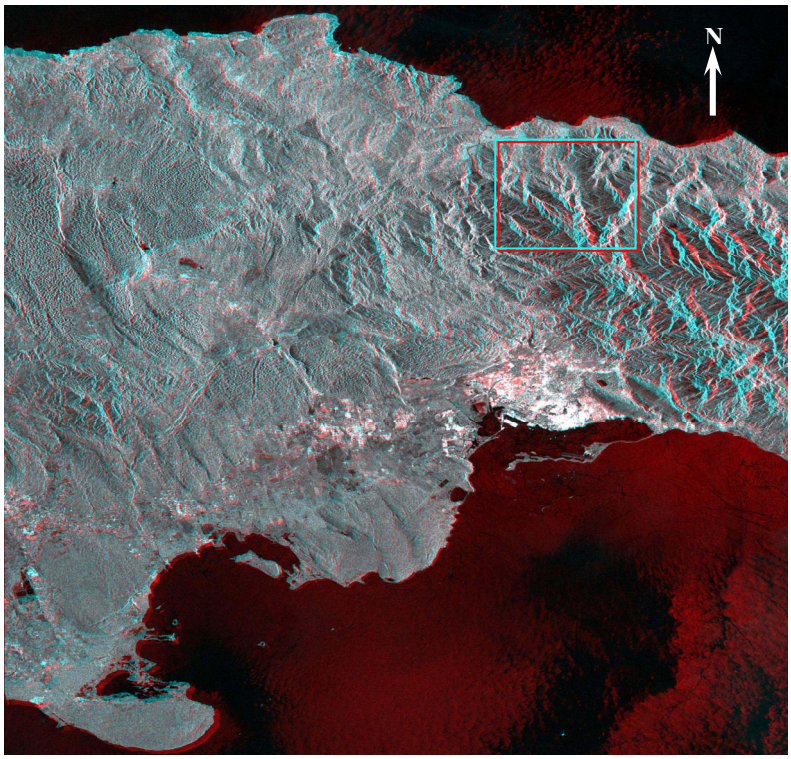

Figure 7.12: *Envisat Anaglyph Showing Study Area (requires red/blue glasses provided)*

The extraction of the subsets over the study area is accomplished using the Nottingham StereoSAR *Import Module* in the case of Radarsat and the *Beam 3.1* toolkit in the case of Envisat once the parameters defining the top left corner of the reference image and the dimensions in pixels for the study area have been determined. The extraction proceeds as described in section 6.2.1. When extracted, the subsets are in 16 bits and cannot be displayed in the StereoSAR system which is geared towards 8 bits. Figure 7.12 and Figure 7.13 show the subsets extracted.

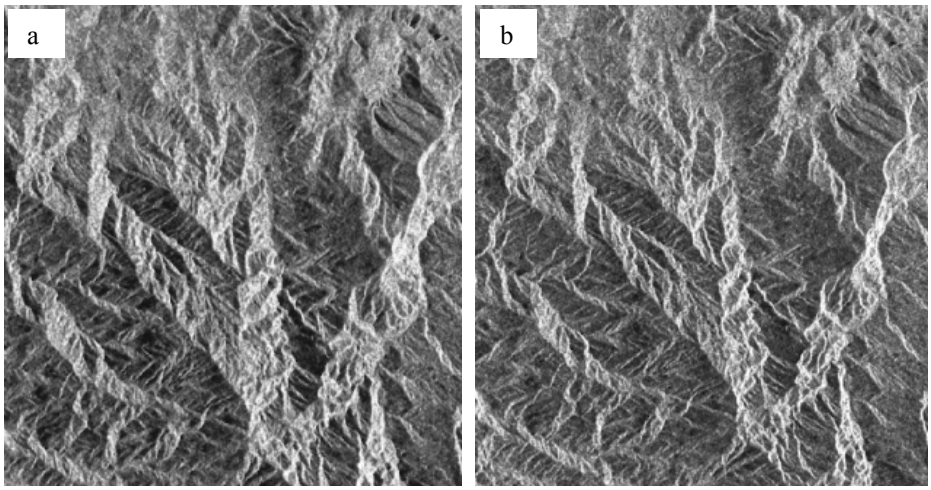

Figure 7.13: *Image Subsets Used to Form the Radarsat Stereo Pair. (a) S 7 (1024x1024 pixels); and (b) W 2 (1088x1088 pixels)*

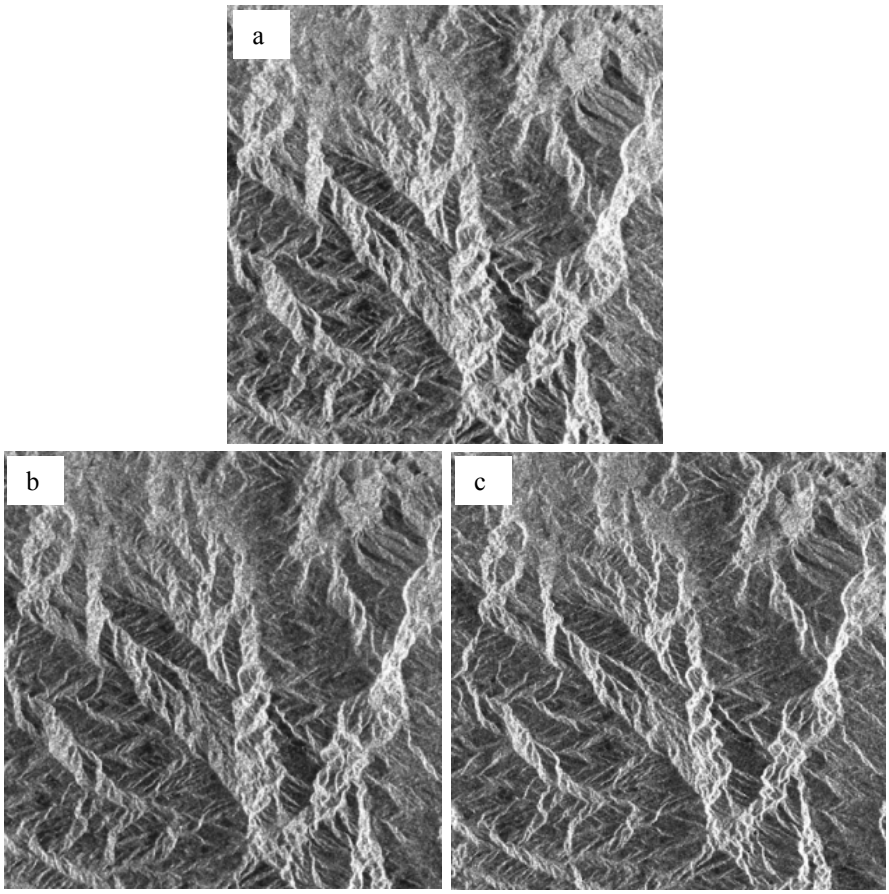

Figure 7.14: *Image Subsets Used to Form the Envisat Stereo Pairs.*
(a) IS 7 (1024x1024 pixels); (b) IS 6 (1024x1024 pixels); and (c) IS 4 (1088x1088 pixels)

7.5.2 Image Pre-Processing

Most viewing systems can only display 8 bit data and since visual inspection of the images at various stages of the process is critical for making decisions about parameter selection and settings in this research based software, it was decided to stretch the images from 16bits to 8bits. This would also reduce by half the size of the data the StereoSAR system would have to handle and would be more appropriate for a fast low-cost system. For the purposes of reporting, the results of all stretch options will not be presented. Instead, the Radarsat S7 image mode will be used to demonstrate the image pre-processing techniques applied.

7.5.2.1 Image Stretch

To stretch the images from 16bits to 8 bits three options are provided in the StereoSAR system: Linear Contrast Stretch; Standard Deviation Stretch; and the newly developed Sigma Nought Stretch. Examples of the image stretches performed are presented in Figure 7.15 in relation to the S7 subset. All other image stretching was done in a similar manner using the *Image Processing Module* of the Nottingham StereoSAR System as illustrated in section 6.2.2.

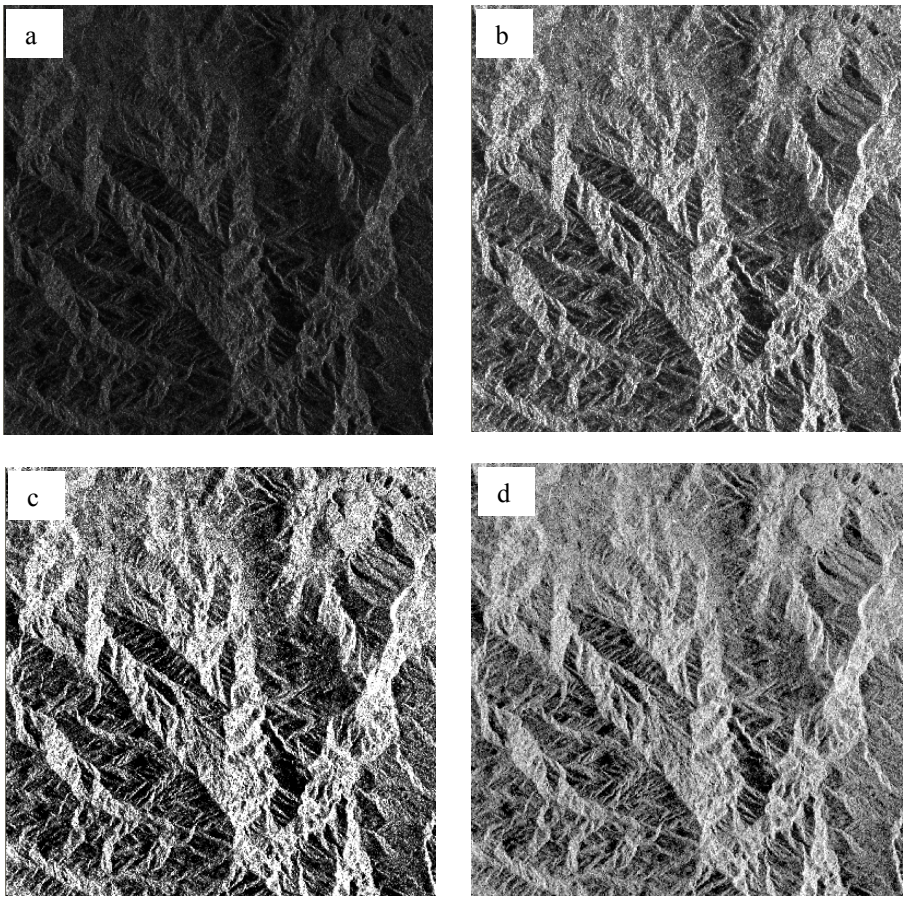

***Figure 7.15**: Examples of Image Stretch on Radarsat S7: (a) Linear Contrast Stretch 480-65535; (b) Linear Contrast Stretch 480-22000; (c) Standard Deviation Stretch-1SD; and (d) The Newly Developed Sigma Nought Stretch.*

7.5.2.2 Speckle Filtering

The usefulness of SAR data over cloud affected areas has already been shown, but the speckle noise which corrupts the data makes it difficult to conduct stereo matching. To improve the matching process, it is necessary to try to remove the speckle noise while at the same time retaining texture and edges that will be useful in the stereo matching process. Conflicting views in the literature, as to whether or not to speckle filter, has prompted an investigation in this research to determine the influence of speckle filtering on the DSMs. As noted in section 2.8.3, studies by *Paudayal and Aschbacher 1993* revealed the Gamma MAP is best for preserving linear and edge features during filtering while similar studies conducted by *Shi and Fung 1994* indicated that the Frost filter was more appropriate for this purpose. In this step both the Gamma MAP and the Frost speckle filters were used to generate filtered images so as to ascertain which one, if any, is more appropriate for use in the StereoSAR system. Figure 7.16 and Figure 7.17 illustrate the effects of these filters.

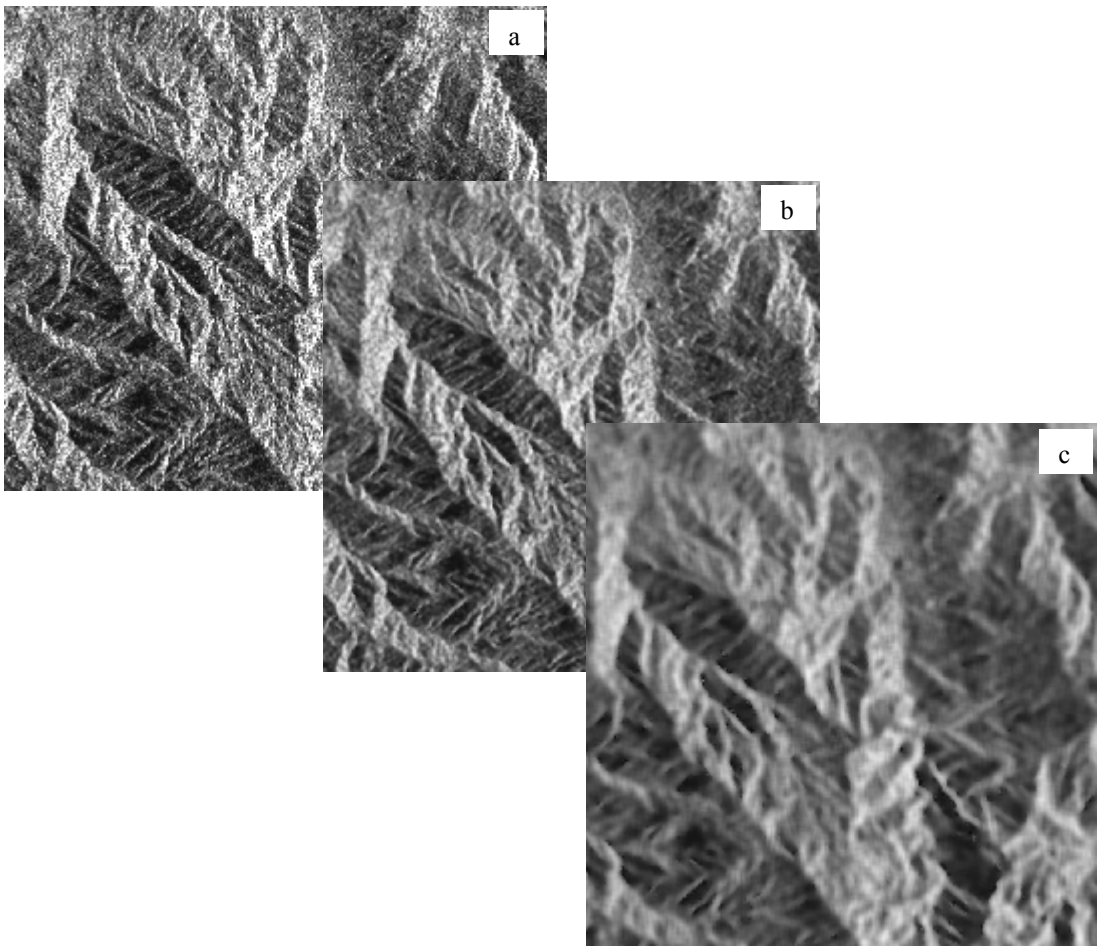

Figure 7.16: *Speckle Filtering using Gamma Map: (a) Original; (b) 5x5 Kernel; (c) 11x11 Kernel*

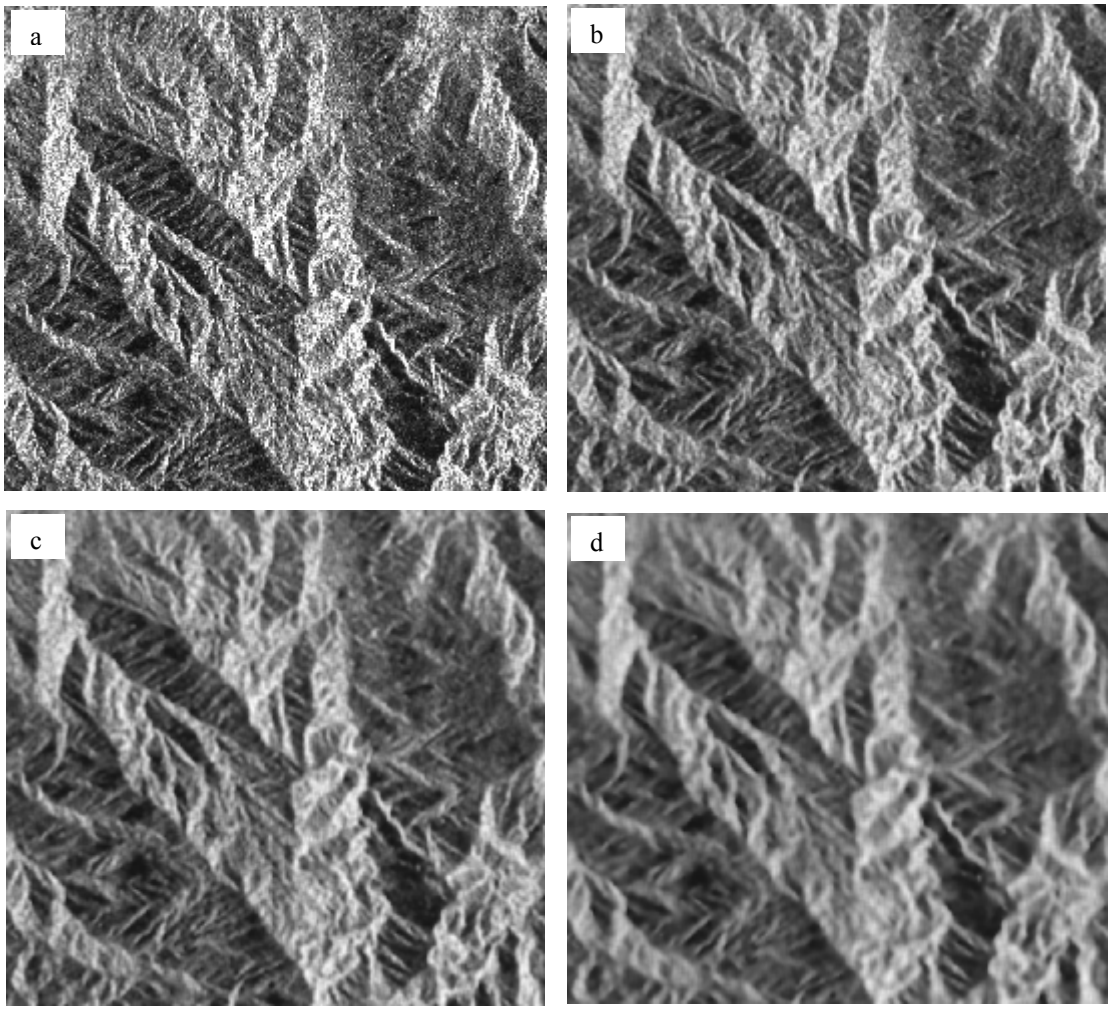

Figure 7.17: *Speckle Filtering using Frost: (a) Original; (b) 5x5 Kernel; (c)7x7 kernel; and (d) 11x11 Kernel*

7.5.2.3 Texture Mask

Previous researchers have conducted stereo matching experiments using fixed strategy parameters for the entire surface extraction process. In this research, a different approach was implemented. The strategy parameters used to control the matching is made to adapt based on the level of texture in the image. This adaptive stereo matching algorithm, described in section 4.5, required the use of a *texture mask* as noted earlier. In deriving this texture mask, the user is required to set the values for two parameters: processing template size; and greyscale threshold value.

There was no direct method for determining values for these parameters in this research so a series of experiments were conducted to arrive at a set of optimized values for these parameters. Examples of texture masks generated from the spaceborne SAR images used in this research, applying these optimized values, are illustrated in Figure 7.18 along with the respective optimized values listed. It is important to note here that the texture mask must be generated from the unfiltered image and not the speckle filtered image since the texture mask algorithm already has a speckle removal component built in (see section 4.5.1). Also, the mask is generated for the reference image only. In this research those images would be Radarsat S7 and Envisat IS6 and IS7.

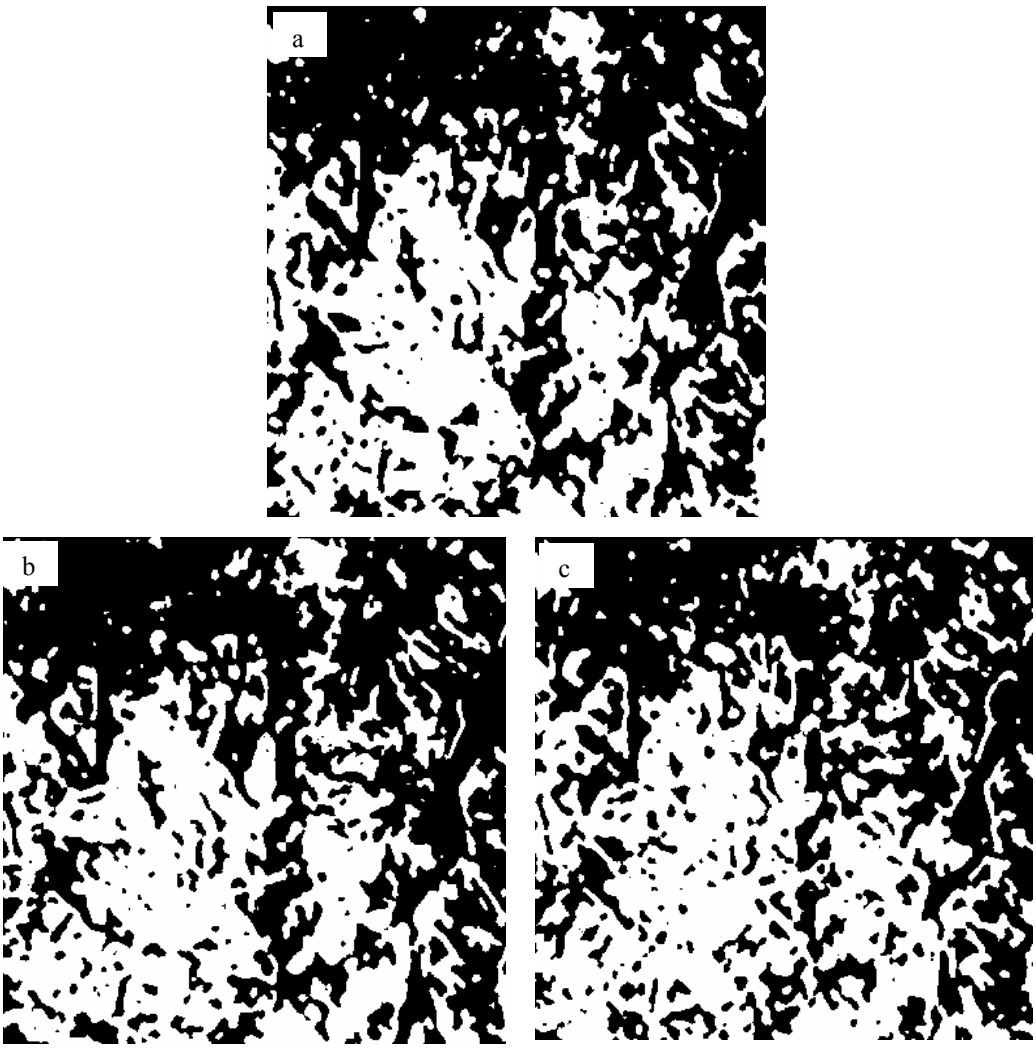

Figure 7.18: *Texture masks Generated for (a) Radarsat S7 Template=15, Threshold=80; (b) Envisat IS6 Template=15, Threshold = 70; and (c) Envisat IS7 Template=15, Threshold=70*

7.5.3 Co-Registration of Images

One of the most fundamental questions in StereoSAR is "*where should the matcher begin?*" Several authors have approached this problem in different ways, some of which were mentioned in section 4.4. In this research, ancillary data from the image header files were used to determine the preliminary relationship between image pairs using a hierarchical procedure, as described in section 6.2.3, to automatically determine a set of polynomial coefficients and by extension the approximate shifts between each pixel in the reference and search images that can be applied at each level of the image pyramid during stereo matching. This coarse registration of the images helps to reduce the search space and speeds up the matching process.

The *Image Co-registration Module* was used to accomplish this step of the processing chain. Several parameters are required to be set by the user and again after experimentation the optimized values are shown in the screen shots below. It was noted in the experiments that when using unfiltered images the correlation threshold parameter has to be relaxed to a lower value than would be used for filtered images, otherwise less than the minimum of four tie-points are detected. This is mainly due to the speckle noise in the un-filtered image pair. Figure 7.19 illustrates the output for the co-registration of an un-filtered stereo pair while Figure 7.20 shows the output from a filtered pair using a Gamma Map 5x5 speckle filter. The output shows that filtering the image pair increases the number of tie-points generated by ~ 500 %.

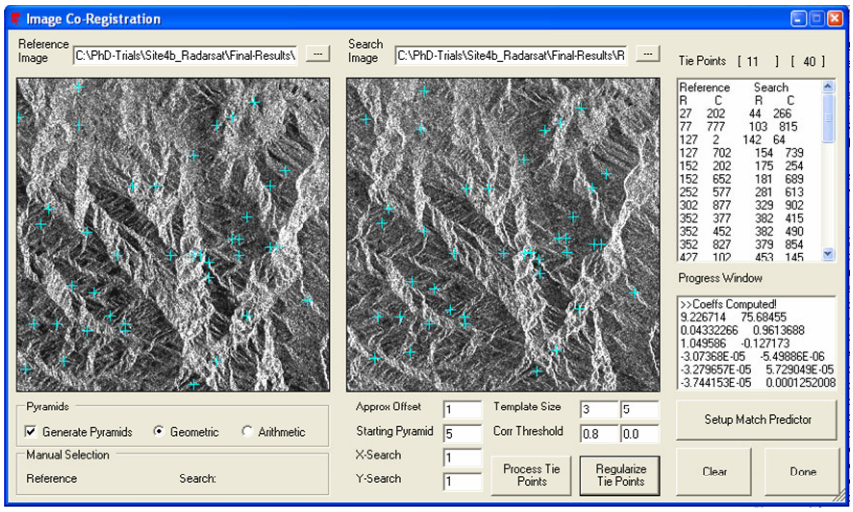

Figure 7.19: *Final Automatic Co-Registration Example for Un-Filtered Radarsat S7-W2 Pair*

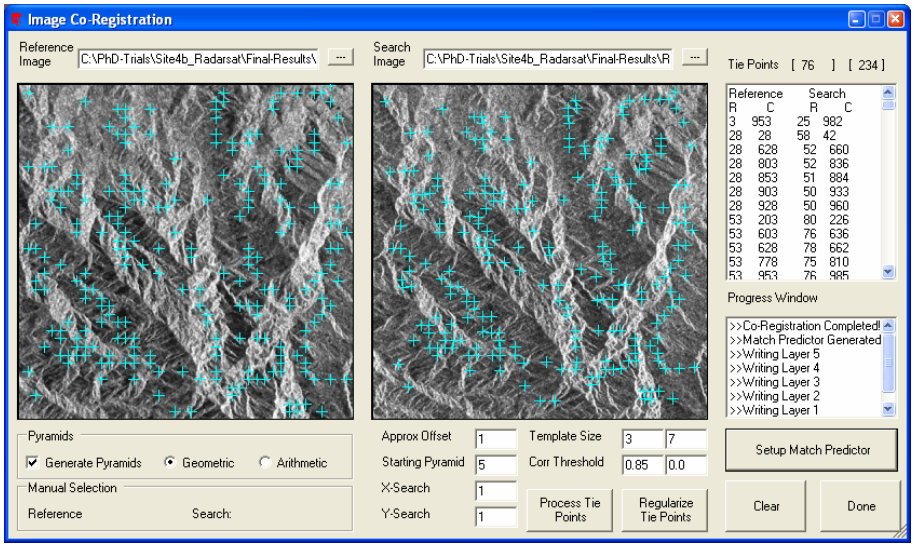

Figure 7.20: *Final Automatic Co-Registration for Gamma Map Filtered Radarsat S7-W2 Pair*

7.5.4 Digital Stereo Matching

This software is newly developed so optimized strategy parameters would not be available. Before conducting stereo matching it was important to determine the most suitable values that should be assigned to the strategy parameters controlling the *StereoMatching Module*. Among these parameters, the size of the matching windows (templates), the correlation threshold and the x-search distance are thought to be quite critical. According to *Kanade and Okutomi 1994*, the selection of an appropriate window size in stereo matching is a central problem; the window must be large enough to include enough intensity variations yet small enough to avoid the effects of distortion. Small windows that do not cover enough grey values give poor disparity estimates because of the low signal-to-noise ratio.

To identify optimal values for the strategy parameters, several experiments were conducted. To facilitate these experiments a special computer program, using sections of the stereo matching code, was created to match individual conjugate points based on image coordinates manually selected by an observer using *ERDAS Imagine* software.

The manually extracted image coordinates were used to perform supervised matching at pre-determined locations. A total of six pairs of conjugate points were manually measured, three in high textured areas (*PT#1 – PT#3*) and three in low textured areas (*PT#4 – PT#6)*. The main objective of these experiments was to provide knowledge as to the behaviour of the matching software when using different window sizes and also to show the correlation values changed in high textured and low textured areas. The experiments were conducted for filtered and un-filtered images and the results are presented in Figure 7.21 and Figure 7.22 respectively.

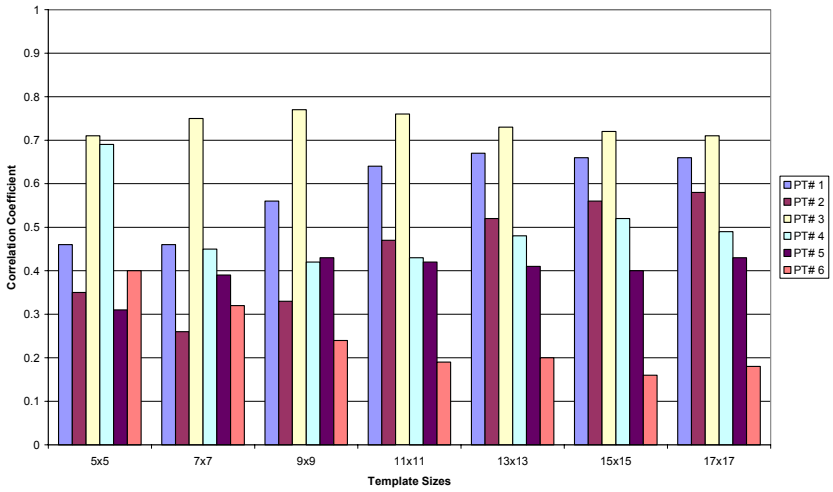

Figure 7.21: *Stereo Matching Experiments Using Un-Filtered Stereo Pair*

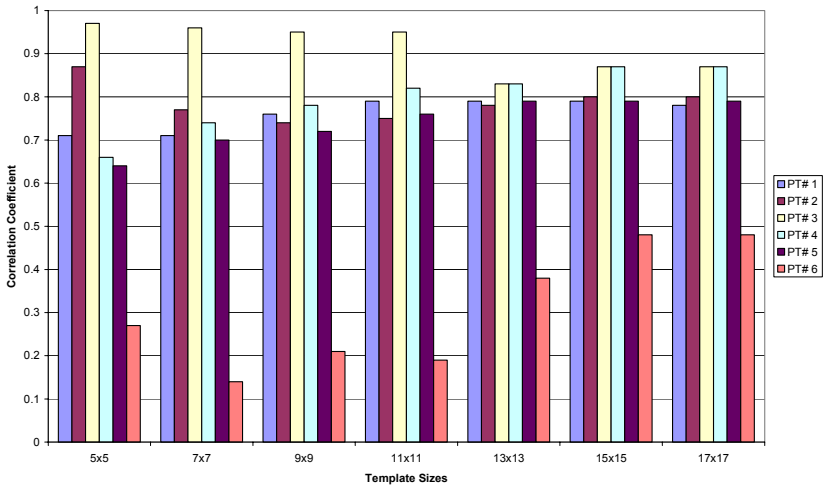

Figure 7.22: *Stereo matching Experiments Using Gamma Map 5x5 Filtered Stereo Pair*

Knowledge gained from these experiments was used to define the parameters to be utilized by the stereo matching algorithm. These strategy parameters are summarized in Table 7.4 and they were adopted along with the texture masks shown in Figure 7.18 to generate the disparity files for the stereo pairs from Radarsat and Envisat using the *IESSG Adaptive Matching Strategy* outlined in Figure 4.2. Since part of the research involves testing the influence of speckle filtering, disparity files were generated for the filtered and un-filtered Radarsat S7-W2 pair to further investigate this influence. The disparity and correlation images generated by the *Stereo Matching Module* for each of the stereo pairs are shown in Figure 7.23 to Figure 7.27. From these figures, observe that there are less correlated points as evidenced by the increase in black cells in the correlation image in Figure 7.25 and more artefacts, as seen in the parallax image , when using the un-filtered images.

Table 7.4: *Optimized Strategy Parameters Developed for Adaptive Stereo Matching Algorithm*

Sensor	***Radarsat***		***Envisat***	
Stereo Pair	***S7 – W2***		***IS7 – IS4***	***IS6 – IS4***
	Filtered	***Un-Filtered***		
Correlation Threshold	0.7	0.4	0.65	0.7
Template Minimum *(pixels)*	7	5	7	7
Template Maximum *(pixels)*	13	11	13	13
Start Pyramid	4	5	5	5
Stop Pyramid	0	0	0	0
X – Search *(pixels)*	1	1	1	1

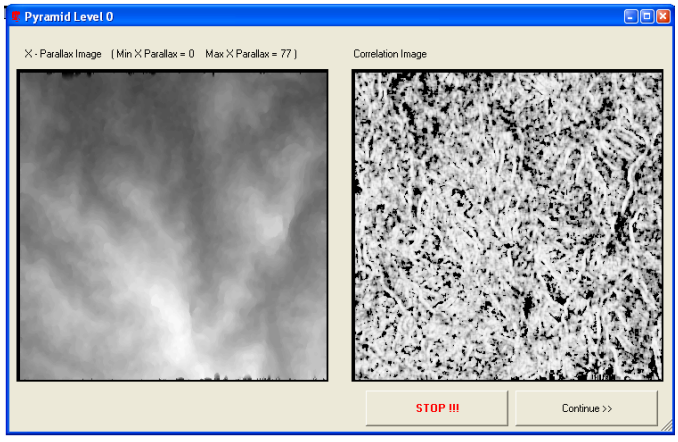

Figure 7.23: *Gamma Map 5x5 Filtered Radarsat S7-W2 Stereo Pair*

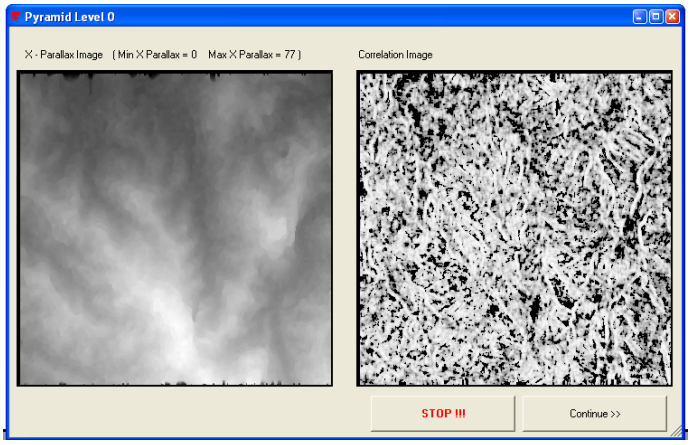

Figure 7.24: *Frost 5x5 Filtered Radarsat S7-W2 Stereo Pair*

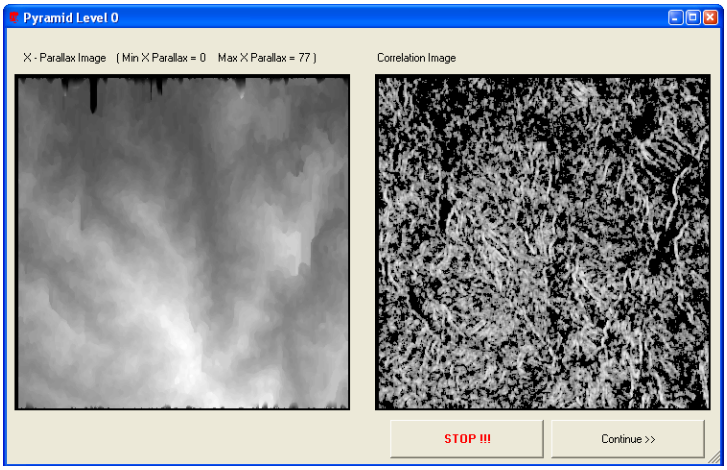

Figure 7.25: *Un-Filtered Radarsat S7-W2 Stereo Pair*

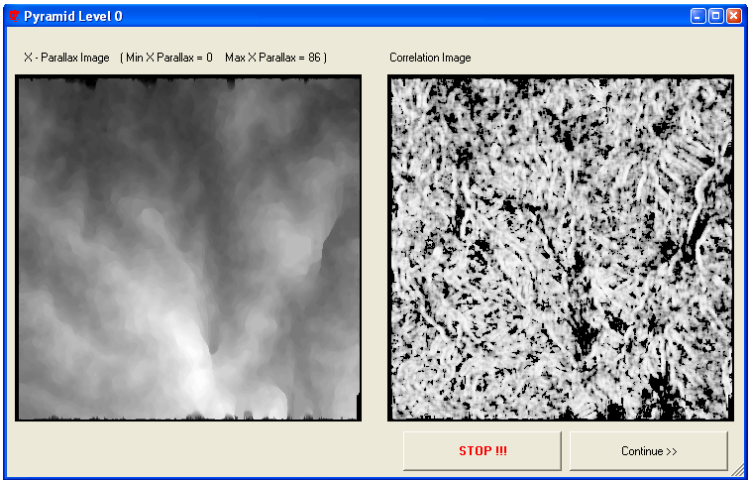

Figure 7.26: *Gamma Map 5x5 Filtered Envisat IS7 – IS4 Stereo Pair*

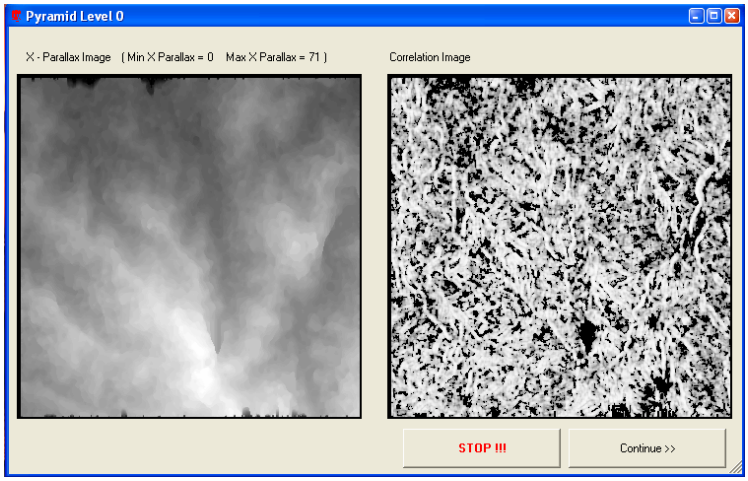

Figure 7.27: *Gamma Map 5x5 Filtered Envisat IS6 – IS4 Stereo Pair*

7.5.5 Space Intersection

Having generated disparity files for each of the stereo pairs being used in the application over the tropical region of Jamaica, the next phase is to convert the image coordinates to object space coordinates using the space intersection algorithms developed in chapter 5 and the software options illustrated in chapter 6.

In computing the 3D point cloud from the disparity files, the JAD69 datum was selected from the datum list, along with the Everett method of orbit interpolation for the Radarsat stereo pair and the spline method for the Envisat stereo pairs. The Jamaica Grid coordinates were computed for all points based on the definition for the local mapping system outlined in section 5.8.

7.6 Nottingham StereoSAR DSM Results

Based on the strategy followed in the previous section, the StereoSAR system was used to generate topographical information in the form of DSMs, with 50m spacing, using stereoscopic SAR pairs from Radarsat and Envisat satellites. In this section the DSMs and ortho-images are presented and only visual comparisons are made at this time. Detailed critical assessment of the various surfaces will be conducted later in section 7.7.

7.6.1 Radarsat DSM

Three images were available from the Radarsat satellite, two from the standard beam mode and one from the wide beam mode occupying positions S7, S1 and W2. The S1 image had severe layover in the study area and was difficult to match. The only stereo pair suitable for matching was the S7-W2. One of the objectives of the research was to investigate the influence of speckle filtering on the DSM product, so DSMs were generated using speckle filtered and non-speckle filtered images. All images were pre-processed using a standard deviation stretch with a factor of 2. Figure 7.28 presents the StereoSAR DSM results obtained using the Radarsat stereo pair.

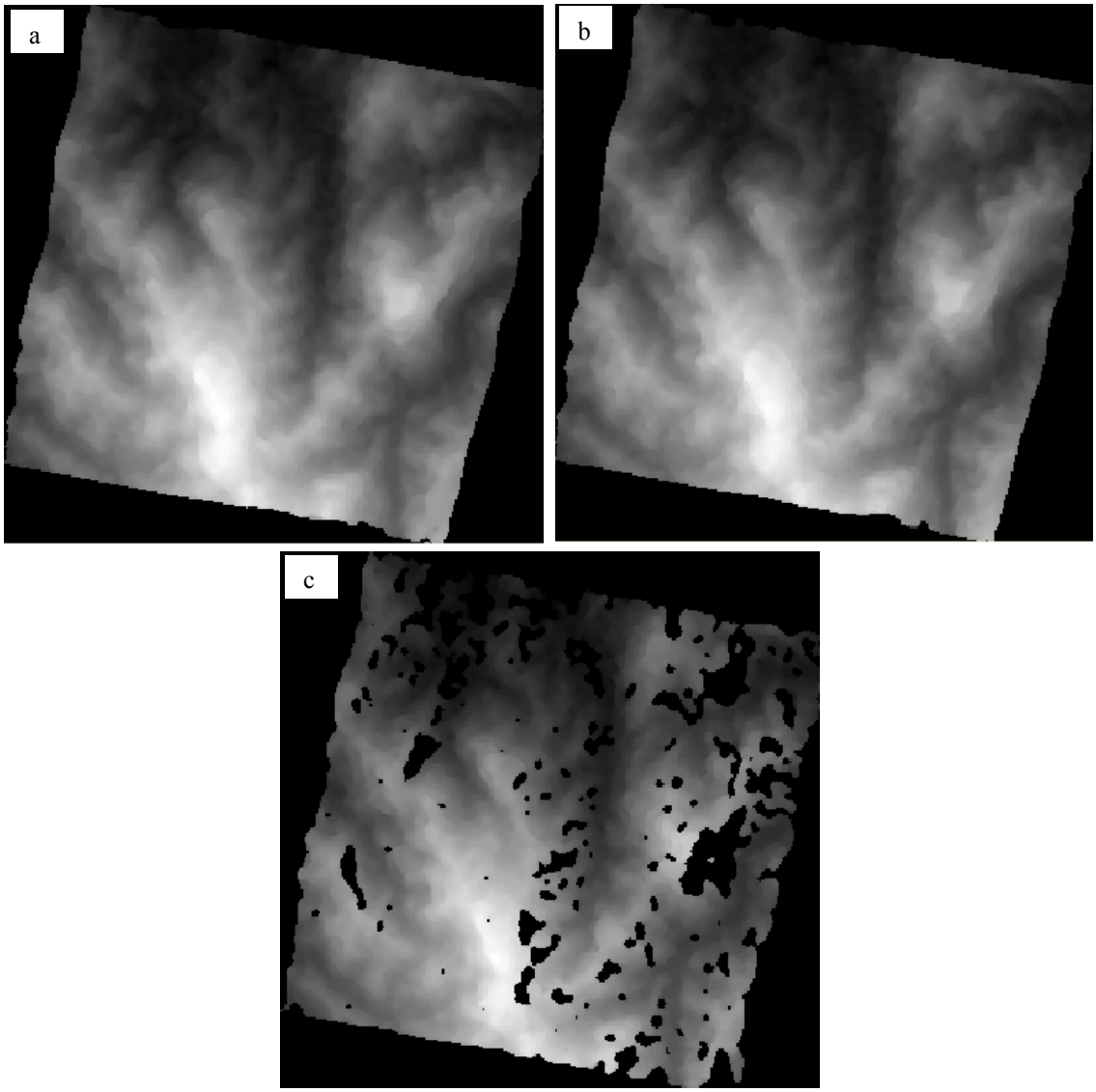

Figure 7.28: *StereoSAR DSM Generated using (a) Gamma Map5x5 Filtered (b) Frost 5x5 Filtered and (c) Un-Filtered , Radarsat S7-W2 Stereo Pair*

7.6.2 Envisat DSM

Of the five images available for forming stereo pairs only the Image Swaths IS4, IS6 and IS7 displayed the least effects of layover and foreshortening and therefore suitable for use in the StereoSAR software for generating DSMs over the study area. This allowed the formation of two stereo pairs IS7 – IS 4 and IS6 – IS4. The results of the DSM generation process using the Envisat images are shown in Figure 7.29 and also presented in *Edwards et al. 2005*.

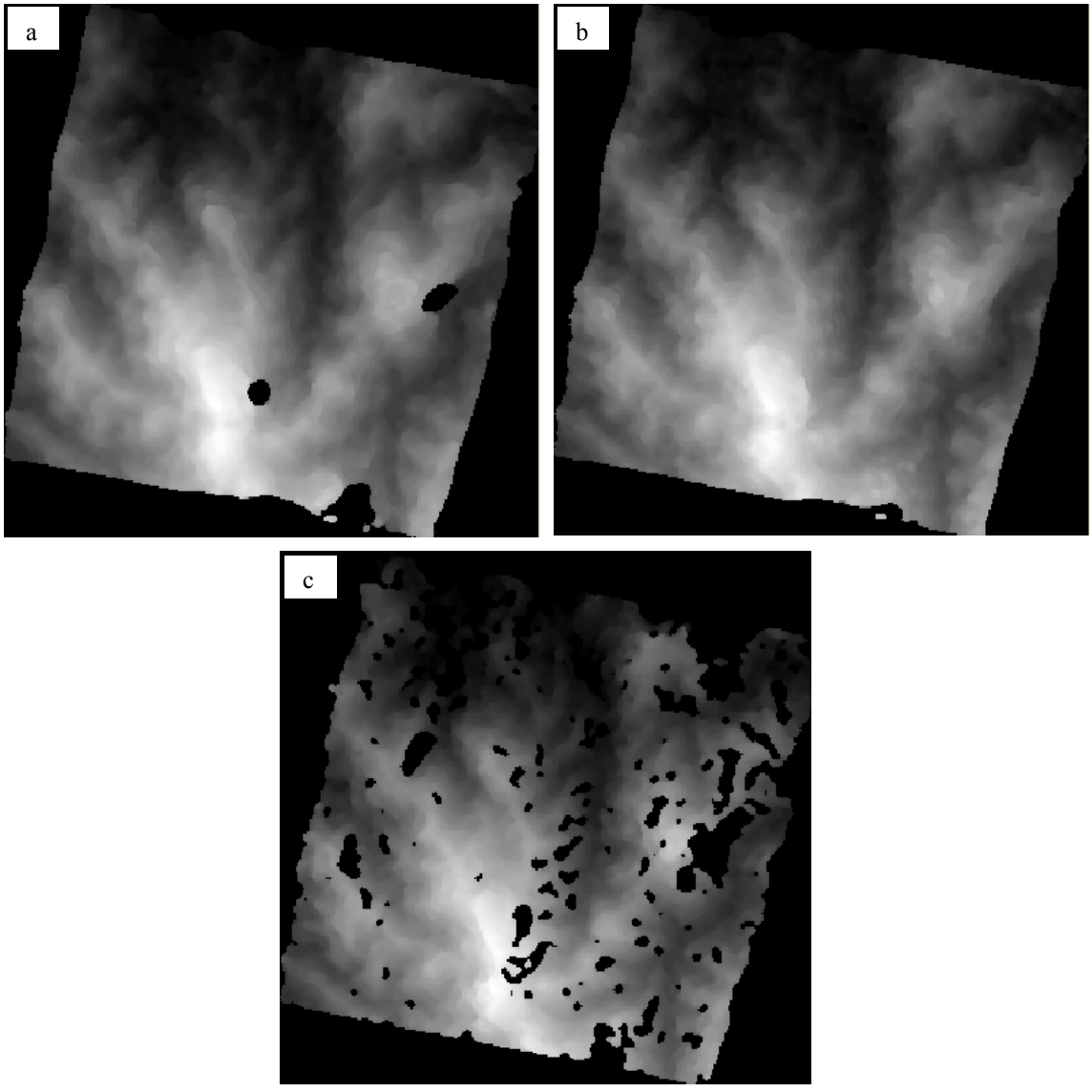

Figure 7.29: *StereoSAR DSM Generated using (a) Gamma Map5x5 Filtered IS7 – IS4 (b) Gamma Map 5x5 Filtered IS6 – IS4 and (c) Un-Filtered IS6 – IS4, Stereo Pairs*

7.6.3 Ortho-Images

A technique for simultaneously extracting the ortho-image during the DSM generation process was implemented in the StereoSAR system, as described in section 3.4.3.6. This allowed significant time savings by not having to first extract the DSM, and then use that DSM in a separate process to geocode the image as with some cases in the literature. The results of the automatically geocoded images, based on the reference image, are shown in Figure 7.30 for Radarsat and Figure 7.31 for Envisat.

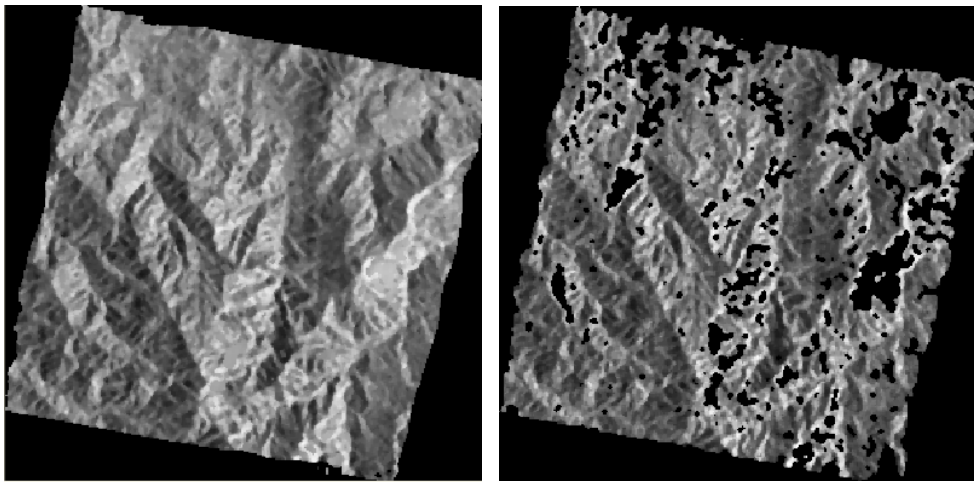

Figure 7.30: *Automatically Geocoded Radarsat Ortho-Image Based on Left: DSM Generated using Gamma Map5x5 Filtered Images and Right: DSM Generated using Un-Filtered Images, from Radarsat S7-W2 Stereo Pair*

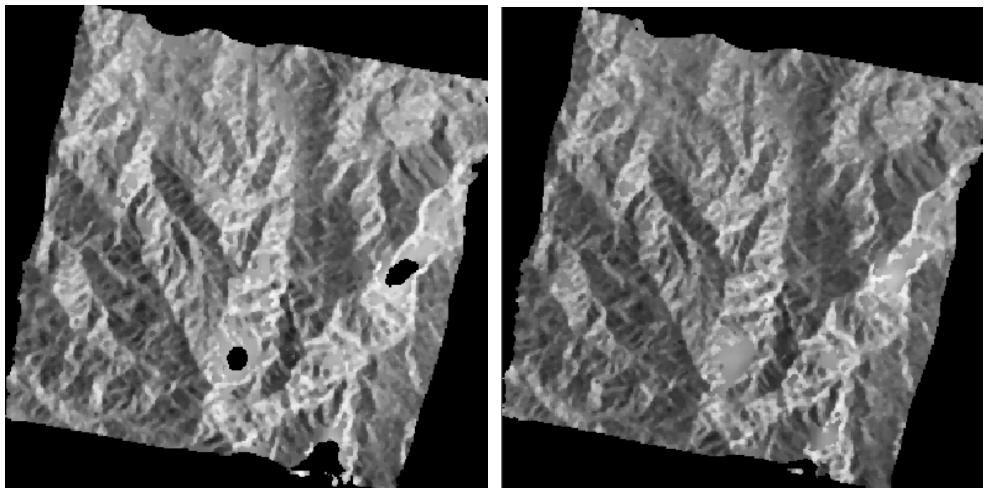

Figure 7.31: *Automatically Geocoded Envisat Ortho-Image Based on Left: DSM Generated using Gamma Map5x5 Filtered IS7-IS4 and Right: DSM Generated using Un-Filtered IS6-IS4, Envisat Stereo Pairs*

7.7 Critical Assessment of the Nottingham StereoSAR DSMs

The methods for assessing the quality of a DSM have been reviewed in section 3.5. Of these techniques, the use of the *mean* to indicate the existence of systematic errors, the *standard deviation* to indicate the internal reliability (precision/relative accuracy) and the *root mean square error* (RMSE) to estimate the absolute accuracy of the surface are quite common. These measures are global in nature using a single figure, usually the RMSE, to represent the accuracy of the entire DSM irrespective of the extents and landscape characteristics of the study area. When assessing the quality of a surface model, apart from indicating the global statistics there will also be the need to show the spatial distribution of elevation errors. This can usually be achieved by computing a difference image (reference DSM minus StereoSAR DSM) and representing the results using an appropriate colour-coded scheme.

The generation of the statistical measures is usually achieved by comparing the DSM to be assessed with a higher quality surface model, as noted earlier. In this section, the airborne InSAR DSM, evaluated previously, will be used to assess the quality of the DSMs generated by the *Nottingham StereoSAR System*. To facilitate this analysis, a 10km x 10km subset is extracted from the StereoSAR DSMs presented in section 7.6. This ensured that DSM edges did not influence the results.

The importance of having this high-resolution reference DSM cannot be overstated. Other researchers have noted that the lack of proper validation data have hindered their studies. *Premalatha 2001* concluded that the main shortcoming of her study of spaceborne repeat-pass InSAR DSMs over India was the lack of suitable validation data of higher order accuracy and that the study would have benefited from the availability of a 'quality tested' DSM. *Sowter 1998* successfully demonstrated the ability to generate StereoSAR DSMs over a remote area of Papua New Guinea; unfortunately, the author was unable to quantitatively assess the quality of the derived surface model due to the non-existence of proper validation data and had to rely on outdated topographical maps for visual comparisons. *Ka and Kim 2001* used StereoSAR techniques to generate a DSM over a part of Seoul and could only perform a qualitative assessment of the product using profiles generated from topographical maps due to a lack of suitable validation data.

7.7.1 Visual Analysis of the StereoSAR DSMs

In this analysis, three-dimensional (3D) views from the North West are created from the DSMs generated by the *Nottingham StereoSAR System*. The *ArcGIS 9.0 ArcScene Extension* was used in creating the 3D visualizations of the study area from the DSMs. A suitable colour ramp was selected for the representation of elevations which was set to the same range for all the DSMs, i.e. 22m – 1295m and the results are displayed in Figure 7.32. The StereoSAR DSMs are highlighting the main landscape characteristics of the study area when compared with the reference DSM, but some of the terrain features are smoothed out. Comparing the StereoSAR DSMs with each other, only subtle differences can be detected at this viewing scale.

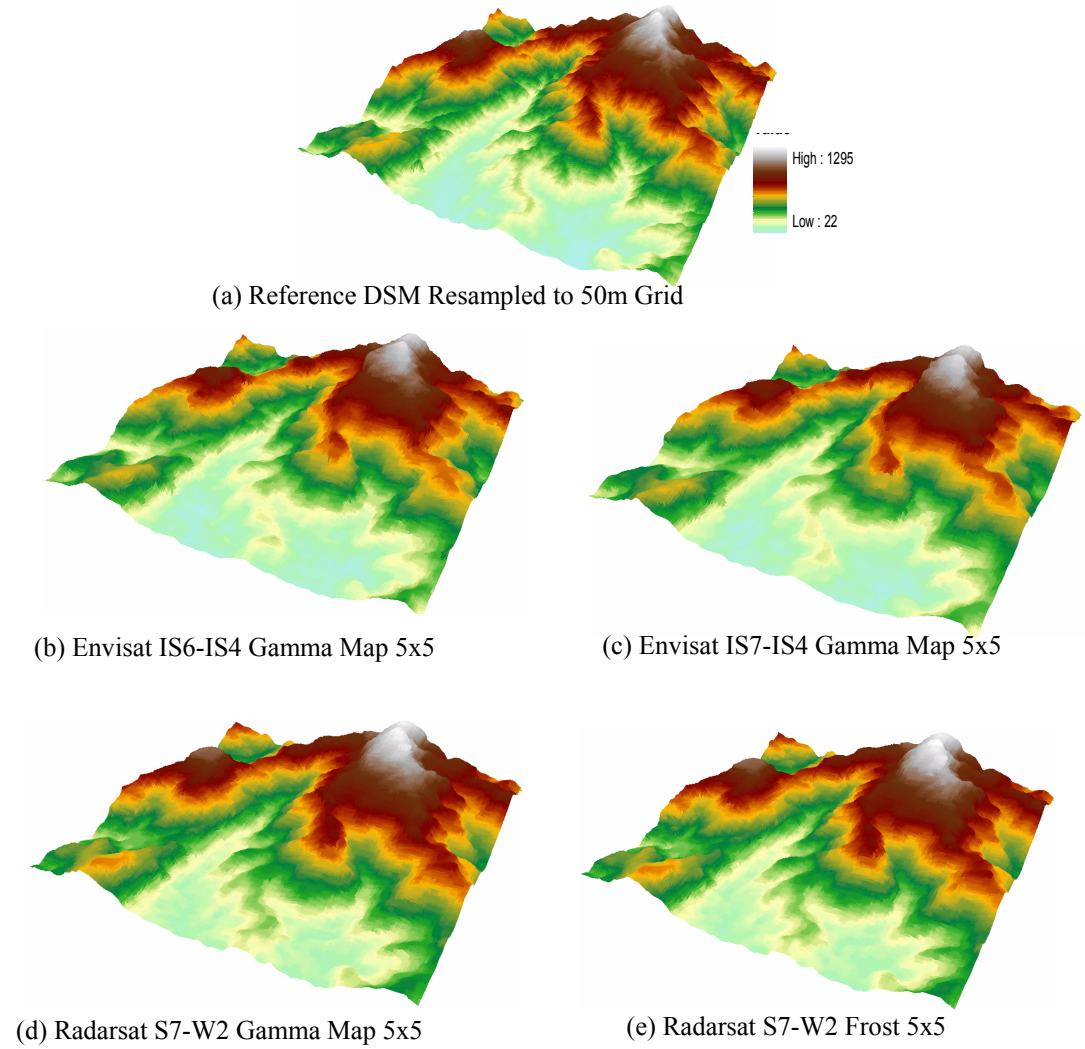

(a) Reference DSM Resampled to 50m Grid

(b) Envisat IS6-IS4 Gamma Map 5x5

(c) Envisat IS7-IS4 Gamma Map 5x5

(d) Radarsat S7-W2 Gamma Map 5x5

(e) Radarsat S7-W2 Frost 5x5

Figure 7.32: *Comparing the 3D views of StereoSAR DSMs with the Reference DSM*

Another method of visualizing the quality of the DSMs is to overlay other known data, such as contour lines (see section 7.3). In this study digital contour data in a GIS ready format was available for the study area. These contours were overlaid onto the StereoSAR DSMs and the surface inspected to see how well it matched. The results of this are shown in Figure 7.33. In all three cases the contours follow closely the colour coded values representing the elevations of the landscape. This highlights the suitability of the StereoSAR DSMs for medium to small scale mapping and visualization applications.

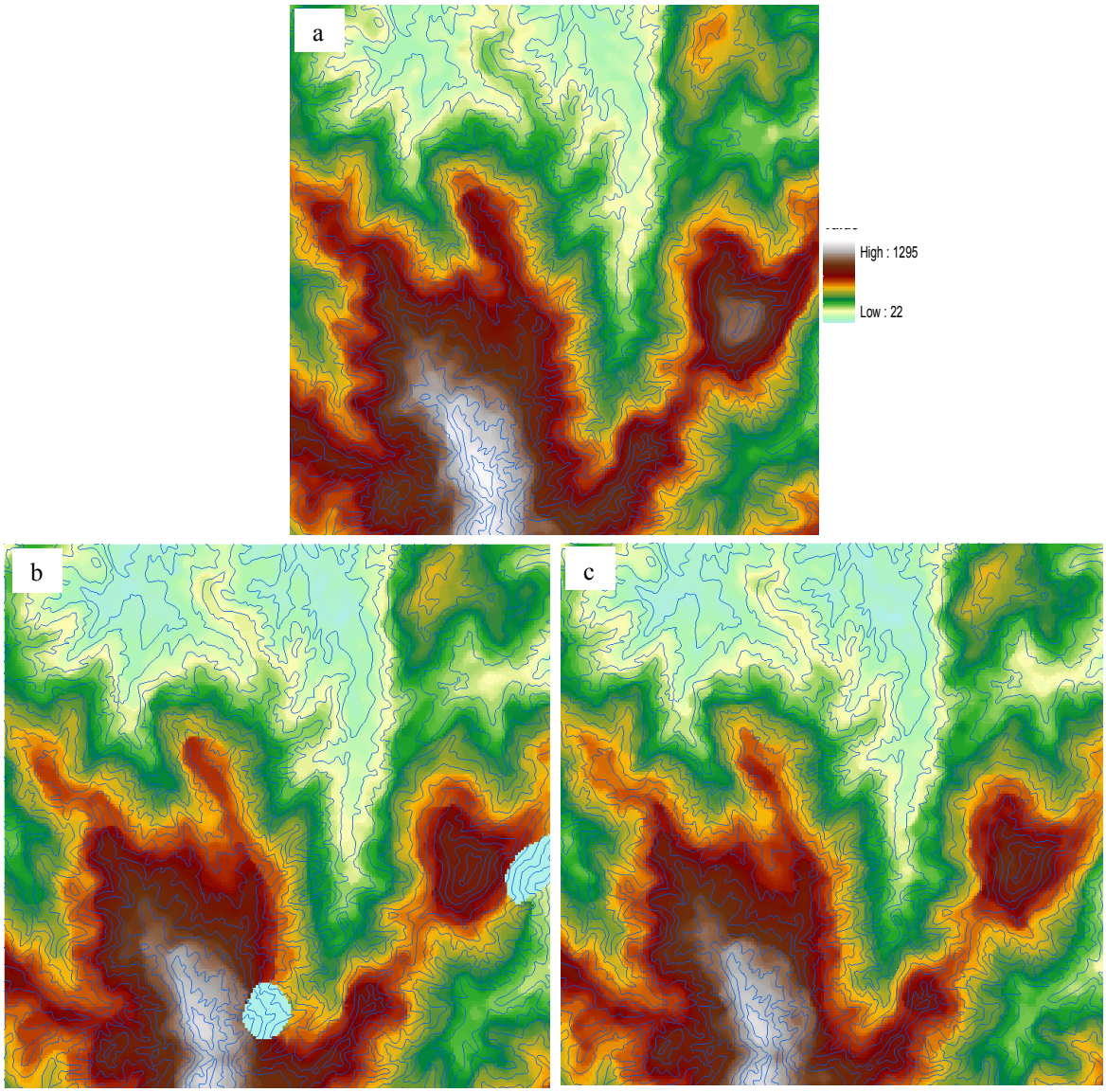

Figure 7.33: *Digital Contours Overlaid onto the Nottingham StereoSAR DSMs (a) Radarsat W2-S7 Gamma Map Filtered (b) Envisat IS7-IS6 Gamma Map Filtered and (c) Envisat IS6-IS4 Gamma Map Filtered*

7.7.2 Assessment Using Spatial Profiling

Additional assessment of the StereoSAR DSM was accomplished by performing qualitative analysis through the construction of profiles across the surface of the DSMs. This was done using the *ERDAS Imagine* software to create a *layer stack* for the DSMs and then utilizing the *spatial profile tool* in that software to generate two sets of profiles. The first set, shown in Figure 7.34, compares the DSMs generated using Radarsat images filtered by the Gamma Map and Frost speckle filters. The profiles do not seem to indicate any significant differences between the two DSMs.

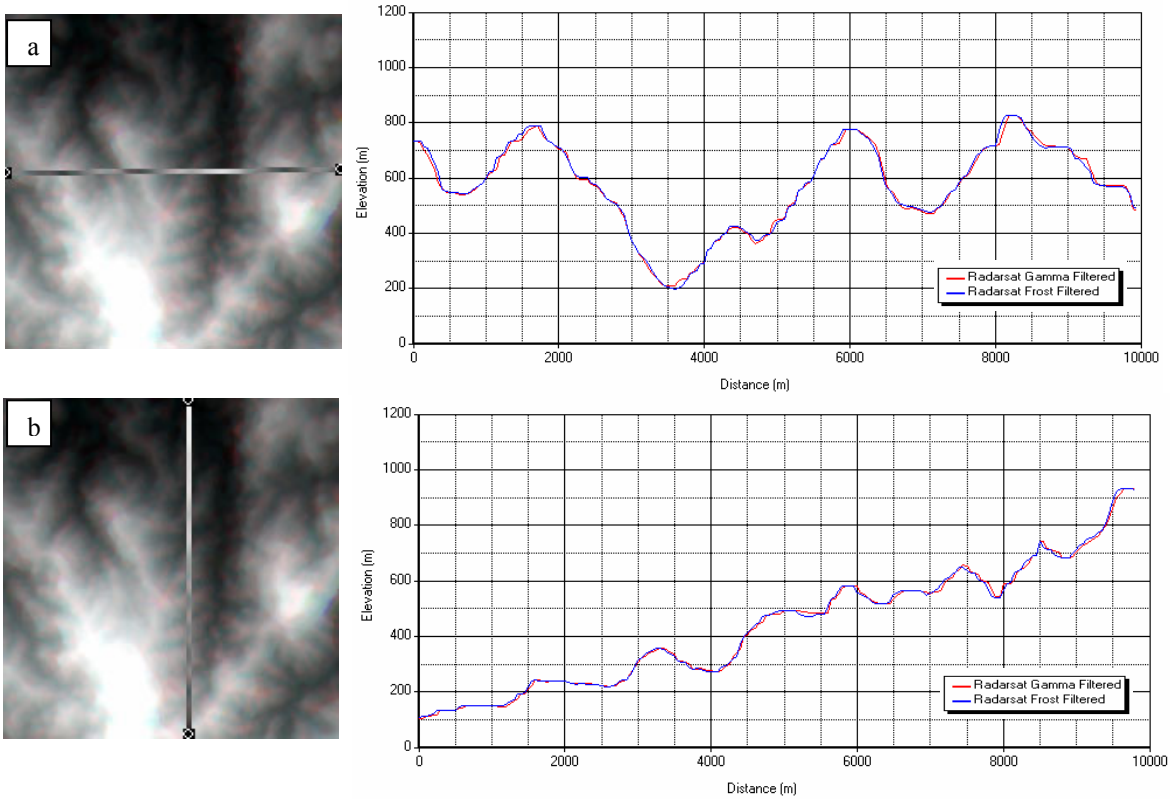

Figure 7.34: Spatial Profile Showing the Comparison between DSMs Generated Using Radarsat S7-W2 Gama Map Filtered and Frost Filtered Stereo Pairs (a)Taken East-West and (b) Taken North-South

The second set shown in Figure 7.35, compares the DSM generated from the Gamma Map filtered Radarsat S7-W2 stereo pairs with the reference DSM. It also compares the DSM generated from Envisat stereo pairs with the reference DSM. The spatial profiles created shows that the StereoSAR DSM is able to characterize the main terrain features. However, finer surface information is missing or smoothed out. It also shows that the algorithms tend to fill in valleys making them too high or smooth out hill tops making them too low as well as the systematic bias in the Radarsat DSM.

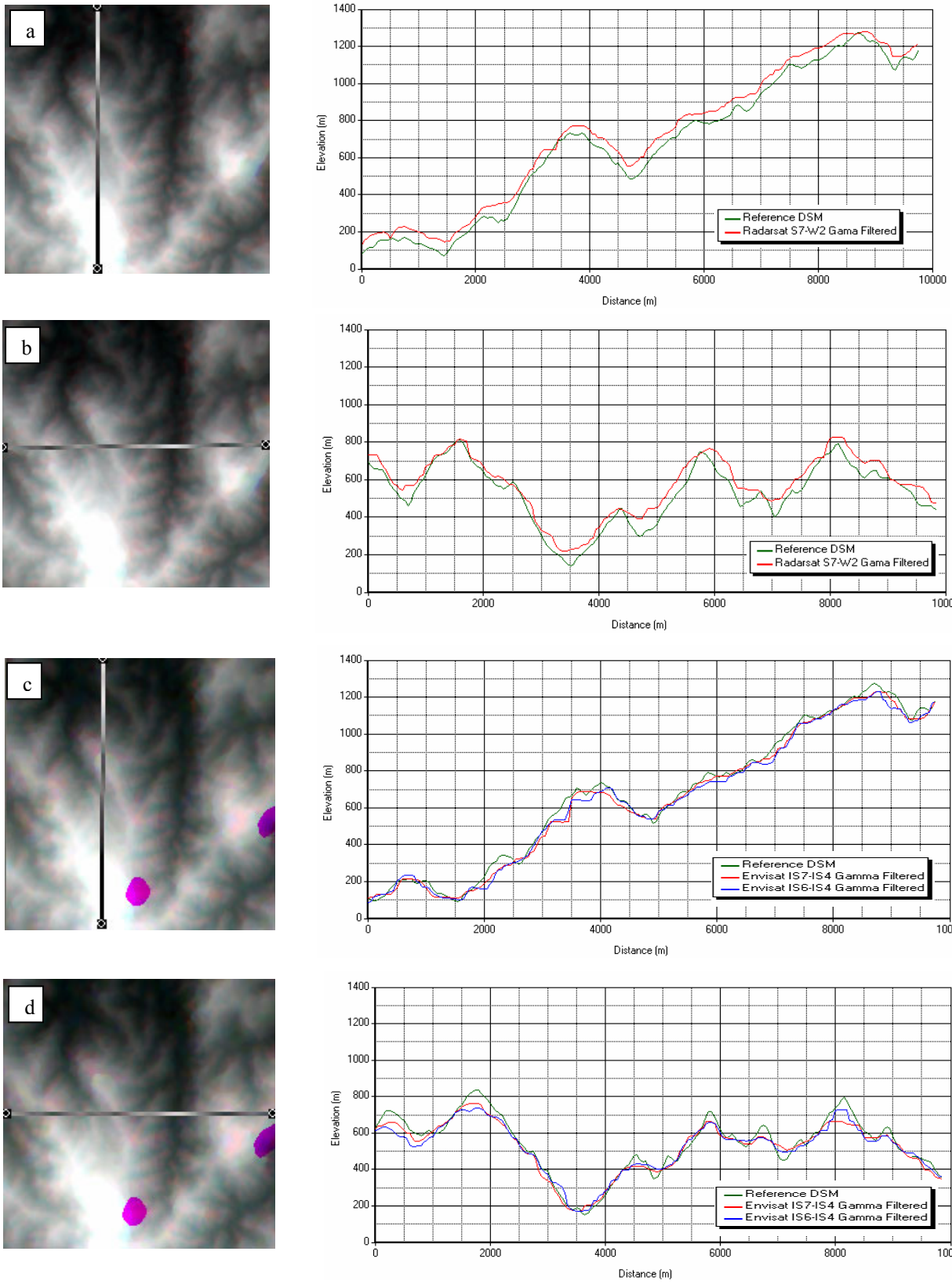

Figure 7.35: *Spatial Profiles Showing the Comparison between DSMs Generated Using Radarsat S7-W2 Gamma Map Filtered Stereo Pair and the reference DSM (a) East-West (b) North-South and Comparison between DSMs Generated Using Envisat IS7-IS4, IS6-IS4 Gamma Map Filtered Stereo Pairs and the Reference DSMs (c) North-South (d) East-West (the purple blobs in DSM images are due to data voids)*

7.7.3 Statistical (Quantitative) Accuracy Estimation of the StereoSAR DSMs

The vertical accuracy of the *Nottingham StereoSAR* DSMs generated in section 7.6 was determined by comparing it with the airborne InSAR reference DSM; the reference DSM was resampled to a 50m spacing to match the grid size of the StereoSAR DSM. Two approaches were used in arriving at the accuracy of the generated StereoSAR DSMs:

1. A set of 428 randomly located points well distributed across the 10km x 10km subset of the DSM, as shown in Figure 7.36, were created using *ESRI ArcGIS 9.0.* The elevations of these *check-points* were determined using an ESRI '*spot height*' script (obtained from *www.esri.com*) for extracting the elevations from both the reference DSM and the StereoSAR DSM at the check-point location. The differences in elevations at the check-points were computed and the statistical summary of this comparison is shown in Table 7.5. The analysis shows that the comparison with the check points yielded a SD of ~ 30m for all of the DSMs assessed.

2. The *Spatial Analyst Extension* from *ArcGIS 9.0* was used to compute difference images between the reference DSM and the StereoSAR DSMs. This yielded differences at 40,401 grid cells which represent the entire 10km x 10km surface. Histograms were generated to assess the distribution of the differences and also to visually indicate the existence of systematic biases. Table 7.6 shows the summary of statistics generated from the image differences; the histograms can be seen in Figure 7.37 to Figure 7.38.

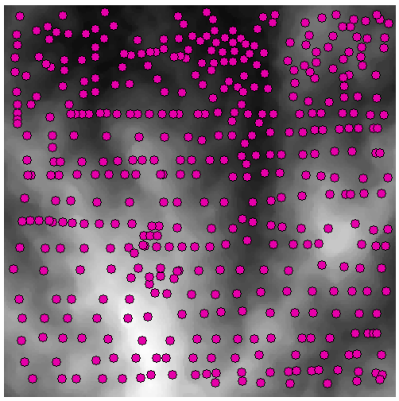

Figure 7.36: *Distribution of 428 Check-Points in 10kmx10km StereoSAR DSM*

Table 7.5: *Summary of Statistics for DSM Comparisons at Check-Points (Ref. DSM-StereoSAR DSM)*

Reference DSM Compared With	***No. of Samples Compared***	***Mean (m)***	***Std. Dev. (m)***	***RMSE (m)***	***Min. (m)***	***Max. (m)***
Radarsat S7-W2 Gamma Map Filtered	428	-58.1	28.7	64.8	-139	38
Radarsat S7-W2 Frost Filtered	428	-59.8	30.1	66.9	-142	44
Radarsat S7-W2 Un-Filtered	353	-52.4	33.0	62.0	-153	223
Envisat IS7-IS4 Gamma Map Filtered	415	+8.0	31.8	32.8	-81	130
Envisat IS6-IS4 Gamma Map Filtered	428	+11.2	33.6	35.4	-81	148
Adjusted Radarsat S7-W2 Gamma Map Filtered	428	-2.1	28.7	28.7	-83.0	94
Adjusted Radarsat S7-W2 Frost Filtered	428	-3.8	30.1	30.3	-86	100
Adjusted Radarsat S7-W2 Un-Filtered	353	+3.5	33.0	33.1	-97	279

Some check-points could not be used in the assessment of the DSM generated from the Envisat IS7-IS4 stereo pair and the DSM generated from the unfiltered Radarsat S7-W2 stereo pair, because they fell in the data void areas of those surface models. From the summary of statistics presented in Table 7.5, there is an evident systematic bias in the DSMs generated using Radarsat data. This bias was first noted in section 5.8.1.2 during the performance testing of the space intersection algorithm. The bias is also illustrated in the profiles in Figure 7.35(a) and Figure 7.35(b). Correcting for this systematic bias improves the estimate of the RMSE as shown in Table 7.5.

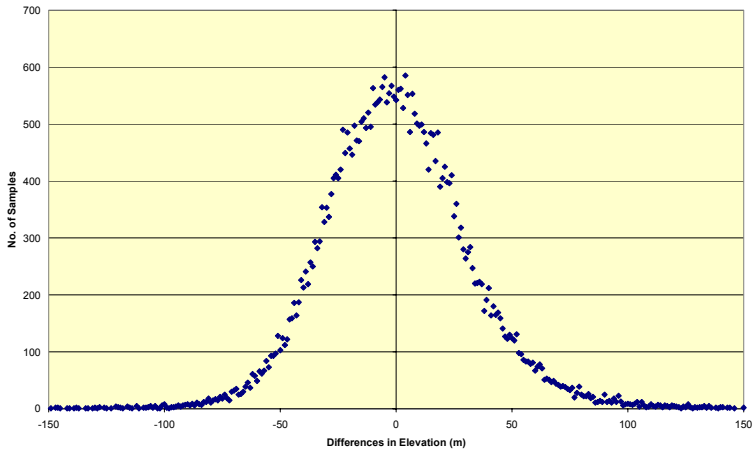

Figure 7.37: *Histogram of Elevation Differences between Reference DSM and Adjusted Radarsat S7-W2 Gamma Map Filtered DSM*

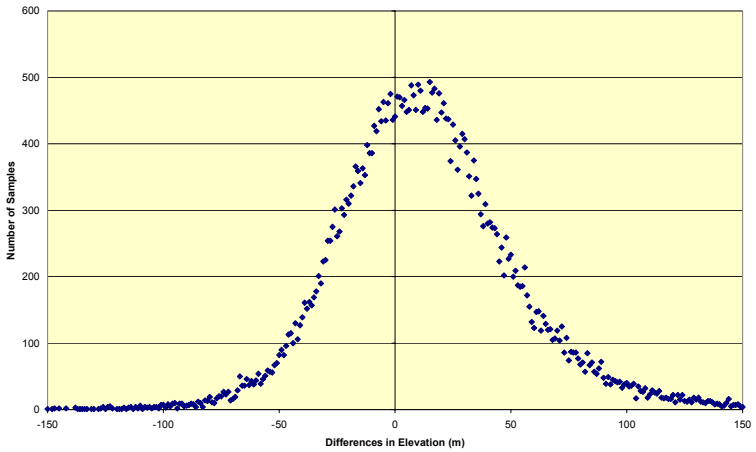

Figure 7.38: *Histogram of Elevation Differences between Reference DSM and Envisat IS6-IS4 Gamma Map Filtered DSM*

The use of check-points tends to give estimates based on the locations sampled and these may not be representative of the nature of the entire surface of the model as noted in section 3.5. If a 'high quality' surface is available then a direct subtraction will yield differences for each pixel in the DSM, as described earlier. The statistics generated from this second approach is shown in Table 7.6. Comparing these values with Table 7.5, it can be seen that including more points also increases the noise (min, max values) and standard deviation values.

Table 7.6: *Summary of Statistics Generated from the Difference between DSM Grids*

Reference DSM Compared With	***No. of Samples Compared***	***Mean (m)***	***Std. Dev. (m)***	***RMSE (m)***	***Min. (m)***	***Max. (m)***
Adjusted Radarsat S7-W2 Gamma Map Filtered	40,401	+0.4	31.3	31.3	-174	+152
Envisat IS6-IS4 Gamma Map Filtered	40,401	+13.7	36.6	38.4	-171	+183

7.7.4 Spatial Distribution of Elevation Errors

As mentioned earlier, statistical measures such as mean, standard deviation and root mean square error do not give information on the spatial distribution of the elevation differences across a DSM. In Table 7.6, difference information was used to generate global statistical measures but these differences can also be used to represent the variation of the differences across the surface. The differences computed in section 7.7.3 were colour coded in *ArcGIS 9.0* to show the variations. The results are illustrated in Figure7.39 and Figure 7.40. It can be seen that the largest errors occur in the areas influenced by layover, foreshortening and shadows which increase the dissimilarity between stereo pairs in these areas. Good results occur in moderate to flat terrain as can be seen.

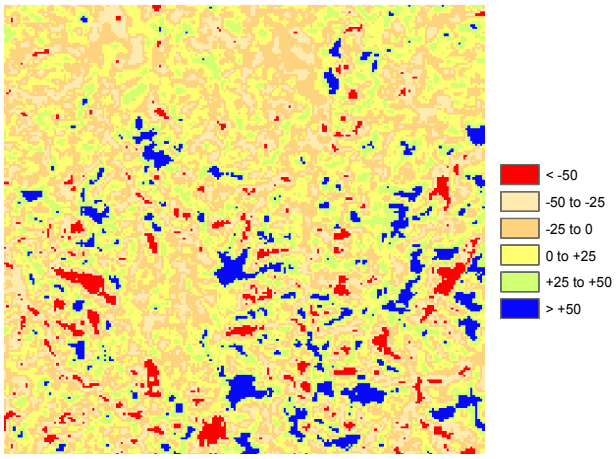

Figure 7.39: *Spatial Distribution of Elevation Differences between the Reference DSM and the DSM Generated from Radarsat S7-W2 Gamma Map Filtered Stereo Pair*

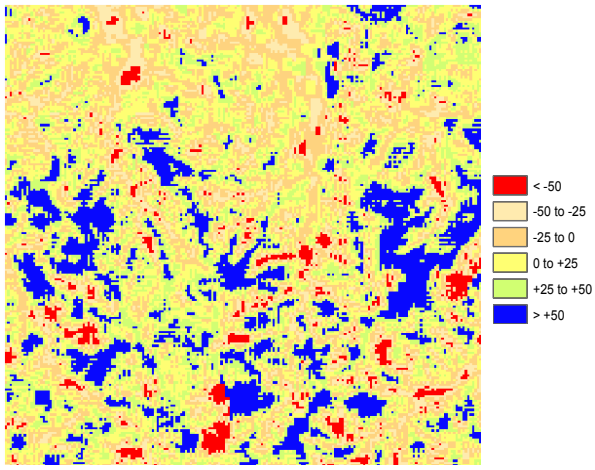

Figure 7.40: *Spatial Distribution of Elevation Differences between the Reference DSM and the DSM Generated from Envisat IS6-IS4 Gamma Map Filtered Stereo Pair*

7.7.5 Sensitivity of Space Intersection Algorithm to Matching Errors

Experiments were conducted to evaluate the sensitivity of the space intersection algorithm to errors in determining the correct location of conjugate points, which will result in errors in x-parallax. To test this sensitivity, points measured in the image from satellite S_1 were assumed to be error-free and errors of +1, +2, and +3 pixels were applied to the column values of the points related to the image from satellite S_2 and then processed with the *IESSG Space Intersection Algorithm*. The effect of these errors on the position (N, E) and height (H) of the test points are shown in Table 7.7 and have also been presented in *Edwards et al. 2004*.

As can be seen from Table 7.7, the longer baseline tends to give better results. Misidentification of the conjugate point by ±3 pixels results in differences in height from ±29 to ±98m when compared with the error-free values and depends on baseline length. Based on experiments performed by *Leberl et al. 1994*, it is possible to automatically determine conjugate points to within 2 pixels of manually extracted values. Matching accuracy and baseline length are critical factors in the space intersection strategy and will therefore influence the final 3D position of the terrain point.

Table 7.7: *Sensitivity Analysis of the Space Intersection Algorithm to Errors in x – Parallax*

Stereo Pair	Baseline (km)	Shifts	x Parallax Errors		
			+1	+2	+3
Radarsat S1-S7	490	dN (m)	-2	-4	-5
		dE (m)	+9	+17	+25
		dH (m)	-10	-19	-29
Envisat IS2-IS6	335	dN (m)	+3	+5	+8
		dE (m)	-13	-25	-38
		dH (m)	+12	+23	+35
Envisat IS3-IS6	250	dN (m)	+4	+8	+12
		dE (m)	-21	-41	-61
		dH (m)	+19	+38	+58
Radarsat W2-S7	243	dN (m)	-6	-11	-16
		dE (m)	+28	+55	+83
		dH (m)	-33	-65	-98

7.7.6 Influence of Speckle Filtering

One of the objectives of this research was to evaluate the effects of speckle filtering on the quality of the StereoSAR DSM. There exists conflicting views as to whether or not to speckle filter images before use in stereo matching algorithms. Some authors are in support of speckle filtering while others are not. The literature had identified Gamma Map or Frost as being the most suitable for speckle filtering, based on studies carried out by different researchers.

In this study, the StereoSAR system developed provided options for speckle filtering SAR images. Images were filtered using Gamma Map and Frost in the case of Radarsat and Gamma Map in the case of Envisat using a 5x5 kernel in both cases. The filtered and un-filtered images were used in the *Co-Registration Module* to compute the initial coarse registration of the stereo pairs. It was found that images that were not speckle filtered struggled to produce enough high quality tie-points for the generation of polynomial coefficients for the co-registration. Images that were filtered showed a ~500% increase in the number of tie-points found, even when setting a high correlation threshold value of 0.9 (see Figure 7.19 and Figure 7.20).

DSMs were generated using both speckle filtered and un-filtered images and the results were presented in section 7.6. The results showed that the unfiltered images generated a surface filled with several areas that were void of data. This could be attributed to the fact that the matching is struggling with the speckle at the last pyramid level. Those images that were speckle filtered produced complete surfaces and with less noise (i.e. min to max values) than the un-filtered images. Figure 7.34 showed a comparison between DSMs generated from Frost filtered and Gamma Filtered Images and the differences were marginal. This same marginal difference was also evident in Table 7.5. This seems to suggest, that while there may be great benefits from speckle filtering the image before matching, it may not be important whether the filter used is a Frost or Gamma Map. Despite this, Gamma Map was the preferred filter for this research mainly because during its execution it filters the image based on rules governing whether or not the pixel falls in a homogeneous, textured or strong scatter area (*Lopes et al. 1990b*).

7.8 Summary

The *Nottingham StereoSAR System* developed in this research was tested over Jamaica, a tropical region in the Caribbean, to demonstrate its capabilities and assess the quality of the DSM output. The results showed that the system is functioning and is capable of producing DSMs and ortho-images for an area where spaceborne repeat-pass interferometry failed to produce a surface model. Moreover, the system is capable of achieving these results without any need for GCPs to an accuracy level of ~ ± 30m using images with the characteristics outlined in section 7.3. There were no published studies found using the Radarsat S7-W2 stereo pair, or any using Envisat stereo pairs, with which to compare the results of this research. *Chen 2000* used Radarsat S7 and S1 and quoted accuracies of ±32m in hilly terrain.

Images speckle filtered before use in the StereoSAR system showed better results for co-registration and disparity, than those images that were un-filtered. The resulting DSM based on the filtered images also showed significantly less data voids compared to un-filtered images.

The technique that was implemented in the system to simultaneously extract the ortho-image and DSM functioned as expected and section 7.6.3 shows some examples. This demonstrates that the system also has the capability to generate rectified SAR images as well as DSMs for Caribbean territories.

The common practise of assessing DSM quality is to generate statistical measures such as RMSE, which is used to indicate the accuracy of the surface. In this research, in addition to statistical measures, GIS tools were utilized to generate elevation difference images which were colour coded to show the spatial variation of the errors. The results shown in section 7.7.4 indicate that the flat areas exhibit fewer errors than the hilly part of the study area. This may be because of the effects of layover in these hilly areas and the difference image may be a useful tool for investigating the further development of the image matching algorithm so as to enhance its performance in these areas.

Chapter 8

Conclusions and Recommendations

8.1 Conclusions

This thesis has presented research into the development of algorithms and software for extracting topographical information from stereoscopic pairs of Radarsat and Envisat imagery for use over cloud affected territories. These algorithms have been integrated into a software package called the *Nottingham StereoSAR System,* also developed in this research, which was successfully tested over a tropical region – the Caribbean island of Jamaica - and accuracy assessments performed on the results. The following is a summary of the main conclusions resulting from the research, based on the findings presented elsewhere in the thesis.

- Developing countries have financial difficulties which result in limited resources being available for the generation of topographical information and these countries must rely on the near global data coverage available from spaceborne platforms.

- Many of these developing countries are located in the tropical zone where there is often cloud cover problems, making SAR a compelling alternative to optical techniques for the generation of topographical information over these areas.

- Chapter 3 introduced the various techniques that exist for the extraction of topographical information from SAR data; the two most common being *Interferometric SAR (InSAR)* and *Stereoscopic SAR (StereoSAR)*. While each method provides different levels of measurement accuracies, its use over developing countries will be determined by cost, landscape characteristics, time lapse between concept and implementation, knowledge and expertise needed to collect the data and extract the

topographical information. Spaceborne repeat-pass interferometry was tested over Jamaica and it failed to produce a surface model due to loss of coherence over the vegetated and steep nature of the Jamaican landscape. This meant that the only other spaceborne alternative was the use of StereoSAR.

- The processing chain for StereoSAR comprises many steps. The two identified as the most critical were stereo matching and space intersection. Errors at these levels will have a significant impact on the generated surface model.

- Chapter 4 reviewed the techniques available for matching pairs of stereoscopic SAR imagery. Of these, the *normalized cross correlation* and *least squares correlation* techniques, implemented using automated strategies, were more appropriate for use with SAR imagery.

- Most of the strategies available for stereo matching make use of the normalized cross correlation method because it is faster in processing than the least squares correlation and easier to implement. However, the strategies currently in practise normally use fixed correlation windows and thresholds for determining match locations and this can be problematic in low textured areas.

- An alternative strategy was developed in this research that adapts the window size based on the texture, or lack there of, in the image. A first order statistical texture filter was used to segment the images into areas of low texture and high texture. The *adaptive matching algorithm* was implemented using a hierarchical approach based on image pyramids. A coarse registration of the images was first carried out automatically by the algorithm, to reduce the search space and thereby speeding up the matching process.

- A GCP-free *space intersection algorithm* has been developed in this research, which makes use of zero-Doppler stereoscopic SAR imagery. GCP points are difficult to detect in SAR imagery due to speckle noise and the lack of well contrasting cultural features. This algorithm is designed to use both Radarsat and Envisat datasets. In the past, interpolation methods were not used with Radarsat data to determine position and velocity of the satellite, mainly because of the 480 seconds spacing of orbital data. The practise was to use orbit integration methods which proved, on their own, to be very computer intensive. In this research, an Everett interpolation method was implemented for use on the Radarsat orbits. The method was tested against a known DORIS orbit of Envisat and it was found that an 8^{th} order Everett interpolation was appropriate for use with Radarsat, resulting in discrepancies of 3.2m in X, -7.6m in Y and 2.2m in Z; all within the known orbital accuracy for Radarsat satellite.

- The algorithm was tested on a sample of points to compare its performance with Envisat and Radarsat data. Until now, space intersection techniques have not been tested on Envisat satellite data so there were no results from this sensor for comparison. The results for Radarsat showed a ~55m bias in the height, and this suggests that if accurate heighting is required this systematic error would have to be removed using at least two GCPs, as suggested by other authors. Surprisingly, the results from Envisat did not show any systematic biases in the height component, with differences less than ~ 4m. This showed the advantage of the superior orbit of Envisat over Radarsat. These results also confirmed that the space intersection algorithm was functioning correctly.

- The Adaptive matching and space intersection algorithms, along with other modules programmed using the C# language, was integrated to form a system appropriately named the *Nottingham StereoSAR System*. The system is designed using GUI to allow ease of operation and quick recovery from errors due to user input. The fact that the code is available makes the system an ideal platform for conducting related research activities.

- The Nottingham StereoSAR System was tested over the Caribbean island of Jamaica to demonstrate its ability to produce topographical information over such areas. DSMs were generated using stereoscopic pairs from both Radarsat and Envisat.

- The DSMs were critically assessed by comparing the generated surface with a high resolution surface from airborne InSAR. Jamaica is the only one, of nearly 25 islands, to have such validation dataset and this research was fortunate to benefit from it. Statistical measures and difference maps were generated based on the comparisons. The results for Radarsat showed the ~55m bias that was identified during the testing of the space intersection algorithm. The results for Envisat showed elevation biases of less than 11m. 3D visual comparison showed the DSMs generated were highlighting the main landforms, with hills and valleys identifiable. The algorithms were however smoothing out the finer topographic details.

- Analysis was conducted on the space intersection algorithm to determine its sensitivity to errors from the adaptive stereo matching strategy. The investigation showed that the longer baselines tend to give better results. It also revealed that matching errors up to ~3 pixels will result in height errors of ranging from 29m to 98m depending on satellite and baseline length. It is therefore inferred from these results, that small matching accuracy and long baseline will result in accurate heights. Of course, there must be some trade-off between the effort to obtain sub-pixel level of matching accuracy, and this will be determined by cost, time and intended use of the application.

- The benefits of speckle filtering images before matching were tested during the extraction of DSMs. The results showed that images that were speckle filtered produced a more complete surface, almost no data voids. It also showed a ~500% improvement in determining tie-points at the co-registration stage.

8.2 Recommendations for Future Research

Based on the research reported in this thesis and the conclusions deduced from the results of the study, the following recommendations are being made for possible future work to extend the potential of the *Nottingham StereoSAR System*.

- Radarsat-2 will be launched as early as 2006. This sensor is expected to have resolutions as high as 3m. The StereoSAR system should be tested with this dataset and improvements made where necessary to capitalize on the improved characteristics of the sensor.

- Since the research showed that there are benefits from speckle filtering images before stereo matching, other methods of speckle filtering such as wavelets could be explored to identify any potential benefits for stereo matching.

- The space intersection technique can be modified to take advantage of the launching of new SAR sensors with good quality orbits. The sensor model could be modified to allow the mixing of different satellite sensors.

- The adaptive stereo matching algorithm is by no means a perfect one. Investigations should take place to determine if other ancillary data, apart from texture, can be used to adapt parameters to the landscape.

References

Ackerman, F. (1984), "Digital Image Correlation: Performance & Potential Applications in Photogrammetry", *Photogrammetric Record*, vol. 11, no. 64, pp. 429-439.

Agrotis, L. G. (1984), *Determination of satellite orbits and the global positioning system,* PhD Thesis, University of Nottingham.

Asal, F. F. (2003), *Airborne Remote Sensing for Landscape Modelling,* PhD. Thesis, University of Nottingham.

ASPRS (1998), *Manual of Remote Sensing: Principles and Applications of Imaging Radar*, 3 rd edn, John Wiley and Sons, NY, USA.

ASPRS (2004), *Manual of Photogrammetry*, 5 th edn, American Society for Photogrammetry and Remote Sensing, Bethesda, Maryland.

Bach, K. (2003), *E-Mail Communication* Radarsat International, Canada.

Baltavias, E. P. (1999), "Airborne Laser Scanning: Basic Relations and Formulas", *ISPRS Journal of Photogrammetry & Remote Sensing*, vol. 54, pp. 199-214.

Bamler, R. and Schattler, B. (1993), "SAR Data Acquisition and Image Formation," in *SAR Geocoding: Data and Systems*, G. Schreier, ed., Wichmann, Karlsruhe, pp. 53-102.

Bannister, A., Raymond, S., & Baker, R. (1998), *Surveying* Longman, Harlow.

Belgued, Y., Hervet, E., Marthon, P., Lemaréchal, C., Rognant, L., & Adragna, F. (1999), "An Accurate Radargrammetric Chain for DEM Generation", *SAR Workshop: CEOS Committee on Earth Observation Satellites; Working Group on*

Calibration and Validation, Proceedings of a Conference held 26-29 October 1999, Toulouse, France pp. 167-172.

Berry, P. A. M. (2000), "Topography from Land Radar Altimeter Data: Possibilities & Restrictions", *Physics and Chemistry of the Solid Earth - Part A*, vol. 25, no. 1, pp. 81-88.

Burrough, P. A. and McDonnell, R. A. (1998), *Principles of Geographical Information Systems* Oxford University Press, New York.

Campbell, J. B. (2002), *Introduction to Remote Sensing*, 3rd edn, Taylor & Francis, London.

Caspary, W. and Joos, G. (2002), "Statistical quality control of geodata," in *Spatial Data Quality*, Shi W, Fisher P.F, & Goodchild M.F, eds., Taylor and Francis, London, pp. 106-115.

Chen, P. H. (2000), *Extraction of Spatial Information from Stereoscopic SAR images,* PhD Thesis, University College London.

Chen, P. H. and Dowman, I. J. (2001), "A Weighted Least Squares Solution for Space Intersection of Spaceborne Stereo SAR Data", *IEEE Transactions on Geoscience and Remote Sensing*, vol. 39, no. 2, pp. 233-240.

Chen, P. H. and Dowman, I. J. (1996), "Space Intersection from ERS-1 Synthetic Aperture Radar Images", *Photogrammetric Record*, vol. 15, no. 88, pp. 561-573.

Clarke, C. (1991), *Geocoding and Stereoscopy of Synthetic Aperture Radar,* PhD Thesis, University College London.

Cooper , M. A. R. (1998), "Datums, Coordinates and Differences," in *Landform Monitoring, Modelling and Analysis*, S. N. Lane, K. S. Richards, & J. H. Chandler, eds., John Wiley and Sons, Chichester, pp. 21-36.

Cooper, M. A. R. and Cross, P. A. (1988), "Statistical concepts and their application in photogrammetry and surveying", *Photogrammetric Record*, vol. 12, pp. 637-663.

Curlander, J. C. (1982), "Location of Spaceborne SAR Imagery", *IEEE Transactions on Geoscience and Remote Sensing*, vol. 20, no. 3, pp. 359-364.

Curlander, J. C. (1984), "Utilization of Spaceborne SAR Data for Mapping", *IEEE Transactions on Geoscience and Remote Sensing*, vol. 22, no. 2, pp. 106-112.

Curlander, J. C., Kwok, R., & Pang, S. S. (1987), "A Post-Processing System for Automated Rectification and Registration of Spaceborne SAR Imagery", *International Journal of Remote Sensing*, vol. 8, no. 4, pp. 621-638.

Curlander, J. C. and Mcdonough, R. N. (1991), *Synthetic Aperture Radar: Systems and Signal Processing* John Wiley & Sons, New York.

Daniel, C. and Tennant, K. (2001), "DEM quality assessment," in *Digital Elevation Model Techniques and Applications: The DEM Users manual*, Maune D.F, ed., ASPRS, Maryland, pp. 395-440.

Dare, P. M. (1999), *New Techniques for the Automatic Registration of Microwave and Optical Remotely Sensed Images,* PhD, University College London.

Day, T. and Muller, J. (1989), "Digital Elevation Model Production by Stereo Matching Spot Image Pairs: a Comparison of Algorithms", *Image and Vision Computing*, vol. 7, no. 2, pp. 95-101.

Denos, M. (1991), "An Automatic Approach to Stereo Matching Seasat Imagery", *Proceedings of the British Machine Vision Conference, Glasgow, Scotland* pp. 335-338.

Denos, M. (1992), "A Pyramidal Scheme for Stereo Matching SIR-B Imagery", *International Journal of Remote Sensing*, vol. 13, no. 2, pp. 387-392.

Dowman, I. (1992), "The Geometry of SAR Images for Geocoding and Stereo Applications", *International Journal of Remote Sensing*, vol. 13, no. 9, pp. 1609-1617.

Dowman, I., Twu, Z.-G., & Chen, P. H. (1997), "DEM Generation from Stereoscopic SAR Data", *International Symposium: Geomatics in the ERA of RADARSAT (GER97)*, vol. CDROM.

Edwards, E. P. (2002), *Digital surface Modelling in Developing Countries Using Spaceborne SAR Techniques*, Internal PhD Report, University of Nottingham.

Edwards, E. P. (1994), *Land Surveying with Garmin GPS Receivers,* BSc Dissertation, University of the West Indies, Trinidad.

Edwards, E. P. (1998), *Orthorectification and Mosaicing of Digitized Aerial Photographs,* MPhil Thesis, University of Cambridge.

Edwards, E. P., Sowter, A., & Smith, M. J. (2004), "Evaluation of a Space Intersection Strategy for use with Stereoscopic SAR Imagery over Developing Countries", *Proceedings of the 2004 Envisat Symposium. Sept 6-10, Salzburg, Austria*.

Edwards, E. P., Sowter, A., & Smith, M. J. (2005), "Algorithm Development for the Automatic Extraction of Topographic Data from Stereoscopic ENVISAT Imagery over Caribbean Territories", *Proceedings of RSPSoc 2005 - Measuring, Mapping and Managing a Hazardous World. University of Portsmouth, September 6-9*.

Elachi, C. (1988), *Spaceborne Radar Remote Sensing: Applications and Techniques* IEEE Press, New York.

ESA (1998), *Envisat ASAR: Science and Applications. Report # SP-1225* European Space Agency Publishing Division, The Netherlands.

ESA (2002), *Envisat ASAR Product Handbook Issue 1.1* European Space Agency.

Fairfield, J. and Leymarie, P. (1991), "Drainage Networks from Grid Digital Elevation Models", *Water Resources Research*, vol. 30, no. 6, pp. 1681-1692.

Farr, T. G. and Kobrick, M. (2000), "The Shuttle Radar Topography Mission - A global DEM", *Proceedings of the 3rd European Conference on Synthetic Aperture Radar, Germany. May 23 - 25*.

Flood, M. (2001), "Laser Altimetry: From Science to Commercial Mapping", *Photogrammetric Engineering and Remote Sensing*, vol. 67, pp. 1209-1217.

Forstner, W. (1986), "A Feature Based Correspondence Algorithm for Image Matching", *International Archives of Photogrammetry and Remote Sensing*, vol. 26, no. 3, pp. 150-162.

Fowler, R. (2001), "Topographic LiDAR," in *Digital Elevation Model Technologies and Applications: The DEM Users Manual*, Maune D.F, ed., ASPRS, Maryland, pp. 207-236.

Fox, L. (1958), *Tables of Everett Interpolation Coefficients* HMSO, London.

Frankot, T. R. and Chellappa, R. (1990), "Estimation of Surface Topography from SAR Using Shape From Shading Techniques", *Artificial Intellegence*, vol. 43, no. 3, pp. 271-310.

Frost, V. S., Stiles, J. A., Shamugan, K. S., & Holtzman, J. C. (1982), "A model for Radar Images and its Application to Adaptive Digital Filtering of Multiplicative Noise", *IEEE Transaction on Pattern Analysis and Machine Intelligence*, vol. 4, pp. 157-166.

Fullerton, J. K., Leberl, F. W., & Marque, R. E. (1986), "Opposite-Side SAR Image Processing for Stereo Viewing", *Photogrammetric Engineering and Remote Sensing*, vol. 52, no. 9, pp. 1487-1498.

Gabriel, A. K. and Goldstein, R. M. (1998), "Cross Orbit Interferometry: Theory and Experimental Results from SIR-B", *International Journal of Remote Sensing*, vol. 9, no. 5, pp. 857-872.

Gelautz, M., Paillou, P., Chen, C. W., & Zebker, H. A. (2003), "Radar Stereo- and Interferometry-derived Digital Elevation Models: Comparison and Combination Using Radarsat and ERS-2 Imagery", *International Journal of Remote Sensing*, vol. 24, no. 24, pp. 5243-5264.

Girvan, R. A. (1984), *Jamaica Horizontal Adjustment (JAD69)*, Jamaica Survey Department, Kingston.

Goldstein, R. M., Zebker H.A, & Werner, C. (1988), "Sattelite Radar Interferometry: Two Dimensional Phase Unwrapping", *Radio Science*, vol. 23, no. 4, pp. 713-720.

Goncalves, J. and Dowman, I. (1998), "Precise Geocoding and Orbit Improvement of RADARSAT SAR Images", *Proceedings of Radarsat ADRO Symposium.Montreal Canada*.

Gooch, M. and Chandler, J. (1998), "Optimization of Strategy Parameters used in Automated Digital Elevation Model Generation", *International Archives of Photogrammetry and Remote Sensing*, vol. 32, no. 2, pp. 88-94.

Goodman, J. W. (1976), "Some Fundamental Properties of Speckle", *Journal of the Optical Society of America*, vol. 66, pp. 1145-1150.

Graham, L. C. (1974), "Synthetic Interferometer Radar for Topographic Mapping", *Proceedings of the IEEE*, vol. 62, no. 6, pp. 763-768.

Gruen, A. W. (1985), "Adaptive Least Squares Correlation: A Powerful Image Matching Technique", *South African Journal of Photogrammetry and Cartography*, vol. 14, no. 3, pp. 175-187.

Guindon, B. (1990), "Development of a Shape From Shading Technique for the Extraction of Topographic Models from Individual Spaceborne Images", *IEEE Transactions on Geoscience and Remote Sensing*, vol. 28, no. 4, pp. 654-661.

Hannah, M. J. (1989), "A system for Digital Stereo Image Matching", *Photogrammetric Engineering and Remote Sensing*, vol. 55, no. 12, pp. 1765-1770.

Haralick, R. M., Shanmugan, K., & Dinstein, I. (1973), "Textural Features for Image Classification", *IEEE Transaction on Systems, Man and Cybernetics*, vol. 6, pp. 610-621.

Heipke, C. (1996), "Overview of Image Matching Techniques", *Proceedings of OEEPE Workshop on Applications of Digital photogrammetric Workstations*, vol. 33, pp. 173-189.

Hensley, S., Goldstein, R. M., & Rosen, P. (1993), "Techniques and applications of SAR interferometry for ERS-1: Topographic mapping, change detection, and slope measurement", *Proceedings of First ERS-1 Symposium on Space at the Service of Our Environment*, vol. 1, pp. 205-210.

HMSO (1956), *Interpolation & Allied Tables* HMSO, London.

Hoffman-Wellenhof, Lichtenegger, B. H., & Collins, J. (1994), *GPS: Theory and Practice*, 3rd edn, Springer-Verlag, New York.

Jon, U. (1991), *An Orbit Propagator which Models Drag, J2 and Lunar Pertubations,* BSc Dissertation, University of Washington.

Ka, M.-H. and Kim, M.-J. (2001), "Digital Elevation Map Generation Using SAR Stereo Technique with Radarsat Images over Seoul Area", *Korean Journal of Remote Sensing*, vol. 17, no. 2, pp. 155-164.

Kanade, T. and Okutomi, M. (1994), "A Stereo Matching Algorithm with Adaptive Window: Theory & Experiment", *IEEE Transaction on Pattern Analysis and Machine Intelligence*, vol. 16, no. 9.

Kaplan, E. D. (1996), *Understanding GPS: Principles and Applications* Artech House, Boston.

Kavanagh, B. F. (2003), *Surveying: Principles and Applications* Prentice Hall, New Jersey.

Kennie, T. J. M. and Petrie, G. (1990), *Engineering Surveying Technology* Blackie, Glasgow.

Kim, M. (2003), "An Efficient Rectification Algorithm for Spaceborne SAR Imagery Using Polynomial Model", *Korean Journal of Remote Sensing*, vol. 19, no. 5, pp. 363-370.

Kingsley, S. and Quegan, S. (1992), *Understanding Radar Systems* McGraw-Hill, Berkshire, England.

Kost, W. (2002), "Imaging Latin America and the Caribbean: A View from the Company GeoAir", *GIM International* no. July.

Kuan, D. T., Sawchuk, A. A., Strand, T. C., & Chavel, P. (1985), "Adaptive Noise Smoothing filter for Images with Signal-Dependent Noise", *IEEE Transaction on Pattern Analysis and Machine Intelligence*, vol. 7, no. 2, pp. 165-177.

Kuan, D. T., Sawchuk, A. A., Strand, T. C., & Chavel, P. (1987), "Adaptive Restoration of Images with Speckle", *IEEE Transaction on Acoustic Speech and Signal Processing*, vol. 35, no. 3, pp. 373-383.

Kwok, R., Curlander, J. C., & Pang, S. S. (1990), "An Automated System for Mosaicking Spaceborne SAR Imagery", *International Journal of Remote Sensing*, vol. 11, no. 2, pp. 209-223.

La Prade, G. L. (1963), "An Analytical and Experimental Study of Stereo for Radar", *Photogrammetric Engineering*, vol. 29, no. 2, pp. 294-300.

Lane, S. N., Reid, S. C., Westway, R. M., & Hicks, D. M. (2004), "Remotely sensed topographic data for river channel research: the identification, explanation and management of error," in *Spatial Modelling of the Terrestrial Environment*, Kelly R.E.J, Drake N.A, & Barr S.L, eds., John Wiley & Sons, Chichester.

Leberl, F. W. (1990), *Radagrammetric Image Processing* Artech House, Norwood, MA.

Leberl, F. W. (1998), "Radargrammetry," in *ASPRS Manual of Remote Sensing: Principles and Applications of Imaging Radar*, 3rd edn, F. M. Henderson & A. J. Lewis, eds., John Wiley & Sons, New York, pp. 183-269.

Leberl, F. W. (1979), "Accuracy Analysis of Stereo Side-Looking Radar", *Photogrammetric Engineering and Remote Sensing*, vol. 45, no. 8, pp. 1083-1096.

Leberl, F. W., Domik, G., Raggam, J., & Kobrick, M. (1986), "Radar Stereomapping Techniques and Applications to SIR-B Images of Mt. Shasta", *IEEE Transactions on Geoscience and Remote Sensing*, vol. 24, no. 4, pp. 473-481.

Leberl, F. W., Maurice, K., Thomas, J. K., & Millot, M. (1994), "Automated Radar Image Matching Experiments", *ISPRS Journal of Photogrammetry & Remote Sensing*, vol. 49, no. 3, pp. 19-33.

Lee, J. S. (1980), "Digital image Enhancement and Noise Filtering by use of Local Statistics", *IEEE Transaction on Pattern Analysis and Machine Intelligence*, vol. 2, pp. 165-168.

Lee, J. S. (1986), "Speckle Suppression and Analysis for Synthetic Aperture Radar", *Optical Engineering*, vol. 25, pp. 636-643.

Lee, J. S. (1981), "Speckle Suppression and Analysis for Synthetic Aperture Radar Images", *Optical Engineering*, vol. 15, pp. 380-389.

Leica (2003), *Leica Photogrammetric Suite User Guide - 1* Leica Geosystems, Atlanta, Georgia.

Leick, A. (1995), *GPS Satellite Surveying*, 2nd edn, John Wiley & Sons, New York.

Lemmens, M. J. (1988), "A survey of Image Matching Techniques", *International Archives of Photogrammetry and Remote Sensing*, vol. 27, no. B3, pp. 11-23.

Lewis, A. J. and Henderson, F. M. (1998), "Radar Fundamentals: The Geoscience Perspective," in *ASPRS Manual of Remote Sensing: Principles and Application of Imaging Radar*, 3rd edn, F. M. Henderson & A. J. Lewis, eds., John Wiley & Sons, New York, pp. 131-181.

Li, F. K. and Goldstein, R. M. (1990), "Studies of Multibaseline Spaceborne Interferometric Synthetic Aperture Radar", *IEEE Transactions on Geoscience and Remote Sensing*, vol. 28, no. 1, pp. 88-97.

Lillesand, T. M., Kiefer, R. W., & Chipman, J. W. (2004), *Remote Sensing and Image Interpretation*, 5th edn, John Wiley & Sons, New York, NY.

Lopes, A., Nezry, E., Touzi, R., & Laur, H. (1990a), "A Maximum A-Posteriori Filtering and First Order Texture Models in SAR Images", *IGARSS '90, Washington D.C* pp. 2409-2412.

Lopes, A., Nezry, E., Touzi, R., & Laur, H. (1993), "Structure Detection and Statistical Adaptive Speckle Filtering in SAR Images", *International Journal of Remote Sensing*, vol. 14, no. 9, pp. 1735-1758.

Lopes, A., Touzi, R., & Nezry, E. (1990b), "Adaptive Speckle Filters and Scene Heterogeneity", *IEEE Transactions on Geoscience and Remote Sensing*, vol. 28, no. 6, pp. 992-1000.

Maling, D. H. (1991), *Coordinate Systems and Map Projections*, 2nd edn, Pergamon, Oxford.

Marr, D. and Hildreth, E. (1980), "Theory of Edge Detection", *Proceedings of the Royal Society of London*, vol. B207, pp. 187-217.

Marr, D. and Poggio, T. (1979), "A computational Theory of Human Stereo Vision", *Proceedings of the Royal Society of London*, vol. B204, pp. 301-328.

Martz, L. W. and Garbrecht, J. (1992), "Numerical Definition of Drainage Network and Subcatch-ment Areas from Digital Elevation Models", *Computer and Geosciences*, vol. 18, no. 6, pp. 747-761.

Mather, P. M. (2001), *Computer Processing of Remotely-Sensed Images: An Introduction*, 2nd edn, John Wiley & Sons, Chichester.

Mikhail, E. M. (1976), *Observation and Least Squares* IEP, New York.

Mikhail, E. M., Bethel, J. S., & McGlone, J. C. (2001), *Introduction to Modern Photogrammetry* John Wiley & Sons, New York.

Moore, T. (1986), *Satellite Laser Ranging and the Determination of Earth Rotation Parameters,* PhD Thesis, University of Nottingham.

Moore, T. (2001), *Coordinate Systems and Map Projections Lecture Notes* Unpublished, University of Nottingham.

Newsome, G. G. (2000), *GPS Coordinates Transformation Parameters for Jamaica,* MSc Dissertation, University New South Wales.

Nezry, E., Lopes, A., & Touzi, R. (1991), "Detection of Structural and Textural Features for SAR Images Filtering", *Proceedings of the International Geoscience and Remote Sensing Symposium (IGARSS)*, vol. 4, pp. 2169-2172.

Ostrowski, J. A. and Cheng, P. (2000), "DEM Extraction from Stereo SAR Satellite Imagery", *Proceedings IEEE International Geoscience And Remote Sensing Symposium*, vol. 5, pp. 2176-2178.

Otten, M. and Dow, J. (2004), "Envisat Precise Orbit Determination", *Proceedings of the 2004 Envisat and ERS Symposium, Salzburg, Austria*, vol. ESA SP-572.

Otto, G. P. and Chau, K. W. (1989), "Region-Growing Algorithm for matching of Terrain Images", *Image and Vision Computing*, vol. 7, no. 2, pp. 83-94.

Paillou, P. and Gelautz, M. (1999), "Relief Reconstruction from SAR Stereo Pairs: The "Optimal Gradient" Matching Method", *IEEE Transactions on Geoscience and Remote Sensing*, vol. 37, no. 4, pp. 2099-2107.

Pitas, I. (2000), *Digital Image Processing: Algorithms and Applications* John Wiley & Sons, New York.

Premalatha, M. (2001), *Quality Assessment of Interferometrically Derived DEMs,* PhD Thesis, University of Nottingham.

Press, W. H., Teukolsky, S. A., Vetterling, W. T., & Flannery, B. P. (2002), *Numerical Recipes in C++*, 2 nd edn, Cambridge University Press, Cambridge, UK.

Raggam, H. and Gutjahr, K. (1998), "DEM Generation Using Radarsat Stereo Data", *Proceedings of the Radarsat ADRO Symposium.Montreal, Canada*.

Ramapriyan, H. K., Strong, J. P., Hung, Y., & Murray, C. W. (1986), "Automated Matching of Pairs of SIR-B Images for Elevation Mapping", *IEEE Transactions on Geoscience and Remote Sensing*, vol. 24, no. 4, pp. 462-472.

Rizos, C. (1997), *Principles and Practice of GPS* UNSW, Sydney.

Rosenfield, G. H. (1968), "Stereo Radar Technique", *Photogrammetric Engineering*, vol. 34, no. 6, pp. 586-594.

RSI (1997), *Radarsat CEOS Product Specification: RSI-GS-021* Radarsat International, Richmond, Canada.

RSI (1998), *RADARSAT Swath planner User Manual* RadarSat International, Richmond, British Columbia.

RSI (2000), *RADARSAT Data Products Specifications*, 3rd edn, RadarSat International, Richmond, British Columbia.

Rufino, G., Moccia, A., & Esposito, S. (1998), "DEM Generation by Means of ERS Tandem Data", *IEEE Transactions on Geoscience and Remote Sensing*, vol. 36, no. 6, pp. 1905-1912.

Sabins, F. F. (1997), *Remote Sensing: Principles and Interpretation*, 3 rd edn, W. H. Freeman & Company, New York, NY.

Schenk, A. F. (1996), "Automatic Generation of DEM's," in *Digital Photogrammetry: An Addendum to the Manual of Photogrammetry*, C. Greve, ed., ASPRS, Maryland, pp. 145-150.

Schenk, T. (1999), *Digital Photogrammetry* TerraScience, Laurelville, Ohio.

Schuler, D. L., Ainsworth, T. L., Lee, J. S., & De Grandi, D. (1998), "Topographic Mapping Using Polarimetric SAR Data", *International Journal of Remote Sensing*, vol. 19, no. 1, pp. 141-160.

Schuler, D. L., Lee, J. S., & De Grandi, D. (1996), "Measurement of Topography Using Polarimetric SAR Images", *IEEE Transactions on Geoscience and Remote Sensing*, vol. 34, no. 5, pp. 1266-1277.

Seeber, G. (2003), *Satellite Geodesy*, 2nd edn, Walter de Gruyter, Berlin.

Shearer, J. W. (1990), "The Accuracy of Digital Terrain Models," G. Petrie & T. J. M. Kennie, eds., Whittles Publishing, London, pp. 315-336.

Shi, Z. and Fung, K. O. (1994), "A Comparison of Digital Speckle Filters", *Proceedings of the International Geoscience and Remote Sensing Symposium (IGARSS 94)* pp. 2129-2133.

Shukla, R. K. (2001), *Geo-Referencing of Airborne Imagery Using Direct Measurement of Position and Attitude,* PhD Thesis, University of Nottingham.

Simard, R., Plourde, F., & Toutin, T. (1986), "Digital Elevation Modeling with Stereo SIR-B Data", *Proceedings of the 7th International Symposium on Remote Sensing for Resource Development and Environmental management, ISPRS Commission VII*, vol. 1, pp. 161-166.

Smith, M. J. (2005), *Photogrammetry Lecture Notes* IESSG, The University of Nottingham, Nottingham, UK (unpublished).

Smith, M. J., Edwards, E. P., Priestnall, G., & Bates, P. (2005), *Creation of Digital Elevation Models for Flood Inundation Modelling* Report Prepared for the UK Flood Risk Management Research Consortium, Nottingham, UK.

Smith, M. J., Priestnall, G., & Asal, F. (2000), "Combining Lidar & Photogrammetry for Urban and Rural Landscape Studies", *International Archives of Photogrammetry and Remote Sensing*, vol. 33, no. B3, pp. 44-50.

Sowter, A. (2005), *Introduction to SAR Lecture Notes* The University of Notingham, Unpublished.

Sowter, A. (1998), "The Automatic Extraction of DEM Data from Stereo Radasat Pairs over the Tropics", *International Archives of Photogrammetry and Remote Sensing*, vol. 32, no. 2, pp. 291-298.

Sun, C. (1998), *Multi-Resolution Rectangular Subregioning Stereo Matching Using Fast Correlation and Dynamic Programming Techniques* CSIRO, Macquarie University Campus, North Ryde, NSW.

Sylvander, S., Petitcolas, B., Cousson, D., & Souyris, J.-C. (1998), "Evaluation of the Potential of Radarsat Images for the Production of Digital Terrain Model by Radargrammetry", *Proceedings of the Radarsat ADRO Symposium.Montreal, Canada*.

Thomas, J. W., Kober, F., & Leberl, F. W. (1991), "Multiple Image SAR Shape From Shading", *Photogrammetric Engineering and Remote Sensing*, vol. 57, no. 1, pp. 51-59.

Toutin, T. (2001), "Elevation Modelling from Satellite Visible and Infrared (VIR) Data", *International Journal of Remote Sensing*, vol. 22, no. 6, pp. 1097-1125.

Toutin, T. (1996), "Opposite Side ERS-1 SAR Stereo Mapping over Rolling Topography", *IEEE Transactions on Geoscience and Remote Sensing*, vol. 34, no. 2, pp. 543-549.

Toutin, T. (1999), "Error Tracking of Radargrammetric DEM from RADARSAT Images", *IEEE Transactions on Geoscience and Remote Sensing*, vol. 37, no. 5, pp. 2227-2238.

Toutin, T. (2000), "Evaluation of Radargrammetric DEM from RADARSAT Images in High Relief Areas", *IEEE Transactions on Geoscience and Remote Sensing*, vol. 38, no. 2, pp. 782-789.

Toutin, T. (2002), "Impact of Terrain Slope and Aspect on the radargrammetric DEM Accuracy", *ISPRS Journal of Photogrammetry & Remote Sensing*, vol. 57, pp. 228-240.

Toutin, T. and Gray, L. (2000), "State-of-the-Art of Elevation from Satellite SAR Data", *ISPRS Journal of Photogrammetry & Remote Sensing*, vol. 55, pp. 13-33.

Toutin, T. (1995), "Generating DEM from Stereo Images with a Photogrammetric Approach: Examples with VIR and SAR Data", *EARSeL Advances in Remote Sensing*, vol. 4, no. 2, pp. 110-117.

Trimble (2001), *GeoExplorer 3: Operation Guide* Trimble Navigation Limited, Sunnyvale, CA.

Tso, B. and Mather, P. M. (2001), *Classification Methods for Remotely Sensed Data* Taylor & Francis, London.

Twu, Z.-G. (1996), *Automatic Height Extraction from Stereoscopic SAR Imagery,* PhD, University College London.

Twu, Z.-G. and Dowman, I. (1996), "Automatic Height Extraction from ERS-1 SAR Imagery", *International Archives of Photogrammetry and Remote Sensing*, vol. 31, no. B2, pp. 380-383.

Ulaby, F. T., Kouyate, F., Brisco, B., & Williams T.H.L (1986a), "Textural Information in SAR Images", *IEEE Transactions on Geoscience and Remote Sensing*, vol. 24, no. 2, pp. 235-245.

Ulaby, F. T., Moore, R. K., & Fung, A. K. (1981), *Microwave Remote Sensing: Active and Passive, Volume 1* Addison-Wesley, Reading, Massachusetts.

Ulaby, F. T., Moore, R. K., & Fung, A. K. (1986b), *Microwave Remote Sensing: Active and Passive, From Theory to Application* Artech House, Dedham, MA.

Vachon, P. W., Geudtner, D., Gray, A. L., & Touzi, R. (1995), "ERS-1 synthetic aperture radar repeat-pass interferometry studies: implications for RADARSAT", *Canadian Journal of Remote Sensing*, vol. 21, no. 4, pp. 441-454.

Veregin, H. (1999), "Data quality parameters," in *Geographical Information Systems: Principles and Technical Issues*, vol. one Longley P.A et al., eds., John Wiley & Sons, Chichester, pp. 175-189.

Watson, D. F. (1994), *Contouring: A Guide to the Analysis and Display of Spatial Data* Pergamon Press, Oxford.

Wehr, A. and Lohr, U. (1999), "Airborne Laser Scaanning: An Introduction and Overview", *ISPRS Journal of Photogrammetry & Remote Sensing*, vol. 54, pp. 68-82.

Wells, D. (1989), *Guide to GPS Positioning* Canadian GPS Associates, Fredericton.

Wimmer, C., Siegmund, R., & Moreira, J. (1999), "Derivation and Validation of High Precision Topography Models in the Waddensea with Airborne SAR-Interferometry", *Proceedings of IGARS99, 28 June - 2 July 1999, Hamburg, Germany*.

Wise, S. (1998), "The effect of GIS interpolation errors on the use of DEMs in geomorphology," in *Landform Monitoring, Modelling and Analysis*, Lane S.N, Richards K.S, & Chandler J.H, eds., John Wiley & Sons, Chichester, pp. 139-164.

Wolf, P. R. and Dewitt, B. A. (2000), *Elements of Photogrammetry: With Applications in GIS*, 3 rd edn, McGraw-Hill, Boston.

Zebker, H. A. and Goldstein, R. M. (1986), "Topographic Mapping from Interferometric Synthetic Aperture Radar Observations", *Journal of Geophysical Research*, vol. 91, no. B5, pp. 4993-4999.

Zebker, H. A., Werner, C., Rosen, P., & Hensley, S. (1994), "Accuracy of Topographic Maps Derived from ERS-1 interferometric Radar", *IEEE Transactions on Geoscience and Remote Sensing*, vol. 32, pp. 823-836.

Zhen, X. (2001), "Extracting DEM from SPOT Images", *Proceeding of the 22nd Asian Conference on Remote Sensing*.